Aston University

If you have discovered material in AURA which is unlawful e.g. breaches copyright, (either yours or that of a third party) or any other law, including but not limited to those relating to patent, trademark, confidentiality, data protection, obscenity, defamation, libel, then please read our Takedown Policy and contact the service immediately

Analysis and optimisation of the performance of nonlinear optical communication systems

IRINA OLEGOVNA NASIEVA

Doctor of Philosophy

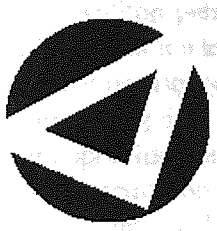

ASTON UNIVERSITY

October 2006

This copy of the thesis has been supplied on condition that anyone who consults it is understood to recognise that its copyright rests with its author and that no quotation from the thesis and no information derived from it may be published without proper acknowledgement.

ASTON UNIVERSITY

Analysis and optimisation of the performance of nonlinear optical communication systems

IRINA OLEGOVNA NASIEVA

Doctor of Philosophy, 2006

Thesis Summary

This thesis presents a general analysis and optimisation of the performance of nonlinear optical transmission systems.

We investigate the feasibility of simultaneous suppressing of the amplification noise and nonlinearity, representing the most fundamental limiting factors in modern optical communication. To accomplish this task we developed a general design optimisation technique, based on concepts of noise and nonlinearity management. We demonstrate the immense efficiency of the novel approach by applying it to a design optimisation of transmission lines with periodic dispersion compensation using Raman and hybrid Raman-EDFA amplification. Moreover, we showed, using nonlinearity management considerations, that the optimal performance in high bit-rate dispersion managed fibre systems with hybrid amplification is achieved for a certain amplifier spacing— which is different from commonly known optimal noise performance corresponding to fully distributed amplification.

Required for an accurate estimation of the bit error rate, the complete knowledge of signal statistics is crucial for modern transmission links with strong inherent nonlinearity. Therefore, we implemented the advanced multicanonical Monte Carlo (MMC) method, acknowledged for its efficiency in estimating distribution tails. We have accurately computed marginal probability density functions for soliton parameters, by numerical modelling of Fokker-Plank equation applying the MMC simulation technique. Moreover, applying a powerful MMC method we have studied the BER penalty caused by deviations from the optimal decision level in systems employing in-line 2R optical regeneration. We have demonstrated that in such systems the analytical linear approximation that makes a better fit in the central part of the regenerator nonlinear transfer function produces more accurate approximation of the BER and BER penalty. We present a statistical analysis of RZ-DPSK optical signal at direct detection receiver with Mach-Zehnder interferometer demodulation. A close-form analytical expression for the BER is derived in the limit of narrow pulses. This theoretical result is supported by numerical MMC simulations. Furthermore, we apply the MMC method to evaluate the performance of an RZ optical receiver enhanced by a nonlinear all-optical decision element. We demonstrate more than one order improvement in the BER over the conventional receiver for operation at 40 Gb/s.

Keywords: nonlinearity management, Monte Carlo methods, soliton statistics, 2R optical regeneration, RZ-DPSK modulation format, all-optical decision element

To my husband Diar

Acknowledgements

First and foremost I am grateful to my supervisor Prof. Sergei K. Turitsyn for the support, encouragement and much needed guidance offered to me during my studies at Aston. As a remarkable scientist and a wonderful person, he deserved my deepest respect.

I wish to thank Dr. Juan Diego Ania-Castañón who enormously helped me through the first year of my PhD. I deeply appreciate his kind character and willingness to help.

My special thanks go to Dr. Sonia Boscolo who helped me many times and whose support has always been invaluable to me. I wish to thank Dr. Stanislav A. Derevyanko for teaching me the characteristics method and Dr. Vladimir Mezentzev for giving me valuable lessons in a good style object-oriented programming.

Mr. Andrey Kaliazin deserved special thanks for his much appreciated support and advice on usage of Cray and Condor at Aston University. It was a pleasure to work with him.

My special acknowledgements also go to my fellow colleagues Jovana Petrović, Zahariah Zakaria, Supun Authukorale, Ranjeet Bhambers and Christos Braimiotis. I would also like to thank Terence Broderick and Christopher French, with whom I closely collaborated in my final year. These people made my life in Birmingham enjoyable.

During my years at Aston I have always been receiving the strongest emotional support from my family and friends in Russia. I feel so much grateful to my mother and sister who did everything to help me to follow through tough periods of my study. Special thanks go to my friends in Russia for the wonderful time that we spend together.

Last but not least, I thank my husband Diar and our daughter Dina for their love and understanding.

Contents

List of Tables

List of Figures

Chapter 1

Introduction

1.1 Historical overview

The rapid development of the field of optical fibre communication started in the 1960s and has continued over the last four decades, following the growth in demand for telecommunication applications. The vast rate of improvement in optical transmission systems performance can be seen, for example, from a doubling of the product of information capacity and maximum transmission distance every year during this period [1].

The invention of the laser in 1960 [2] and the idea of using glass materials as a light guiding media suggested in 1966 [3, 4] encouraged extensive worldwide research in the field of optical communications. At this early stage, the performance of transmission systems was limited considerably by extremely high losses (up to 1000 dB/km) originating from the extrinsic material absorption due to the presence of impurities in the glass fibre. However, in 1970 fibre with losses as low as 20 dB/km [5] in the wavelength region near 1 μm was already possible to fabricate. In 1980 the transmission systems operating near 0.8 μm at a bit rate of 45 Mb/s became available commercially [6].

Although the transmission systems performance became considerably improved via using advanced fabrication techniques, still the digital transmission rate could not pass beyond the limit of 100 Mb/s imposed by the effect of intermodal dispersion. The intermodal or modal dispersion occurs in optical fibres supporting

several propagation modes and is related to different group velocities associated with different modes and a consequent broadening and distortion of transmitted pulses. This principal limitation was overcome with the advent of single mode fibres (SMF) first demonstrated in a laboratory experiment [7] in 1981. By designing a fibre with a sufficiently small core diameter and/or fractional refractive index change at the core-cladding interface one can suppress all but the lowest order fundamental propagation mode, thereby removing the intermodal dispersion from signal transmission. With the development of SMF, the bit rate of commercially available optical communication systems rose up to 1.7 Gb/s in 1987.

Along with the intermodal dispersion, other dispersion mechanisms present in fibre waveguides impose restrictions on optical signal transmission. So does the phenomenon of group velocity dispersion (GVD) or intramodal dispersion, which is originated in a frequency dependence of the group velocity. Since the light emitted from an optical source inevitably occupies a band of frequencies the dispersion causes temporal broadening, overlapping and the following distortion of transmitted pulses in a manner similar to intermodal dispersion. Among other dispersion phenomena critical for signal transmission is polarisation mode dispersion (PMD) which comes from the discrepancy between group velocities associated with two orthogonal polarisation states supported by the fundamental mode. PMD grows in importance when the channel bit rate exceeds 10 Gb/s and strongly affects modern optical transmission systems.

Until then the optical communication systems had been operating at a wavelength of 1.3 μm where the chromatic dispersion is comparatively small. The periodical signal regeneration required by long-haul transmission systems was accomplished through using electronic repeaters periodically inserted in the line at a distance limited by losses to approximately 50 km. Essentially the electronic repeaters proceed as a receiver - transmitter pair, where the optical signal is converted into an electrical current and subsequently re - launched into the next section of the optical fibre. Aided to reduce system and maintenance costs, the development of dispersion shifted fibres in the 1980s allowed to move the region of minimal dispersion towards a wavelength of 1.55 μm, where losses were known to have their minimum. As a

result, in 1985, a system capable of operating at 4 Gb/s over distances in excess of 100 km [8] was experimentally demonstrated.

A tremendous breakthrough in the field of optical communication occurred with advancement of optical amplification and the availability of erbium-doped fibre amplifiers (EDFAs) in 1989. EDFAs similar to other optical amplifiers employ the mechanism of stimulated scattering to produce gain in received signals. The insertion of erbium dopants in the amplifier transfers the wavelength region where the signals become amplified to near 1.55 μm, where the fibre losses attain their minimum. In addition, the wide amplification bandwidth provided by EDFAs made their deployment particularly attractive in combination with the wavelength - division multiplexing (WDM) technique. While the use of EDFAs permitted for much larger electronic regenerator spacing, utilisation of multiple transmission channels considerably increased the operational bit rates. Through a combination of these techniques a global submarine transmission network was created in the last decade of the 20th century , which operated with as many as 64 channels giving an overall capacity of up to 2.56 Tb/s in some connections [9].

Further improvement in the transmission capacity can be attained by increasing the number of deployed channels through the WDM technique. However, the fact that EDFAs can amplify signals only within a limited range of wavelengths implies strict limitations on the total bandwidth occupied by signals. These restrictions can be relaxed to some extent by implementing alternative amplification schemes able to provide a broader amplification bandwidth. For example, Raman amplification, in particular the development of a multiple pumping scheme attracted a considerable attention as a promising candidate for the future ultra high bit rate WDM optical fibre communication systems. Another advent further contributed to extending the existing operating bandwidth was the subsequent development of a dry fibre in 2000, acknowledged for its property to maintain low losses in the broad wavelength region between 1.3 and 1.65 μm [10].

Along with extending the operating bandwidth by increasing the number of deployed channels, tremendous efforts are being focused at improving the overall transmission capacity by increasing the bit rate in separate channels. Nowadays

transmission rates as high as 40Gb/s are achievable through careful system design by taking advantage of techniques specially developed to suppress, minimise or effectively counterbalance major performance limiting factors. In particular, such factors affecting the ultra long high bit rate transmission links enhanced by optical amplification are described below, preceding the discussion of the most popular designing techniques.

Fibre losses represent one of the factors degrading the performance of the lightwave communication systems. Mainly this effect is originated from (i) the material absorption; (ii) Rayleigh scattering due to random density fluctuations in the fused silica, resulting in random fluctuations in the refractive index of the transmission medium; (iii) waveguide imperfections, such as random core-radius variations and micro-bending losses; and (iv) losses caused by using in-line splices and connectors in the link. Generally the fibre losses cause an exponential decay in power of propagating signals, the negative effect which is typically overcome with the aid of existing optical amplification techniques.

However, the benefits of optical amplification were realised at the expense of inducing the amplifier spontaneous emission (ASE) noise in the transmission channel, an effect not present in communication systems with electronic regeneration. In signal transmission over large distances the ASE noise may essentially degrade the system performance, as it accumulates when signals propagate through a chain of cascaded optical amplifiers. Indeed, such a build up of noise in the transmission link is accompanied by a degradation in the signal to noise ratio (SNR), a characteristic restricted to exceed some value dependent on receiver sensitivity. Moreover, the accumulation of amplifier noise contributes to degradation of the SNR indirectly: at some level it starts to saturate the subsequent optical amplifiers, thereby gradually reducing the amplifier gain accessible to signals. To enable the propagating signal to be distinguishable from the amplifier noise, operating powers must be kept suitably large. As a consequence, with increasing the signal power, nonlinear effects become more exposed in signal transmission and in general further contribute to the degradation of the system performance.

The nonlinearity, like the ASE noise, accumulates over the propagation distance

and may lead to a signal distortion mostly through the phenomena of self-phase modulation (SPM), cross phase modulation (XPM) and four-wave mixing (FWM). Originating from the intensity dependence of the refractive index, the SPM and XPM manifest themselves through the phase shift acquired by propagating signals. Since the time varying phase causes variations in the instantaneous frequency, the phenomena of SPM and XPM can alter and broaden the spectrum of carrier pulses. In combination with GVD these nonlinear effects can also result in a temporary pulse broadening. Moreover, pulse amplitude variations and ghost-pulse generation caused by FWM in general may futher degrade the performance of modern optical transmission links. In more detail nonlinear impairments that are critical for optical signal transmission are introduced in Table 1.1. Although some control over the nonlinearity is possible by enlarging the fibre effective area, their effects generally can become critical for the transmission performance.

Another important phenomenon severely restricting the maximum operating distances in long-haul transmission lines with periodical optical amplification is the ASE-induced timing jitter. This effect, named after Gordon and Haus who first studied it in 1986 [11] in the context of soliton systems, initiates random deviations in temporary pulse positions and may occasionally result in pulses abandoning their time slots and subsequent erroneous bit detection at the receiver. The timing jitter, arising from the mutual interplay between the dispersion and ASE, originates from time-dependent random fluctuations of the signal phase introduced by amplification noise. The phase fluctuations impose slight modifications on the carrier frequency of propagating pulses, which by the action of the GVD become random shifts in pulse position in the time domain. The fact that timing jitter variance grows proportionally to the cube of the transmission distance [12] justifies the effect as one of the most crucial for long distance optical communication, especially at bit rates exceeding 10 Gb/s. The control over the timing jitter to a great extent can be established by applying existing dispersion management techniques to a system design in order to maintain the total dispersion accumulated in the link close to zero. Otherwise, the amount of timing jitter acquired by signals can be reduced by inserting optical filters after the amplifiers. This method however, suffers from the disad-

nonlinear factor	physical origin	description	negative effect	possible application
self-phase modulation	intensity dependence of the refractive index	self-induced intensity dependent phase shift in propagating signals	variations in spectral pulse width; temporal pulse broadening due to GVD	formation of optical solitons in anomalous-dispersion fibres
interchannel cross-phase modulation (XPM)		phase modulation induced by optical signals propagating at different frequencies	assymetric spectral broadening of co-propagating optical pulses; interaction between channels in WDM optical signal transmission	pulse compression and optical switching
intrachannel cross-phase modulation (IXPM)		phase modulation acquired due to a nonlinear interaction between overlapping neighbouring pulses propagating in the same communication channel	frequency chirp and subsequent timing jitter; the effect is particularly strong at bit rates ≥ 40 Gb/s	
interchannel four-wave mixing (FWM)	third order nonlinear susceptibility	generation of an optical field at a wavelength $w = w_1 \pm w_2 \pm w_3$, when optical signals copropogating at wavelengths w_1,w_2 and w_3 satisfy the phase-matching requirement	although can affect the performance of WDM systems, in general can be avoided by keeping the local GVD high all along the fibre	time-division demultiplexing and wavelength conversion
intrachannel four-wave mixing (IFWM)		transferring the energy from overlapping pulses in the bit slot positions t_1, t_2 and t_3 to a pulse in the position $t = t_1 + t_2 - t_3$	amplitude variations in "ones" and ghost-pulse generation in "zeros"; particularly important at high bit rates (≥ 40 Gb/s)	

Table 1.1: Nonlinear effects in fibre optics communications.

vantage of introducing additional losses in the system and, hence requires careful optimisation.

To summarise the above, the most fundamental limitations in modern long distance high bit rate optical transmission systems are caused by chromatic dispersion, through the pulse temporary broadening and shifting, nonlinearities, contributing to the temporary pulse broadening and amplitude fluctuations, ASE noise responsible for the SNR degradation and at higher bit rates, PMD which introduces further temporary broadening to pulses. Dictated by the necessity to include in analysis all the performance-limiting factors, a search for the optimal system design becomes a challenging task. In this respect, a number of effective designing techniques have been suggested, with the most constructive reviewed below.

Dispersion compensation (DC) represents probably the most popular approach in modern optical communication for establishing control over the chromatic dispersion. The underlying idea of this technique is to assign the average dispersion of the transmission line to zero, with the implication that signals, despite undergoing a considerable pulse broadening during propagation, arrive at the receiver with their original pulse widths. In practice, DC is typically accomplished through the deployment of dispersion-compensating fibres (DCF), first suggested in 1980 [13], with alternatives in the form of optical filters [14, 15] and fibre Brag gratings [16, 17]. By keeping local values of GVD high and at the same time the dispersion of the entire link close to zero, DC enables one to suppress dispersion induced pulse broadening and timing jitter. Moreover, DC restrains FWM, a nonlinear factor severely degrading multichannel transmission, by reducing the efficiency of the phase matching condition. From an economical point of view, such DC schemes offer an advantage of rather upgrading the existing SMF based networks than building new ones.

Signal degradation due to nonlinearity can be substantially suppressed through a widely acknowledged technique of dispersion management (DM). The DM approach, resting on the power dependency of nonlinearity, suggests that signals should be exposed to maximum nonlinear effects when they have the smallest energy during propagation. In this respect, it has become common practice to implement periodic dispersion maps, i.e. separately compensate for accumulated GVD within

each amplification period in a periodic fashion. Moreover, by a slight alteration of the link average dispersion, usually implemented through a carefully optimised dispersion post- and pre-compensation, DM permits to suppress pulse width variations induced by moderate nonlinear effects. By a suitable design of dispersion maps even substantial nonlinearity can be reduced to an acceptable level and therefore be compensated. The only restriction arising in DM transmission systems is that launched signals are limited to having sufficiently low powers, as such systems are aimed to operate in a quasi-linear regime. This condition in principle may conflict with the requirements imposed on SNR. The high potential of periodic dispersion compensation can be seen, for example, from the 2001 experiment [18] demonstrating 1Tb/s data transmission over 9000 km using 101 channels operating at a rate of 10 Gb/s.

An alternative approach to treat the nonlinearity is to turn it to ones' advantage, as in soliton transmission systems. The fundamental solitons' ability to preserve their shape in a lossless anomalous dispersion optical fibre, based on a balance between the dispersion and nonlinearity, attracted considerable attention to the idea of soliton-based communication. The existence of solitons in optical fibres was first predicted in a theoretical study [19] in 1973 and in 1980 it was observed experimentally [20]. In particular, it was demonstrated that secant hyperbolic pulses with the pulse width and peak power satisfying a certain relationship dependent on fibre parameters, can fully compensate for the dispersion pulse broadening by nonlinear phase shift acquired through SPM, thus effectively counterbalancing otherwise detrimental effects. In real transmission systems, where propagating signals undergo losses and subsequent amplification, solitons exist in an "average" sense; they maintain their profile similar to ideal solitons however, their peak power undergoes periodic fluctuations. Although in soliton-based communication limitations related to nonlinearity and dispersion are relaxed, new problems unique to solitons come forward. Among issues specific to soliton-based transmission the most essential are the requirements of sufficient soliton separation and shorter amplifier spacing. As a solitons' width can not be set arbitrary small without causing a considerable decline in the peak power unacceptable due to requirements on SNR, the dense pulse pack-

ing would lead to unwanted soliton interactions and possibly soliton collisions. As for the amplifier spacing, strong signal power variations occurring in transmission systems with large amplification period may lead to under-compensation of the dispersion by power dependent nonlinearity. In this respect, more uniform gain provided by Raman optical amplifiers compared to EDFA makes them more attractive for soliton-based transmission. As an example of essential performance improvement suggested by soliton-based communication, WDM transmission over 9000 km using eight 10Gb/s channels with the total capacity of 80 Gb/s was reported in [21].

A remarkable breakthrough in the field of soliton communication occurred with the development of DM solitons [22,23]. Interestingly, the DM technique, originally designed for operating in a low-power linear regime, became a considerable benefit for soliton transmission, strongly relying on nonlinearity. The distinctive feature of DM solitons is the strong variations in solitons shape occurring during one dispersion period, a "braising" effect, accompanied however by a complete restoration of the initial pulse at the end of each period. The shape of DM solitons is rather Gaussian and their power is enlarged compared to the conventional solitons in the fibre with the same average GVD. The latter property results in generally a better performance in terms SNR degradation demonstrated by DM solitons. Furthermore, unlike conventional solitons, DM solitons acquire a chirp during propagation through the optical fibre, which introduces a phase shift between successive pulses and subsequently gives an additional benefit of reduced soliton interaction. Another attractive quality inherent to DM solitons is their ability to propagate in lines with zero and even normal average GVD: operating at zero average dispersion offers an additional advantage of suppressing FWM and timing jitter. Evidently, such a valuable combination makes DM solitons extremely attractive information carrier for long-haul high capacity optical communication. As a demonstrative example, three channel transmission with the total capacity of 60Gb/s (20 Gb/s per channel) over 10000 km was observed experimentally [24]. Moreover, deployment of synchronous in-line modulation together with highly nonlinear fibres permitted to increase the single channel capacity up to 40Gb/s in 20000 km experiment [25].

Further enhancement in transmission bit rates of such DM soliton based commu-

nication is possible by either implementing increasingly dense dispersion maps, the approach referred to as short-period dispersion management, or, in single channel transmission systems, by operating at low local GVD. Both techniques are intended to limit the pulse width oscillations due to variations of GVD and thereby to reduce the pulse-to-pulse interaction. Furthermore, sliding-frequency filters provide an alternative tool to suppress timing jitter [26] in both classic soliton and DM soliton based transmission.

Another factor critical for optical communications is PMD, which has been addressed by developing a number of specific PMD compensation techniques. In one such technique, an optical PMD compensator uses a polarisation controller followed by a polarisation beam splitter to separate PMD distorted signals into two components along the principal polarisation states. After a delay introduced to one of the components, they are combined together. The magnitude of the delay is adjusted accordingly to an error signal obtained using a feed-back loop. Among other PMD compensation approaches are those based on electrical PMD equaliser, twisted polarisation-maintaining fibre and optical all-pass filters. Nonetheless, analysis of the PMD effect is beyond the scope of the thesis and hence we evade this issue in what follows.

With commercial availability of long-haul transmission systems operating at channel rates of 10 Gb/s and numerous experimental demonstrations of 40 Gb/s transmission over transoceanic distances, recent research efforts are being focused on increasing the transmission rates to 40 Gb/s and higher.

At such large data rates the physical principles governing signal propagation may essentially differ from those at 10 Gb/s. As an example consider the nonlinear effects. Though crucial at 10 Gb/s, the SPM and multichannel XPM and FWM at 40 Gb/s become dominated by single-channel nonlinear effects. An increased PMD sensitivity observed at 40 Gb/s provides another example of an aspect specific to ultra-high speed transmission. In this respect, it seems of importance to review the most constructive designing techniques in application to modern high speed optical communications.

The problems affecting high speed signal transmission and their practical solu-

Impairments	Combat techniques
fibre losses	optical amplification
dispersion	dispersion compensation techniques
nonlinearity	dispersion management, soliton-based transmission

Table 1.2: Major performance limiting factors and related combat techniques in modern optical communication.

tions are addressed in Table 1.2. As shown, the dispersive effects can be effectively managed through the technique of DC. Optical amplification represents the most practical way to deal with fibre losses, yet at a price of introducing ASE noise to the system. As for the nonlinearity, two distinct approaches were developed to address this problem. In the linear approach, often employed in combination with DM, an attempt is made to make the nonlinear impairments negligible small by operating at low signal intensity levels; while the other nonlinear or soliton approach which is generally applied to signals of larger intensity, is based on a balance between the GVD and nonlinearity. However, each approach suffers from specific serious limitations and the nonlinear effects remain one of the most fundamental issues in modern optical communications. In fact, the nonlinearity and ASE noise represent the most crucial factors restricting the performance of long-haul optical transmission operating at bit rates of 40 Gb/s and higher. Although in general acting independently, these dominant impairments can be interrelated through a schematic illustrated on Figure 1.1. The Figure illustrates how systems operating at excessively high and excessively low intensities equally undertake a performance decline. Indeed, insufficiently strong signals become rapidly buried by ASE noise accumulated during propagation, an effect even more pronounced for smaller signal powers. Moreover, signals with intensity in excess of some value are inevitably subjected to a large distortion due to the nonlinear effects. In practice, modern transmission systems aim to operate in the vicinity of the optimal power in the region where neither detrimental effect prevails. Several comparatively recent approaches suggest a possibility to relax the limitations imposed by the ASE noise and nonlinearity. Specifically, the deployment of in-line optical regenerators (ORs) permits the effective elimination

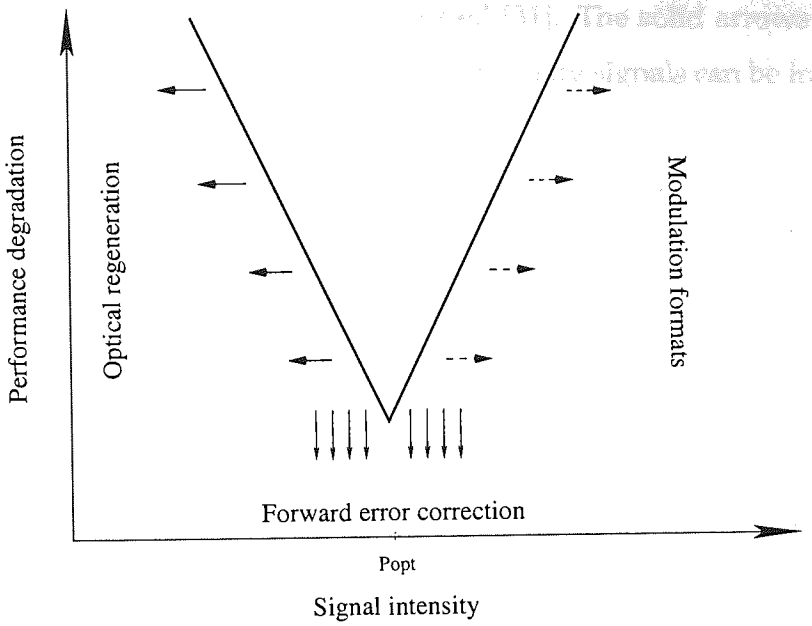

Figure 1.1: System performance degradation with respect to intensity of launched signals.

of amplification noise from a transmission system. Moreover, with development of advanced modulation formats it became possible to reduce the system sensitivity to nonlinear impairments. Finally, recently acknowledged forward error correction (FEC) ensures the overall improvement of a transmission system performance. Figure 1.1 shows an expansion to the existing operating intensity region, which is attainable via deployment of these techniques.

Optical regeneration suggests a promising technique to reduce the build up of ASE noise, a factor which seriously affects transmission performance. As an example, we consider 2R ORs periodically inserted in the link to reamplify and reshape propagating signals. Based on optical devices with strong nonlinear response, such regenerators impose a "threshold" action on the received signals and by suppressing the signals of low intensity and acting as amplifiers to stronger signals, they considerably reduce the effect of noise accumulation. In practice, 2R ORs can be constructed based on a semiconductor optical amplifier [27], nonlinear optical loop mirror [28] or a saturable absorber [29]. In a 10 Gb/s transmission example optical regeneration based on electroabsorbtion modulators allowed the increase of the error-free transmission distance from 24000 km to 30000 km [30]. In another experimental work, 40 Gb/s transmission over 1 000 000 km using fibre-based 2R ORs and

in-line synchronous modulators was reported [31]. The solid arrows in Figure 1.1 indicate that using optical regeneration, low intensity signals can be included in the operational range.

System performance degradation due to nonlinearity can be essentially reduced using advanced modulation formats. As we discuss bit rates of 40 Gb/s and higher, nonlinearity penalties in signal transmission are primarily associated with the effects of IFWM and IXPM [32–34]. In fact, IFWM induced amplitude variations and timing jitter due to IXPM acquired by pulses in bits corresponding to elementary "ones" substantially distort signal propagation. However, the most serious performance degradation in ultra-high speed transmission is caused by the generation of ghost pulses in "zero" bit slots [33–35] initiated by IFWM. Advanced modulation formats typically reduce the detrimental effect of the nonlinearity by imposing phase alternation on transmitted bits. For example, duobinary, modified duobinary and alternate-mark inversion modulation formats have been shown to have an improved robustness to IFWM. As explained in [36], this improved tolerance is due to antisymmetry of phase alternations in marks surrounding an empty bit slot, which result in cancellation of higher order terms contributing to ghost pulse energy. In [37] similar result has been obtained for alternate-phase return-to-zero modulation format.

In differential phase shift keyed (DPSK) modulated signals, reduced efficiency of intrachannel nonlinearity can be attributed to (i) more evenly distributed signal power [38] and (ii) correlation between nonlinear phase shifts acquired by adjacent bits due to propagation in similar conditions [39]. Indeed, the presence of a pulse in each bit slot prevents ghost pulse generation, while differential phase coding ensures transmission insensitivity to identical phase shifts acquired by adjacent pulses. Moreover, 3 dB increase in the receiver sensitivity suggested by DPSK makes this format particularly attractive for practical implementations. The fact that many of the recently reported distance-capacity records [40–43] have been attained using DPSK demonstrates high potential of the advanced signal modulation.

Vital for 40 Gb/s transmission over ultra-long distances, FEC represents a powerful whilst cost-effective approach to improve the overall quality of information

transfer. More specifically, by appending redundant bits to transmitted messages, FEC permits the correction of transmission errors and a consequent decrease in the transmission bit error rate (BER). Reed Solomon and Bose-Chaudhuri-Hocquenghem codes became widely recognised in fibre-optics communications since they allow a suitable balance between coding gain and decoding complexity. Moreover, good codes of reasonable complexity can be constructed using a concatenation of two codes (see e.g. [44, 45]). In such codes, where messages coding/decoding is conducted by a subsequent coding/decoding by component codes, the coding gain is improved considerably compared to constituent codes gains. Coding performance near to Shannon's limit for Gaussian channels has been demonstrated for iterative coding/decoding algorithms [46, 47]. This advanced iterative decoding is accomplished by cascading soft-input/soft-output decoders in a chain. Such decoders operate with "soft" information comprised of log-likelihood ratios, representing related conditional probabilities to be a mark and a zero for each received bit. The major complexity issue for practical implementation of such advanced decoding algorithms is related to a requirement of a priory knowledge of signal statistical properties for calculating log-likelihood ratios. Vital dependence of present 40 Gb/s transmission on FEC motivates the need for developing existing and novel coding algorithms for future ultra-high bit rate transmission.

1.2 Thesis outline

Focus in this thesis is directed towards the feasibility of suppressing impairments of the ASE noise and nonlinearity, which are crucial for high speed optical signal transmission. The idea of setting a trade-off between these detrimental effects formed the basis for a novel design optimisation technique, introduced in Chapter 2. The proposed approach is applied in order to find the configuration that maximises the system performance in transmission lines with periodic dispersion compensation using Raman and hybrid Raman-EDFA amplification. We also prove the existence of a non-trivial optimal span length for 40 Gb/s WDM transmission using a hybrid amplification scheme.

A statistical analysis of ASE noise is presented in Chapter 3. The chapter begins with a description of the multicanonical Monte Carlo (MMC) method, an efficient numerical technique capable of providing complete information about statistical distributions of optical signals at the receiver. Subsequently, in this chapter we investigate the stochastic properties of soliton parameters by the numerical modelling of the Fokker-Planck equation by applying the MMC simulation technique. After that we examine the BER and compare two commonly used linear approximations to a nonlinear transfer function in transmission systems with 2R inline optical regeneration. Subsequently, we present a study of return-to-zero DPSK (RZ-DPSK) optical signal at direct detection receiver with Mach-Zehnder interferometer demodulation, for which we derive a closed-form analytical expression for the BER in the limit of narrow pulses. The chapter is concluded by a quantitative performance evaluation of a novel 40 Gb/s optical receiver scheme exploiting an all-optical decision element. Finally, the thesis conclusions are given in Chapter 4. In the appendices we summarise the properties of the optical fibres and discuss issues related to computer implementation of the MMC.

Chapter 2

Nonlinearity management

2.1 General principle of nonlinearity management.

Typically the optimum performance in optical long and ultra-long distance transmission is associated with maximum operating length. Hence, the task of system design optimisation boils down to a problem of maximising the transmission distance through variation of system parameters. Such a task, in general, can not be accomplished analytically due to its high complexity. Moreover, extensive numerical optimisation is normally not feasible due to large computational times required by simulations. Therefore, alternative approaches to address this issue are highly desired.

It is widely acknowledged that the performance in modern optical signal quasi-linear transmission is primarily limited by such effects as the accumulated amplifier spontaneous emission (ASE) noise and the nonlinearity. During signal propagation the amplification noise and nonlinear effects accumulate with distance until, eventually, one of the factors exceeds the threshold and the degree of signal degradation becomes unacceptably strong. This serves an indication that the transmission length has attained its upper limit. Essentially, this limit is determined by the most crucial of the two factors. Hence, the optimal performance is achieved when the ASE noise and nonlinearity effectively counterbalance each other. This idea of a balance between two major impairments is implemented in a novel optimisation technique presented in this chapter.

In our approach we measure the noise contribution to the performance degradation by the optical signal-to-noise ratio (OSNR), defined as

$$OSNR = \frac{P_{s0}}{P_{noise}}, \tag{2.1}$$

where the P_{s0} and P_{noise} denote the optical signal and noise powers, respectively. Please note that in (2.1) both signal and noise power are measured within the system bandwidth.

Moreover, if we consider nonlinearities as always contributing to the degradation of the transmission system performance, nonlinear phase shift (NPS) can be considered as a good criterion to measure the impact of nonlinear impairments [48–50]:

$$NPS = \frac{2\pi}{\lambda} \int_{Link} \frac{P_s \cdot n_2}{A_{eff}} dz, \tag{2.2}$$

with the following notations:

P_s the power of signal

λ the signal wavelength,

n_2 the nonlinearity coefficient of the fibre,

A_{eff} the effective area of the fibre,

$Link$ the total transmission link,

However, such a measure in general will require modification in transmission links making a positive use of nonlinearity (e.g. in soliton transmission systems).

Unfortunately, measured in different scales, the effects of the noise and nonlinearity can not be related by a single system performance characteristic. To evade this limitation, we suggest to fix one of these factors (e.g. *OSNR*) and, by varying the launch signal power, optimise the other one (*NPS*). As shown by numerical experiment, such approximated optimal configuration is nearly independent on the chosen value of the first factor *OSNR*, which was selected from a broad range of sensible values. Therefore, it is possible to find the optimal design of a transmission link by performing a conditional minimisation of the *NPS* under a fixed *OSNR*, or vice versa, maximising the *OSNR* for a fixed *NPS*.

Moreover, it is feasible in some cases to perform such an optimisation analytically, by applying the method of Lagrange multipliers. For example, when the transmission line is only equipped with EDFA, or when pump depletion and dou-

ble Rayleigh backscattering are ignored in the case of using Raman amplifiers it is possible to derive the explicit expressions for the *NPS* and *OSNR*, which may subsequently be used in a theoretical optimisation study. The theoretical analysis is presented in Section 2.2. In general, however, numerical modelling is required to determine the optimal design. Section 2.3 is devoted to such numerical optimisation.

2.2 Analytical model

2.2.1 Signal power evolution

In the simplest Raman amplification model signal and pumps powers evolution is governed by the system of coupled ordinary differential equations [51]:

$$\frac{dP_s}{dz} = -\alpha_s P_s + g\left(P_p^+ + P_p^-\right)\left(P_s + n_f\right), \tag{2.3}$$

$$\frac{dP_p^\pm}{dz} = \mp\alpha_p P_p^\pm \mp \frac{\nu_p}{\nu_s} g\left(P_s + n_f\right) P_p^\pm, \tag{2.4}$$

where P_s, P_p^+ and P_p^- represent the signal, forward propagating and backward propagating pump powers; α_s and α_p are the attenuation coefficients at the signal (ν_s) and pump (ν_p) frequencies; and the gain factor g is defined as $g = g_R/A_{eff}$, where g_R is the Raman gain coefficient and A_{eff} is the effective area of the fibre core. The amplification noise in this model is presented by the term $n_f = 2n_{sp}h\nu_s\Delta\nu_s$, where n_{sp}, h and $\Delta\nu_s$ indicate the spontaneous emission factor, Planck constant and bandwidth of transmitted signals, respectively; and the factor 2 is originated from two orthogonal polarisation states.

Before proceeding with transmission lines of more complex configuration, we will find variations of signal power acquired during propagation in a single piece of fibre. Subsequently, we will introduce a simple recursive relation, allowing generalisation of this result to a more practical case of periodic dispersion managed (DM) transmission links. Finally the explicit expressions for the SNR and NPS required for implementing the nonlinearity management approach will be derived.

We commence the analysis of signal dynamics by defining a boundary value problem (BVP) for a piece of fibre of length L. Therefore, we set the boundary con-

ditions for the coupled equations 2.3 and 2.4, as follows

$$P_s(0) = P_{s0}, \tag{2.5}$$

$$P_p^+(0) = P_{p0}^+, \tag{2.6}$$

$$P_p^-(L) = P_{pL}^-, \tag{2.7}$$

where P_{s0} is the launched signal power, P_{p0}^+ represents the co-propagating pump at $z = 0$ and P_{pL}^- is the initial counter-propagating pump injected in the fibre at $z = L$.

As typically only insignificant share of the total pump energy become transferred to the signal frequency via Raman scattering, in the present analysis we neglect the second term in the r.h.s. of equations 2.4, which is responsible for the pump depletion. As a result, equations 2.4 can be solved by integration and, using boundary conditions 2.6 and 2.7, we get:

$$P_p^+(z) = P_{p0}^+ e^{-\alpha_p z},$$
$$P_p^-(z) = P_{pL}^- e^{-\alpha_p (L-z)}.$$

Incorporating these expressions in equation 2.3 yields the following inhomogeneous ordinary differential equation for the signal power:

$$\frac{dP_s}{dz} = \mathcal{A}(z) P_s + \mathcal{N}(z), \tag{2.8}$$

where

$$\mathcal{A}(z) = -\alpha_s + g\left(P_{p0}^+ e^{-\alpha_p z} + P_{pL}^- e^{-\alpha_p (L-z)}\right), \tag{2.9}$$

$$\mathcal{N}(z) = n_f g\left(P_{p0}^+ e^{-\alpha_p z} + P_{pL}^- e^{-\alpha_p (L-z)}\right). \tag{2.10}$$

The standard approach to solving equations of such a kind is to present the solution in a form of a product of two functions:

$$P_s = \mathcal{G}(z)\,\mathcal{F}(z), \tag{2.11}$$

with one function satisfying the corresponding homogeneous equation

$$\frac{d\mathcal{G}(z)}{dz} = \mathcal{A}(z)\,\mathcal{G}(z), \tag{2.12}$$

and the other one calculated by solving the equation

$$\frac{d\mathcal{F}(z)}{dz} = \frac{\mathcal{N}(z)}{\mathcal{G}(z)}, \tag{2.13}$$

which comes after substituting equation (2.11) in equation (2.8).

The solution to equation 2.12 yields

$$\mathcal{G}(z) = C \exp\left(-\alpha_s z - G_0^+ \frac{e^{-\alpha_p z}}{\alpha_p} + G_0^- \frac{e^{\alpha_p z}}{\alpha_p}\right), \tag{2.14}$$

where

$$G_0^+ = g P_{p0}^+, \tag{2.15}$$

$$G_0^- = g P_{pL}^- e^{-\alpha_p L}, \tag{2.16}$$

and C is an arbitrary constant. Moreover, integrating equation 2.13 and using boundary condition 2.5 one finds that

$$\mathcal{F}(z) = \int_0^z \frac{\mathcal{N}(z)}{\mathcal{G}(z)} dz + \frac{P_{s0}}{\mathcal{G}(0)}. \tag{2.17}$$

After substituting $\mathcal{G}(z)$ and $\mathcal{G}(0)$ from equation 2.14 into equation 2.17, $\mathcal{F}(z)$ reads:

$$\mathcal{F}(z) = n_f \mathcal{J} + P_{s0} \exp\left(\frac{G_0^+}{\alpha_p} - \frac{G_0^-}{\alpha_p}\right), \tag{2.18}$$

where the variable $\mathcal{J}$ represents the integral:

$$\mathcal{J}(z) = \int_1^{e^{\alpha_p z}} t^{\frac{\alpha_s}{\alpha_p} - 1} \left(\frac{G_0^+}{\alpha_p t} + \frac{G_0^- t}{\alpha_p}\right) \exp\left(\frac{G_0^+}{\alpha_p t} - \frac{G_0^- t}{\alpha_p}\right) dt.$$

Finally, combining the equations 2.11, 2.14 and 2.18, the sought signal power yields the solution:

$$P_s(z) = G(z) P_{s0} + n(z), \tag{2.19}$$

where

$$G(z) = \exp\left(-\alpha_s z + g P_{p0}^+ \frac{1 - e^{-\alpha_p z}}{\alpha_p} + g P_{pL}^- \frac{e^{-\alpha_p (L-z)} - e^{-\alpha_p L}}{\alpha_p}\right), \tag{2.20}$$

$$n(z) = n_f \mathcal{J} \exp\left(-\alpha_s z + g P_{p0}^+ \frac{e^{-\alpha_p z}}{\alpha_p} + g P_{pL}^- \frac{e^{-\alpha_p (L-z)}}{\alpha_p}\right) \tag{2.21}$$

and

$$\mathcal{J}(z) = \int_1^{e^{\alpha_p z}} t^{\frac{\alpha_s}{\alpha_p} - 1} \left(\frac{g P_{p0}^+}{\alpha_p t} + \frac{g P_{pL}^- e^{-\alpha_p L} t}{\alpha_p}\right) \exp\left(\frac{g P_{p0}^+}{\alpha_p t} - \frac{g P_{pL}^- e^{-\alpha_p L} t}{\alpha_p}\right) dt. \tag{2.22}$$

To facilitate the derivation of the OSNR, it is important to discriminate the propagating signal from accumulated noise in equation 2.19. The term $n(z)$ seems to be

a reasonable indicator of noise. Indeed, in the absence of input signal it remains a sole constituent of $P_s(z)$. Furthermore, the evolution of signals in equation 2.19 is described by the coefficient $G(z)$, governing the Raman gain and fibre losses.

In a specific case of only backward propagating pump, i.e. $P^+_{p0} = 0$, the integral $\mathcal{J}(z)$ can be rewritten in terms of the incomplete gamma function γ

$$\mathcal{J}'(z) = \left(\frac{g}{\alpha_p}P^-_{pL}\right)^{-\frac{\alpha_s}{\alpha_p}} \left(\gamma\left(\frac{\alpha_s}{\alpha_p}+1, \frac{g}{\alpha_p}P^-_{pL}e^{-\alpha_p(L-z)}\right) - \gamma\left(\frac{\alpha_s}{\alpha_p}+1, \frac{g}{\alpha_p}P^-_{pL}e^{-\alpha_p L}\right)\right) e^{-\alpha_s L}. \tag{2.23}$$

2.2.2 Dispersion management case.

Before discussing the case of DM transmission line, we rewrite the formulas 2.20 and 2.21 for $z = L$:

$$G = \exp\left(-\alpha_s L + gL_{eff}\left(P^+_{p0} + P^-_{pL}\right)\right), \tag{2.24}$$

$$\begin{aligned} n = {} & n_f g \exp\left(-\alpha_s L + \frac{g}{\alpha_p}\left(-P^+_{p0}e^{-\alpha_p L} + P^-_{pL}\right)\right) \int_0^{L_{eff}} (1-\alpha_p u)^{-\frac{\alpha_s}{\alpha_p}-1} \\ & \exp\left(\frac{gP^+_{p0}(1-\alpha_p u)}{\alpha_p} - \frac{gP^-_{pL}e^{-\alpha_p L}}{\alpha_p(1-\alpha_p u)}\right)\left(P^+_{p0}(1-\alpha_p u) + \frac{P^-_{pL}e^{-\alpha_p L}}{1-\alpha_p u}\right) du. \end{aligned} \tag{2.25}$$

Here we employed a concept of the effective transmission length, defined as

$$L_{eff} = \frac{1-e^{-\alpha_p L}}{\alpha_p}. \tag{2.26}$$

Equipped with formulas for a single fibre section, we can model a single amplification period composed by N different fibre segments $L = L_1 + L_2 + \cdots + L_N$. In the following analysis we assume that pumps P^+_{p0} and P^-_{pL} are fed into the input and the output ends of the span L.

Therefore, in the i-th fibre section (for an arbitrary $i : 1 \le i \le N$) the initial co- and counter-propagating pump intensities are given by

$$P^+_{p0i} = P^+_{p0}e^{-\sum_{j=1}^{i-1}\alpha_{pj}L_j}, \tag{2.27}$$

$$P^-_{pLi} = P^-_{pL}e^{-\sum_{j=i+1}^{N}\alpha_{pj}L_j}. \tag{2.28}$$

Moreover, the output signal of the $(i-1)$-th section becomes the input to the i-th section $(2 \leq i \leq N)$:

$$P_{si} = G_i P_{s(i-1)} + n_i. \tag{2.29}$$

After applying this recursive relation N times, one gets the expression for signals at $z = L$:

$$P_s = G P_{s0} + n, \tag{2.30}$$

where the gain/losses coefficient G and the noise term n satisfy the relations

$$G = \prod_{i=1}^{N} G_i, \tag{2.31}$$

$$n = \sum_{i=1}^{N} \left(n_i \prod_{j=i+1}^{N} G_j \right), \tag{2.32}$$

where

$$G_i = \exp\left(-\alpha_{si} L_i + g_i L_{eff\,i} \left(P^+_{p\,0i} + P^-_{p\,Li}\right)\right), \tag{2.33}$$

$$\begin{aligned} n_i = {} & n_{f\,i} g_i \exp\left(-\alpha_{si} L_i - \frac{g_i}{\alpha_{pi}} \left(P^+_{p\,0i} e^{-\alpha_{pi} L_i} - P^-_{p\,Li}\right)\right) \int_0^{L_{eff\,i}} (1 - \alpha_{pi} u)^{-\frac{\alpha_{si}}{\alpha_{pi}} - 1} \\ & \exp\left(\frac{g_i P^+_{p\,0i} (1 - \alpha_{pi} u)}{\alpha_{pi}} - \frac{g_i P^-_{p\,Li} e^{-\alpha_{pi} L_i}}{\alpha_{pi} (1 - \alpha_{pi} u)}\right) \left(P^+_{p\,0i} (1 - \alpha_{pi} u) + \frac{P^-_{p\,Li} e^{-\alpha_{pi} L_i}}{1 - \alpha_{pi} u}\right) du. \end{aligned} \tag{2.34}$$

with $L_{eff\,i} = \left(1 - e^{-\alpha_{pi} L_i}\right) / \alpha_{pi}$ the effective length of the i-th fibre section and $P^+_{p\,0i}$ and $P^-_{p\,Li}$ the pumps introduced by formulas 2.27 and 2.28.

As a final step in modelling Raman amplification in DM transmission lines, now we consider a link consisting of several amplification periods, i.e.

$$\mathbf{L} = m \times L = m \times (L_1 + L_2 + \cdots + L_N).$$

Using the recursive relation 2.29 for a sequence of such periods, it is easy to get the signal at the end of the entire link

$$\mathbf{P_s} = \mathbf{G} P_{s0} + \mathbf{n}. \tag{2.35}$$

where

$$\mathbf{G} = G^m, \tag{2.36}$$

$$\mathbf{n} = \left(G^{m-1} + G^{m-2} + \cdots + 1\right) n = \frac{1 - G^m}{1 - G} n, \tag{2.37}$$

and G and n denote the gain/losses factor and the noise for a single span, derived by the expressions 2.31 and 2.32.

Substantial simplification of these formulas is possible in the case where total pump power is adjusted so that the initial signal power is recovered at the end of the amplification period. Then, we have $G \equiv 1$ and the formulas 2.36 and 2.37 take the form

$$\mathbf{G} = 1, \tag{2.38}$$

$$\mathbf{n} = m \cdot n. \tag{2.39}$$

2.2.3 Optical signal to noise ratio and nonlinear phase shift

In a DM transmission line composed of several amplification spans with each span consisting of sections of positive and negative dispersion fibres, the solution to the coupled equations 2.3 and 2.4 reads the expression 2.35. In expression 2.35 the signal term is expressed by $\mathbf{G}P_{s0}$ and the noise component is presented by $\mathbf{n}$. When pump energy is chosen to exactly compensate for losses acquired by signals during propagation in one amplification span, as typically done in signal transmission, the $\mathbf{G}$ become 1 and $\mathbf{n}$ is given by combination of formulas 2.39 and 2.32. Therefore, the *OSNR* as defined by equation 2.1 reads

$$OSNR = \frac{P_{s0}}{m \cdot \sum_{i=1}^{N} \left(n_i \prod_{j=i+1}^{N} G_j \right)}. \tag{2.40}$$

Now we derive an expression for the *NPS* for a conventional DM transmission link. Due to the additivity of integration, the phase shift is also additive with respect to fibre sections that comprise the total link. Hence, from equations 2.20 and 2.2, the *NPS* for a single amplification span $L = L_1 + L_2 + \cdots + L_N$ reads

$$NPS = \frac{2\pi}{\lambda} P_{s0} \sum_{i=1}^{N} \frac{n_{2i}}{A_{eff\,i}} \prod_{k=1}^{i-1} G_k \exp\left(\frac{g_i P_{p\,0i}^{+}}{\alpha_{pi}} - \frac{g_i P_{p\,Li}^{-} e^{-\alpha_{pi} L_i}}{\alpha_{pi}} \right) I_i, \tag{2.41}$$

where

$$I_i = \int_0^{L_{eff\,i}} (1 - \alpha_{pi} u)^{\frac{\alpha_{si}}{\alpha_{pi}} - 1} \exp\left(-\frac{g_i P_{p\,0i}^{+} (1 - \alpha_{pi} u)}{\alpha_{pi}} + \frac{g_i P_{p\,Li}^{-} e^{-\alpha_{pi} L_i}}{\alpha_{pi} (1 - \alpha_{pi} u)} \right) du, \tag{2.42}$$

and $P^{+}_{p\,0i}$ and $P^{-}_{p\,Li}$ are as presented by equations 2.27 and 2.28. For m identical spans of length L and complete restoration of the signal power in each span the *NPS* due to its additive properties becomes multiplied by the factor m.

In some cases the approximate expressions (2.40, 2.41) can be used in analytical optimisation, e.g. by the method of Lagrange multipliers, or serve as a first estimate. However, in general, an accurate and complete analysis requires a numerical approach, in particular, in systems with strong impact of the DRS and/or pump depletion.

2.3 Numerical modelling

To include the effect of DRS the power equations model of equations (2.3, 2.4) should be altered to:

$$\begin{aligned}
\frac{dP_s}{dz} &= -\alpha_s P_s + g\left(P_p^{+} + P_p^{-}\right) P_s, \\
\frac{n_s^{+}}{dz} &= -\alpha_s n_s^{+} + g\left(P_p^{+} + P_p^{-}\right)\left(n_s^{+} + n_f\right) + \varepsilon n_s^{-}, \\
\frac{n_s^{-}}{dz} &= \alpha_s n_s^{-} - g\left(P_p^{+} + P_p^{-}\right)\left(n_s^{-} + n_f\right) - \varepsilon\left(n_s^{+} + P_s\right), \\
\frac{dP_p^{\pm}}{dz} &= \mp\alpha_p P_p^{\pm} \mp \frac{\nu_p}{\nu_s} g\left(P_s + n_f\right) P_p^{\pm};
\end{aligned} \tag{2.43}$$

where ε denotes the backscattering coefficient of the propagating fibre. Without loss of generality, we choose to consider dynamics of the signal (P_s) and forward (n_s^{+}) and backward (n_s^{-}) propagating noise confined within the same frequency bandwidth $\nu_s \pm \Delta\nu_s/2$ in separate equations. Through such an approach it became possible to introduce in the model the effect of DRS. Moreover, such separation of the optical amplification noise from the launched signal permits to perform a direct measurement of the *OSNR*.

Rested on a concept of the nonlinearity management, the optimisation suggested in this chapter requires solving the BVP set using the system of coupled ordinary differential equations (2.43) and boundary conditions (2.5, 2.6, 2.7). The boundary

conditions for the noise were defined as

$$n_s^+(0) = 0, \tag{2.44}$$

$$n_s^-(L) = 0. \tag{2.45}$$

In our analysis we used a freely distributed package COLSYS, designed by U. Archer, J. Christiansen and R. D. Russel [52, 53] for solving BVP. The spline collocation method implemented in COLSYS, similarly to other collocation techniques, approximates a solution to a given problem by a linear combination of basis functions. The coefficients in linear combination are found by substituting the solution anzatz in the problem at so called "collocation" points, a set of points chosen carefully to attain maximum efficiency of the algorithm. In general, the collocation methods are applicable to a range of problems, including solving differential and integral equations. Due to simplicity of differentiation of polynomials the spline collocation technique has become well acknowledged for its effectiveness in solving BVPs. In simulations we used a tolerance of 10^{-8} on determination of the average powers.

Solving the BVP for equations (2.43) is essential for performing the optimisation procedure, as it allows to approximate the noise and signal powers and estimate the *OSNR*. The *NPS* in our simulations was calculated with the aid of trapezoidal rule, a standard tool for numerical integration. This third order accurate method is based on the following approximation

$$\int_a^b f(x)\,dx \approx \sum_{i=1}^{n} \frac{f(x_i)+f(x_{i-1})}{2} h = \left(\frac{f(x_0)}{2} + \sum_{i=1}^{n-1} f(x_i) + \frac{f(x_n)}{2} \right) h, \tag{2.46}$$

where $x_0 = a, x_1, \ldots, x_n = b$ represent a set of equally spaced by h points within the interval of integration. As such, the area under the graph between points x_{i-1} and x_i become estimated by the area of the corresponding trapezium with the parallel sides of lengths $f(x_{i-1})$ and $f(x_i)$ and the height h.

To find the optimal state, or in other words, the state of a balance between the noise and nonlinearity one can fix the *OSNR* and minimise the *NPS* with respect to varying parameters of the system. In our simulations we retained the *OSNR* assigned to some value by adjusting the power of launched signals for each set of optimisation parameters. Subsequently, we observed variations of the *NPS* by changing the values of the optimisation parameters and found its minimum.

Note that both the output *OSNR* and *NPS* depend on the input signal power. Thus, the minimisation of the NPS under the requirement of a fixed value of the output OSNR will at the same time determine a certain signal power. Therefore, we additionally verify that variations of the output OSNR do not change the optimal configuration significantly, so the minimum bit-error-rate in the signal power interval in which we are most interested will be obtained.

In simulations, the problem of adjusting the launch signal powers to maintain the fixed OSNR was solved with the aid of a relaxation algorithm. Basically, this iterative algorithm is applicable to solving an arbitrary equation of the kind

$$f(x) = c \tag{2.47}$$

and could be represented by a simple recursive relation:

$$x_{i+1} = \mu x_i \frac{c}{f(x_i)} + (1-\mu)x_i, \tag{2.48}$$

where μ is a relaxation parameter and x_0 is an initial guess for the solution x. Moreover, as the convergence rate of this technique is strongly dependent on the coefficient μ, in simulations the μ was adjusted "by hand" to maximise the method's efficiency. Another important application of this algorithm is related to calculations of the Raman pump power required to ensure exact compensation of signal losses in a single amplification span.

In order to accomplish minimisation of the *NPS*, we used effective and simple for implementation iterative method of gold section search [54]. Being an analogy to bisection method for finding zeros, this optimisation technique accomplishes a search for a function extreme points located within a given interval.

2.4 Optical fibre link with backward Raman amplification

Conventionally, in optical signal transmission the pulse broadening, timing jitter and other impairments associated with dispersion are approached through a technique of dispersion compensation (DC). Moreover, Raman amplification which generally suggests a better noise performance [55] and reduced nonlinear effects [56],

represents an advantageous alternative to traditional EDFA-based lumped amplifiers. Due to these properties, distributed Raman amplification (DRA) has become particularly attractive for quasi-linear optical communications, where nonlinearity is always assumed to be detrimental. An appropriate combination of DM and DRA can provide an important improvement in system efficiency.

Fibres with small effective area, such as dispersion compensating fibres (DCF) are more efficient in Raman conversion, and will usually provide higher Raman gains. On the other hand these fibres also present higher nonlinear and Rayleigh back scattering coefficients, which can degrade the system performance if they receive direct Raman pumping from a strong source or if they are placed close enough to the Raman pump. The optimal location of the DCF inside the dispersion map, for example, between two pieces of transport fibre, can produce an appreciable reduction of non-linear induced interactions and DRS induced noise. Futhermore, with some control of the gain distribution over the span, noise generation from ASE becomes possible.

In systems with backward Raman amplification propagating signals attain the maximum power at the beginning and at the end of amplification spans. Therefore, by locating a segment of DCF in the middle section of the span it is possible to reduce the nonlinear effects accumulated in transmission. However, signal power distribution is assymetric along the span. Moreover, the interaction between the nonlinearity issues, DRS effect and Raman gain factor makes determining the precise optimal location for the DCF a tricky problem, in general.

To evaluate the system performance, we address the nonlinearity management approach of section 2.1. In this respect, we find the optimal configuration, which either maximises the output *OSNR* for a given *NPS*, or minimize the *NPS* for a given *OSNR*.

In particular, we consider a transmission line with counterpropagating Raman amplification, shown on a schematic setup of Figure 2.1. On the plot the "Fibre_1" and "Fibre_2" represent a standard transport and dispersion compensating fibres, respectively. It is customary to describe the location of DCF within the amplification

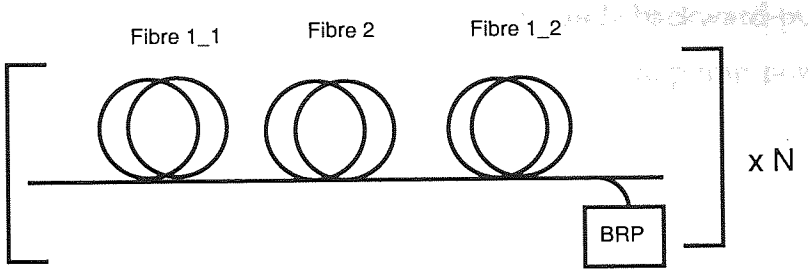

Figure 2.1: Schematic setup of configuration 1. The BRP denotes the backward Raman pump source.

span by introducing an optimisation parameter η

$$\eta = \frac{L_{fibre\_1\_1}}{L_{fibre\_1,Total}}. \tag{2.49}$$

Using the analytical model of section 2.2, we derive the approximate expressions for the *OSNR* and *NPS*:

$$OSNR = \frac{P_{s0}}{m \times (n_1 G_2 G_3 + n_2 G_3 + n_3)}, \tag{2.50}$$

$$NPS = m \times \frac{2\pi P_{s0}}{\lambda} \sum_{i=1}^{3} \frac{n_{2i} \prod_{k=1}^{i-1} G_k}{A_{eff\,i}} \exp\left(-\frac{g_i}{\alpha_{pi}} P^-_{p\,Li} e^{-\alpha_{pi} L_i}\right) I_i, \tag{2.51}$$

where, in the case of only backward pumping,

$$G_i = \exp\left(-\alpha_{si} L_i + g_i P^-_{p\,Li} L_{eff\,i}\right), \tag{2.52}$$

$$n_i = n_{f\,i} J_i \exp\left(\frac{g_i}{\alpha_{pi}} P^-_{p\,Li}\right), \tag{2.53}$$

with J_i and I_i given by

$$J_i = \left(\frac{g_i}{\alpha_{pi}} P^-_{p\,Li}\right)^{-\frac{\alpha_{si}}{\alpha_{pi}}} \left(\gamma\left(\frac{\alpha_{si}}{\alpha_{pi}} + 1, \frac{g_i}{\alpha_{pi}} P^-_{p\,Li}\right) - \gamma\left(\frac{\alpha_{si}}{\alpha_{pi}} + 1, \frac{g_i}{\alpha_{pi}} P^-_{p\,Li} e^{-\alpha_{pi} L_i}\right)\right) \tag{2.54}$$

$$I_i = \int_0^{L_{eff\,i}} (1 - \alpha_{pi} u)^{\frac{\alpha_{si}}{\alpha_{pi}} - 1} \exp\left(\frac{g_i}{\alpha_{pi}} P^-_{p\,Li} e^{-\alpha_{pi} L_i} (1 - \alpha_{pi} u)^{-1}\right) du. \tag{2.55}$$

$P^-_{p\,Li}$ yields expression 2.28. Recall, that $L_{eff\,i} = \left(1 - e^{-\alpha_{pi} L_i}\right) / \alpha_{pi}$ represents the effective length of i-th fibre segment. In equations (2.50-2.55), index 1 corresponds to Fibre 1_1, index 2 refers to Fibre 2 and index 3 refers to Fibre 1_2 (see Figure 2.1). All other notations are as introduced in sections 2.1 and 2.2.

Although, the analytical expressions (2.50, 2.51) can provide a good approximation in some range of input signal and pump powers, the full numerical approach

has been taken, given that the influence of DRS in a purely backward-pumped configurations can be strong, depending on factors such as total pump power and the proximity of the small effective area DCF to the pump.

When addressing numerically the task of evaluating the optimal η (2.49) in the configuration of Figure 2.1, we specify the parameters as follows. We consider a cascade of fibre spans constructed by 100 km of SMF ("fibre 1") and 17 km of DCF ("fibre 2"). The length of DCF here is adjusted so that the span average dispersion is zero. The fibre parameters are summarised in Table A.1 of Appendix A. The Raman gain coefficient presented is for a depolarised pump, and as such has been divided by a polarisation factor of 2. In the link we launch an RZ signal at 40 Gb/s with power centred at 1550 nm and a backward propagating pump at 1455 nm. The total bandwidth of 400 nm became assigned to the signal in order to accommodate four channels spaced at 100 nm. Moreover, the Raman pump power was adjusted to fully compensate for signal attenuation in one span.

The optimal η can be found by maximising the output *OSNR*, while keeping the *NPS* constant. This approach became illustrated on Figure 2.2, where the *OSNR* is plotted with respect to η for two different values of the *NPS* accumulated after 10 spans. We observe that the maximal *OSNR* is reached for quite a broad range of η extending from 0.1 to 0.25. As the *NPS* increases so does the required pump power for full recovery of the signal, and the optimal position of the DCF is displaced further away from the pump, towards the beginning of the span.

This plot identifies an optical range from 10% to 25% for the SMF1/SMF ratio where the optimal cell configuration is obtained. Lines within this range represent the best trade-off, as not only the gain is optimally distributed over the span length in order to reduce the noise built-up, but also nonlinear effects are reduced, with lower pulse peak power at the input of the DCF section. This result is general, as the range associated with maximum *OSNR* is nearly the same irrespectively of the used *NPS*. The underlying idea of the nonlinearity management technique is well presented in Figure 2.3, where the NPS and OSNR evolution is plotted over a single propagation span for two distinct values of the optimisation parameter η. Importantly, the considered configurations exploit different launch signal powers in order

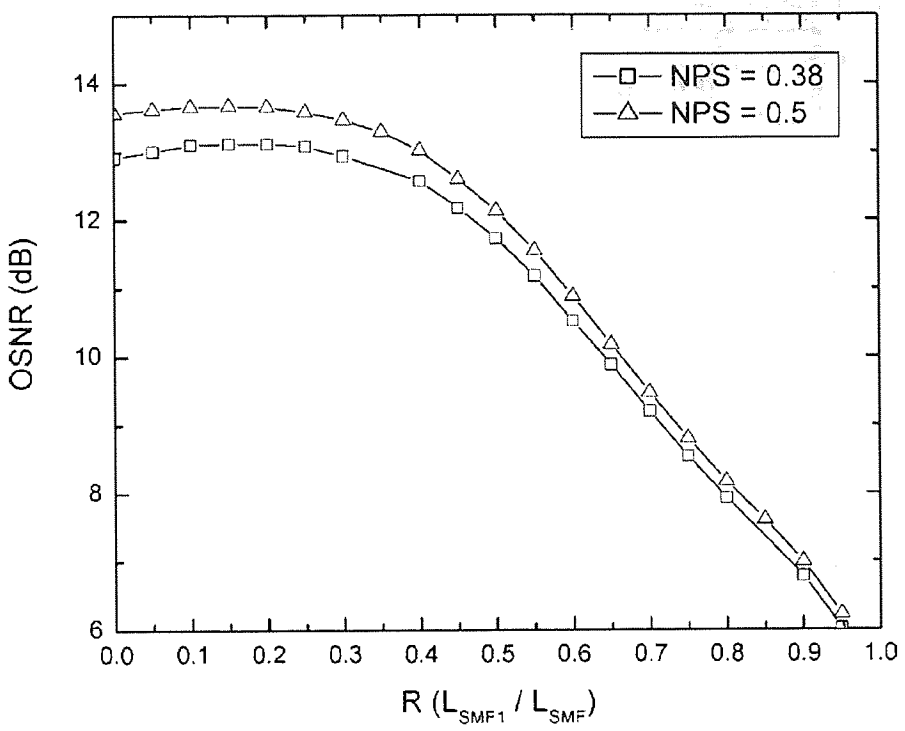

Figure 2.2: The *OSNR* plotted as a function of the parameter η for some fixed values of the *NPS* after 10 spans.

to attain the identical output OSNR. Subsequently, by comparing the values of the NPS at the span output it is possible to determine which of the two transmission system configurations suggests a better balance between the noise and nonlinear effects. As such, the figure shows that the accumulated nonlinearity becomes sufficiently reduced for the configuration with $\eta = 0.2$, compared to the symmetric map ($\eta = 0.5$), which indicates an improved performance demonstrated by this system. In order to confirm this result under realistic conditions we conducted simulations based on a full numerical model, which solves the nonlinear Schrödinger equation by applying to it the split-step Fourier method (see e.g. [57]). This work was carried out in collaboration with a research group from Novosibirsk. As such, Figure 2.4 shows the evolution of the maximum transmission distance with the position of the DCF for a four-channel 40 Gb/s 82.9 km periodic link with zero average dispersion, where we define the maximum transmission distance as a distance at which the Q-factor drops below 6. It is seen that the optimal performance is attained for $\eta = 0.25$, which is in excellent agreement with the results of Figure 2.2. As predicted by the

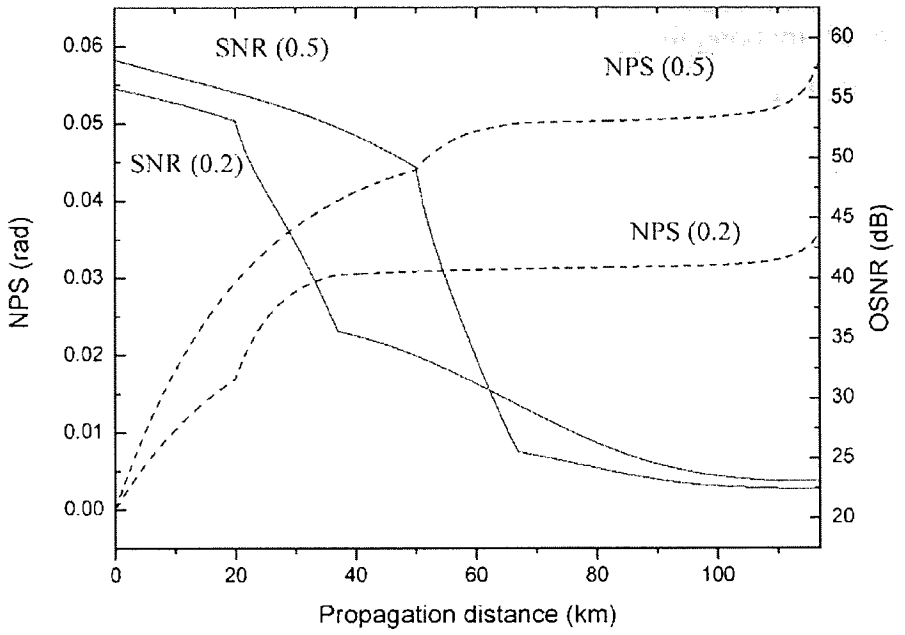

Figure 2.3: The *OSNR* and *NPS* plotted against propagation distance within one amplification span for two configurations ($\eta = 0.2$ and $\eta = 0.5$). The *OSNR* is adjusted to have the same output value.

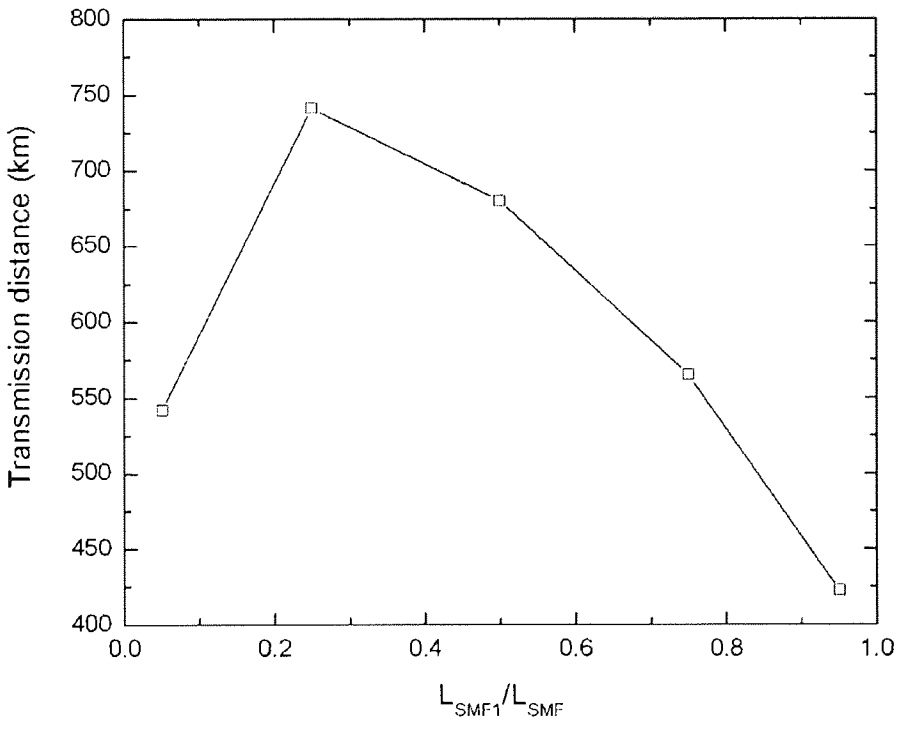

Figure 2.4: Evolution of the maximum transmission distance versus η, approximated using the full numerical model.

simpler analysis based on the integration of the coupled average power equations, the accumulation of noise and nonlinearities is strongly dependent on the ratio η. This dependence is directly reflected on the maximum transmission distance achievable by the system.

In summary, we have applied the nonlinearity management technique to optimisation of the location of DCF in the SMF/DCF link with backward Raman amplification. In particular, we determined that the balance between the noise and nonlinear impairments is attained for the configuration SMF(10%-25%)+DCF+SMF(90%-75%) for the distance considered 1000 km of SMF. These results show an excellent agreement with the ones found with the aid of the full numerical model.

2.5 Optical fibre link with bidirectional Raman amplification

Distributed amplification based on the Raman effect allows for a greater control of the signal power within the transmission line, and thus of the nonlinear effects, as well as it usually delivers better noise performance compared to conventional amplification schemes based on EDFAs. Moreover, DM has become widely acknowledged for its efficiency in approaching the nonlinearity. Therefore, the build-up of noise and accumulated nonlinearity (the factors that mostly limit the performance in modern optical communications) can be managed by system design. In view of this fact and due to constantly growing demands for a better performance, design optimisation in DM transmission links with distributed Raman amplification is very important.

As discussed in previous sections, the best performance of a fibre transmission system is achieved when the optimal compromise between the requirements of high *OSNR* and minimal nonlinear impairments is found. This principle, implemented in the "nonlinearity management" technique, is applied to a transmission link with a dispersion map shown on Figure 2.5. As such, the considered map consists of three sections, built with transport "fibre 1" sections 1 and 3) and dispersion compensating "fibre 2" (section 2).

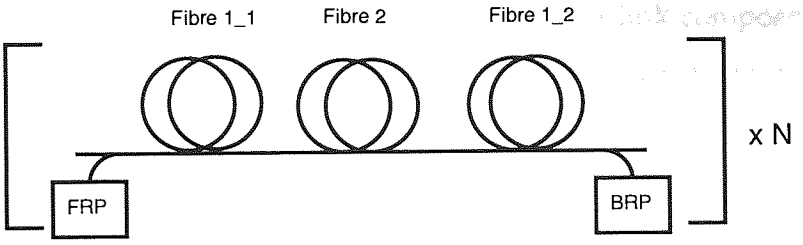

Figure 2.5: Schematic setup of configuration 2.

Two parameters can be optimised in this system: the pumping scheme, represented by η_1 (ratio of the power in the forward pump to the total pump power) and the dispersion map, represented by η_2 ratio of the length of the first piece of "fibre 1" to the total length of "fibre 1"):

$$\eta_1 = \frac{\textit{forward propagating pump power}}{\textit{total pump power}}, \tag{2.56}$$

$$\eta_2 = \frac{L_{\textit{fibre 1, 1}}}{L_{\textit{fibre 1, Total}}}. \tag{2.57}$$

Under the assumption of undepleted pumps and neglecting the effect of double Rayleigh scattering (DRS), it is in general possible to obtain analytical expressions for the evolution of the *OSNR* and the *NPS* in an optically amplified dispersion-managed line. Calculated with the aid of analysis of section 2.2, these expressions read

$$OSNR = \frac{P_{s0}}{m \times (n_1 G_2 G_3 + n_2 G_3 + n_3)}, \tag{2.58}$$

$$NPS = m \times \frac{2\pi}{\lambda} P_{s0} \sum_{i=1}^{3} \frac{n_{2i} \prod_{k=1}^{i-1} G_k}{A_{eff\,i}} \exp\left(-\frac{g_i}{\alpha_{pi}} P^{-}_{p\,Li} e^{-\alpha_{pi} L_i} \right) I_i, \tag{2.59}$$

where G_i and n_i are introduced by relations 2.33 and 2.34. All notations used in these formulas are defined in section 2.2. The indices 1 and 3, moreover, correspond to the transport fibre ("fibre 1 1" and "fibre 1 2", respectively, on the schematic of Figure 2.5), and index 2 is for the segment of DCF ("fibre 2").

However, in general, it is necessary to apply numerical modelling to find the optimal design. In the numerical approach, the system of coupled differential equations for the pump, signal and noise power evolution, taking into account DRS and pump depletion (2.43) is solved, and the *OSNR* and *NPS* are calculated from the resulting power evolutions.

As an illustrative example, we consider a cascaded link composed by sections of Ultrawave super-large-effective-area (SLA) fibre and Ultrwave inverse dispersion fibre (IDF), denoted by fibre 1 and fibre 2 respectively in Figure 2.5. The fibre parameters are described in Appendix A, where ε represents the Rayleigh backscattering coefficient. The periodic cell has a total length of 100 km with zero average dispersion. The total length of SLA fibre is set to 66.67 km, whereas the length of IDF is 33.33 km. The signal consists of 4 channels equally spaced around 1550 nm, with an allocated optical signal bandwidth of 100 GHz for each channel, and the total pump power is always adjusted so that the total signal attenuation at the end of the span is zero.

Figure 2.6 displays the *NPS* versus the parameter η_2 for fixed values of η_1 (0.5) and of the output *OSNR* after one span (25 dB). The analytical and the numerical results show very good agreement, with the biggest differences found in the situations in which the fibre with the smaller effective area (IDF) is set closer to one of the pumps ($\eta_2 = 0$ *or* 1). But most important, both curves present a minimum at $\eta_2 = 0.7$, corresponding to a non-symmetrical split of the SLA fibre. The position of this minimum is constant for any fixed value of the output OSNR, so we can conclude that this is the optimal η_2 for the chosen pump configuration (defined by η_1). This fact justifies an appreciable accuracy of the theoretical analysis of section 2.2.

In order to get a complete optimisation of the system, however, it is still necessary to consider simultaneously the variation of both parameters. Figure 2.7 shows in a contour plot the variation of the NPS vs. η_1 and η_2 again for a fixed value of the output SNR of 25 dB. The plot, obtained by applying a full numerical analysis, shows a clear minimum for the NPS around the coordinates (0.5, 0.7). This point remains constant with variations of the output OSNR, so it can be considered to simultaneously define the optimal configuration for the dispersion map and the pumping scheme. The same result is obtained using the analytical approximation, although the particular value of the minimum NPS differs slightly, as seen in Figure 2.6.

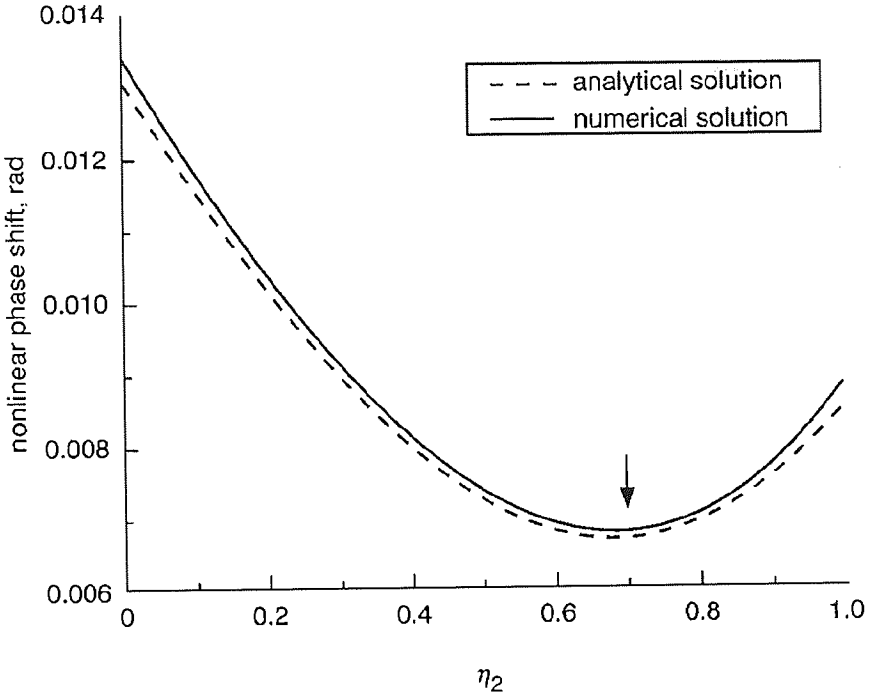

Figure 2.6: Numerical and analytical *NPS* with respect to η_2 for $OSNR = 25dB$ and $\eta_1 = 0.5$.

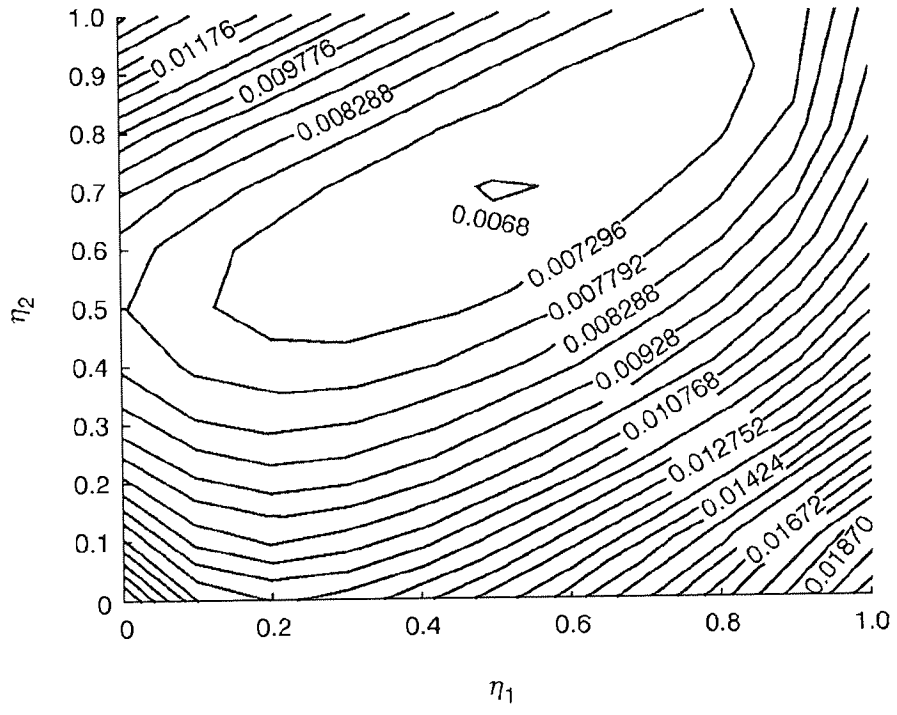

Figure 2.7: *NPS* plotted against η_1 and η_2 for a fixed $OSNR = 25dB$.

2.6 Optical fibre links with hybrid Raman-EDFA amplification

Distributed amplification based on the Raman effect allows for a greater control of the signal power within the transmission line, and thus of the nonlinear effects, as well as usually delivering better noise performance compared to amplification schemes based solely on EDFAs. Both amplification methods can be combined in hybrid schemes in order to obtain some benefits, such as gain equalisation or noise reduction, together with simultaneous dispersion compensation. On the other hand, transmission systems with Raman amplification suffer a disadvantage of reinforcing the effect of DRS, which may contribute to the degradation of the *OSNR*. This issue becomes particularly important in dispersion compensating fibres, which have a smaller effective core area, and hence have a higher DRS coefficient. Some reduction to this negative effect, however, is possible by using a transmission link schematically shown on Figure 2.8, since in this case DCF is not affected by DRS. (On Figure 2.12 fibre 1 denotes the transport fibre, while fibre 2 is for a dispersion compensating fibre.)

Similar to the analysis of previous sections, we accomplish design optimisation to a link presented on Figure 2.12 by performing a conditional minimisation of the *NPS* under a fixed optical *OSNR*, or vice versa, maximising the *OSNR* for a fixed *NPS*.

An important optimisation characteristic of the hybrid amplification dispersion compensation module is the ratio η between the on-off gain provided by the Raman amplifier and the total gain in the span, both in (dB),

$$\eta = \frac{G_{Raman}}{G_{Total}}. \tag{2.60}$$

Under the assumption of undepleted pumps and without taking into account DRS, analytical expressions for the *OSNR* (in dB) and the *NPS* of each channel can be obtained:

$$OSNR = \frac{P_{s0}\,G}{m \times \left(n + Fe^{\alpha_{p2}L_2}\right)}, \tag{2.61}$$

$$NPS = m \times \frac{2\pi}{\lambda} P_{s0} \left(\frac{n_{21}}{A_{eff\,1}} I + \frac{n_{22}}{A_{eff\,2}} \frac{1 - e^{-\alpha_{s2}L_2}}{\alpha_{s2}} G \right), \tag{2.62}$$

where

$$G = \exp\left(-\alpha_{s1}L_1 + g_1 P_p^- L_{eff\,1}\right), \tag{2.63}$$

$$n = n_{f1} J \exp\left(-\alpha_{s1}L_1 + \frac{g_1}{\alpha_{p1}}P_p^-\right), \tag{2.64}$$

with J and I defined as

$$J = \left(\frac{g_1}{\alpha_{p1}}P_p^- e^{-\alpha_{p1}L_1}\right)^{-\frac{\alpha_{s1}}{\alpha_{p1}}} \left(\gamma\left(\frac{\alpha_{s1}}{\alpha_{p1}}+1, \frac{g_1}{\alpha_{p1}}P_p^-\right) - \gamma\left(\frac{\alpha_{s1}}{\alpha_{p1}}+1, \frac{g_1}{\alpha_{p1}}P_p^- e^{-\alpha_{p1}L_1}\right)\right),$$

$$I = \int_0^{L_1} \exp\left(-\alpha_{s1}z + \frac{g_1}{\alpha_{p1}}P_p^-\left(e^{-\alpha_{p1}(L_1-z)} - e^{-\alpha_{p1}L_1}\right)\right) dz.$$

In addition to notations introduced in section 2.2 and used through out this chapter in these formulas we use F which denotes the EDFA noise figure. The parameters of transport and dispersion compensation fibres are conventionally marked by indices "1" and "2".

As discussed previously in this section, the average power model is very useful as a first step in our analysis, since it allows us to obtain both *NPS* and *OSNR*, and represents a good compromise between the high complexity and time consumption of the full amplitude simulation and the flexibility and speed of the purely analytical approach. However, the necessity of accounting for DRS for some combinations of the launch pump and signal powers makes it essential to use the numerical model.

In the numerical approach we consider a hybrid amplification dispersion compensation Raman-Fibre 2-EDFA module as shown in Figure 2.8, designed for a specific transmission Fibre 1 span. In particular, we examine SMF as Fibre 1 and DCF as Fibre 2. The length of SMF is 100 km, and the compensating DCF is adjusted so the total span average dispersion is zero. A backward Raman pump is set at the end of the SMF section and an EDFA with a noise figure of 4.5 dB is used for post-amplification at the end of the span. The combined gain from the two amplifiers compensates exactly for the total loss of the periodic cell. We consider 4 WDM channels equally spaced both sides of 1550 nm, each of them with an optical signal bandwidth of 100 GHz. The system scheme is presented in Figure 2.8.

Figure 2.9 compares the theory and the numerical results obtained from the solution of the system of coupled differential equations for the pump, signal and noise power evolution, taking into account DRS and pump depletion (2.43). In particular, the plot shows the variations of *NPS* versus the gain ratio η for a fixed *OSNR*.

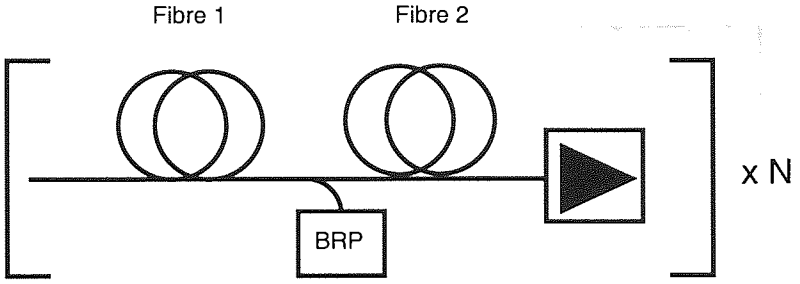

Figure 2.8: Optical link configuration with hybrid amplification.

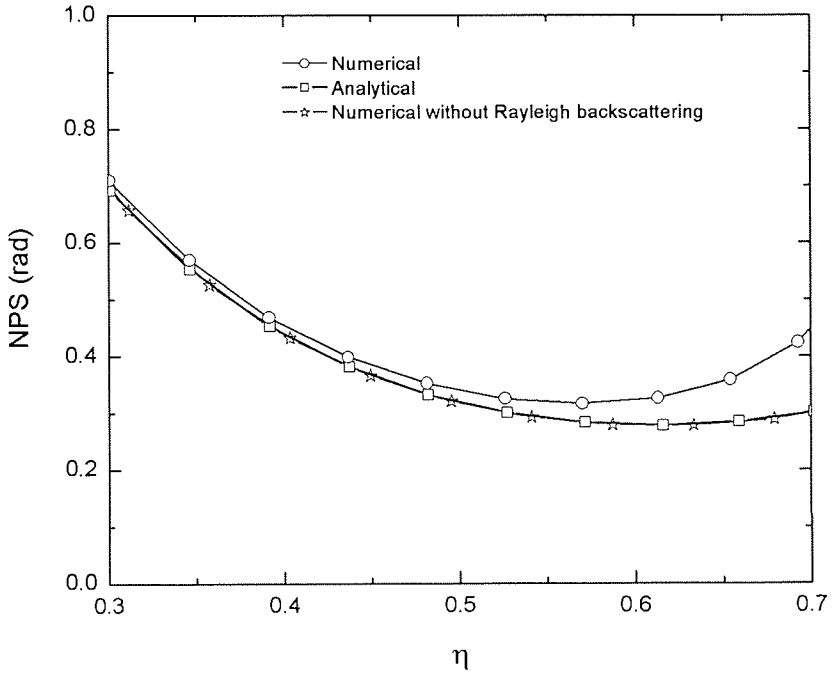

Figure 2.9: NPS with respect to η for $OSNR = 35dB$. Comparison between analytical estimate and numerical modelling with and without DRS.

A third line shows the numerical result obtained when DRS is neglected, so it can be seen that this effect is the one responsible for the deviation (at η close to one) of the analytical results from numerical ones. In order to accurately estimate the configuration that minimises the NPS under a fixed OSNR we must therefore follow the numerical route, although the analytical solution can be used to provide a very useful first estimation. It is seen from Figure 2.9 that it is possible to determine the optimal gain ratio η minimising NPS under a fixed OSNR. This way we end up with a collection of points in the (input signal, η) plane that define the optimal gain ratio for any input signal.

Figure 2.10 shows the superposition of the contour plots of OSNR and NPS in

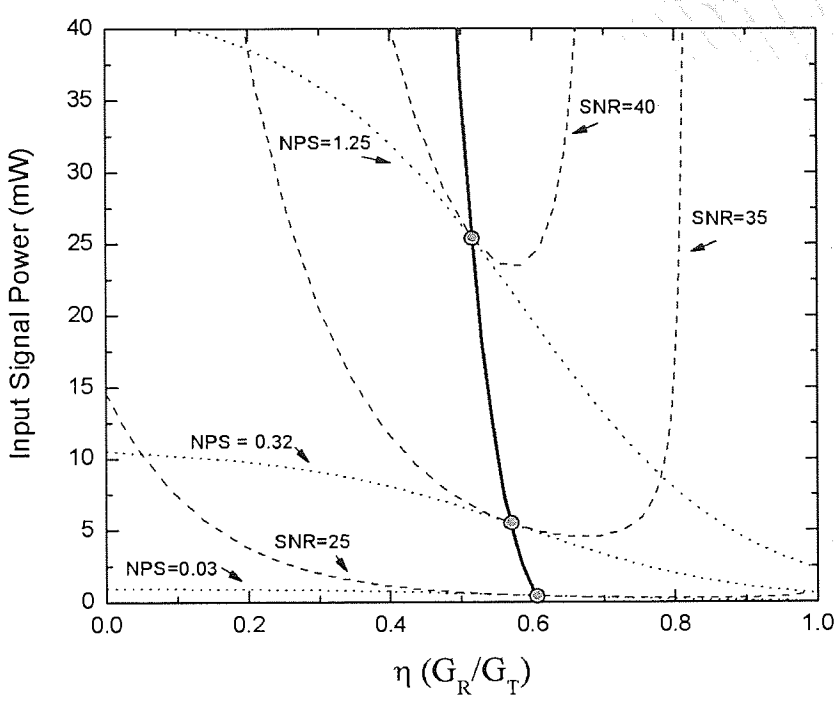

Figure 2.10: Superimposed contour plot of the OSNR and NPS with respect to the input signal power and optimisation parameter η.

the (input signal,η) plane. The points of tangency of the curves of fixed NPS and the curves of fixed OSNR represent the regimes that minimise NPS under a fixed OSNR, and thus optimise the system performance. The curve that follows these points gives the dependency of the optimal signal power for each ratio η (or vice versa, gives the optimal gain ratio that will provide the best performance for a input power). The variability of the ideal gain ratio is small, ranging from slightly below 0.5 to slightly above 0.6.

In order to confirm the results, obtained using the average-power model, and to find out the specific input power that will give the optimal performance for a particular case, the amplitude equations have been solved and the maximum propagation distance optimised in terms of η and input peak power have been determined. Figure 2.11 shows the results obtained for the 40 Gb/s channel bit rate signal. The optimal pump split for this case corresponds to $\eta = 0.55$, with an optimal input peak power of 3 dBm, which is in good agreement with the results obtained from average study. The maximum propagation distance obtained is 1323.6 km. It is important to note that an incorrect choice of η is likely to have a visible impact on system per-

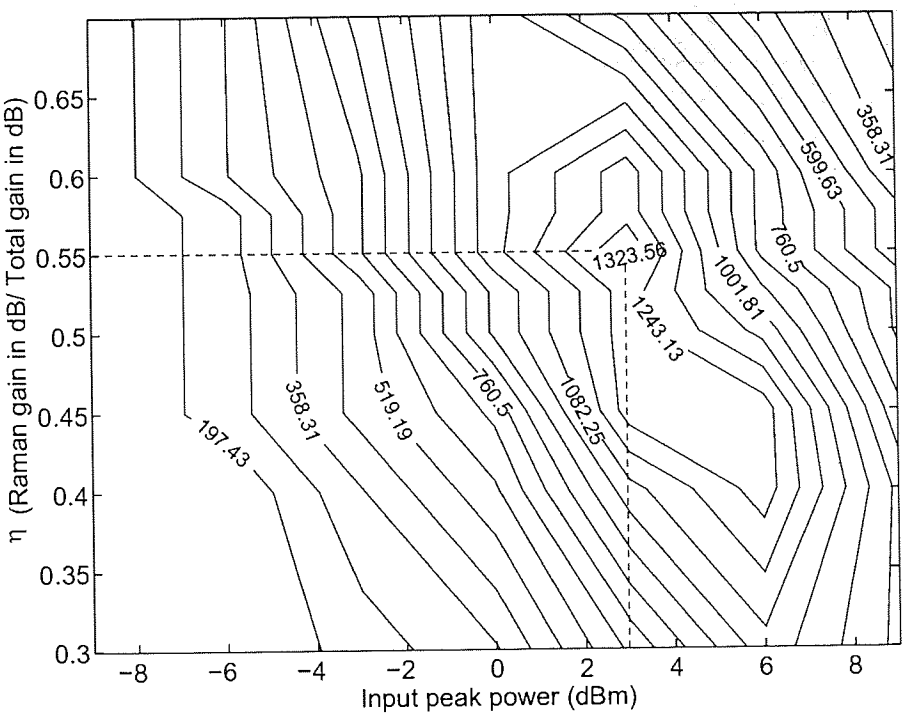

Figure 2.11: Maximum transmission distance versus input signal power and η. The results of full numerical modelling.

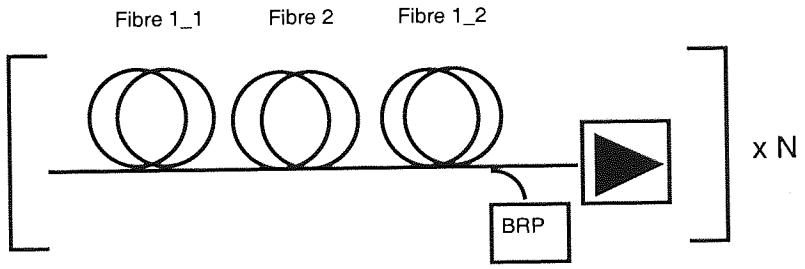

Figure 2.12: Optical fibre link with hybrid amplification. Configuration 2. Schematic setup.

formance, and that both pure Raman and pure EDFA amplifications present a much worser performance than the optimised hybrid amplification scheme.

As another example of a hybrid amplification scheme, we focus now on a configuration with the gain provided by a backward Raman pump and EDFA, both placed at the end of the transmission line, as shown on Figure 2.12. The two parameters to be optimised in this system are the ratio between Raman gain and total gain in the span (η_1) and the ratio of the first piece of transport Fibre 1 to the total length of Fibre 1 (η_2).

In numerical optimisation we use SLA as a Fibre 1 and IDF as a Fibre 2. The

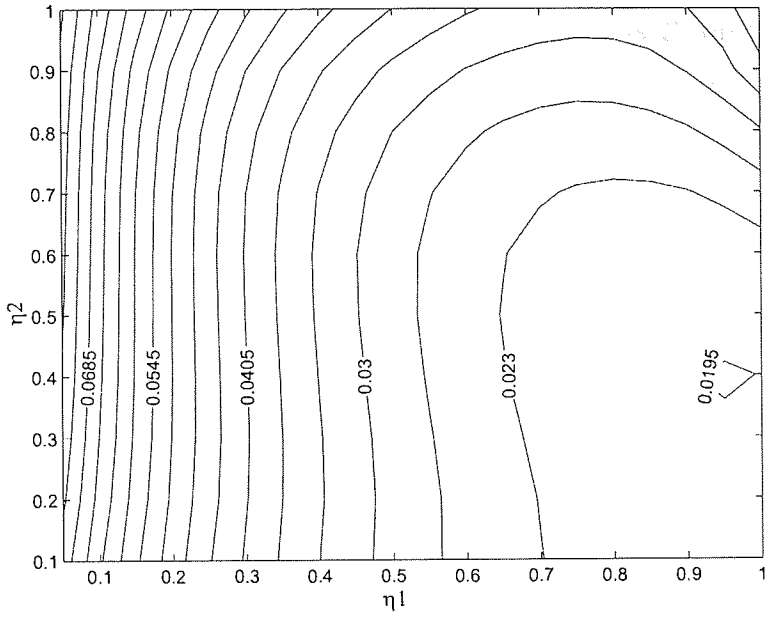

Figure 2.13: *NPS* plotted as a function of optimisation parameters η_1 and η_2 for a fixed *OSNR* of 30 dB.

parameters of these fibres are given by Table A.1 in Appendix A. The total length of SLA in simulations comprised of 100 km, and the compensating IDF was selected so the total span average dispersion became zero. As such, we launch an RZ four channel WDM signal centred at 1550 nm with the total bandwidth of 400 Hz. The Raman pump launched at 1455 nm was adjusted to compensate for the signal loss in the span. The EDFAs noise figure was 4.5 dB.

Figure 2.13 shows the *NPS* for a fixed *OSNR* of 30 dB in a contour plot versus both optimisation parameters. We can see that for the current system the optimal fibre split corresponds to a 40% of the total length of SLA in the first section, with an optimal gain ratio between distributed Raman amplification and total gain in the span close to one, corresponding to full Raman amplification. This optimal configuration is virtually independent from the chosen fixed *OSNR*, and as such it can be considered constant for a reasonable range of input signal powers.

In summary, this section considers design optimisation in optical links with hybrid amplification, as presented on Figures 2.8 and 2.12. High accuracy of the analytical approach is demonstrated for situations where the DRS effect is negligible.

In the general case, however, the necessity of the numerical optimisation is shown. The optimal gain split between amplifiers that maximises OSNR under a fixed NPS for any given input signal power is determined for the configuration of Figure 2.8. Moreover, such the gain split and the location for the DCF become optimised for the configuration of Figure 2.12.

2.7 Optimal span length

During the late nineties, EDFAs had a deep impact on the performance and design of optical networks, resulting in the deployment of a large number of high-capacity long-distance optical transmission systems. In this context, a way to finely control the ASE noise generated by the cascade of EDFA implemented in these systems consists in well-optimising the amplifier spacing. In fact, the optimal amplification span length is the one which enables the best trade-off between the low cost requirements (a low number of amplifiers, ensuring a satisfying cost efficiency) and the high system performance constraints (a large number of amplifiers, ensuring a good performance of the transmission system, thanks to the reduction of ASE noise accumulation). Nonlinear effects also have a strong influence on the overall system performance. In particular, long amplifier spans result in high input average powers (the aim being to maintain a good optical signal to noise ratio), leading in turn to an increase on the impact of nonlinearities. In these conditions, the goal of transmission system designers is to find the best balance between the requirements of a high *OSNR* and low nonlinear impairments. Yariv demonstrated in [58] that the highest OSNR of an ideal optically amplified system is obtained for a transmission system implementing a perfectly distributed amplification or asymptotically vanishing span length. This last result is incompatible with a modern necessity for cheaper system design. Fortunately, the recent availability of high pump lasers has made possible the comeback of Raman amplification in WDM transmission systems. Improved *OSNR* performance suggested by Raman amplification makes it genuinely attractive for deployment in optical communications. Moreover, combined with dispersion management and EDFA amplification, DRA can be used to better control

the signal power evolution inside the amplification spans and thus nonlinear effects along the optical line.

In this section, we highlight new design possibilities in high-speed optical communications and present some examples of transmission systems in which optimal performances do not necessarily require shorter amplifier spacing. As shown below, the implementation of both DRA and proper nonlinearity managements permits to significantly increase the amplifier span length without degrading the output *OSNR* or exacerbating nonlinearities. By using the optimisation approach developed in section 2.1, we investigate the amplifier span length impact on the optimal configuration of the amplification scheme in 40 Gb/s WDM transmission systems based on hybrid Raman/EDFA amplification and SMF/DCF and SLA/IDF dispersion mapping. The optimal system configuration is then determined by performing a conditional minimisation of the *NPS* under a fixed *OSNR*, or vice versa, a maximisation of the *OSNR* under a fixed *NPS*.

More specifically, we perform numerical modelling of 40 Gb/s WDM transmission systems based on a hybrid Raman/EDFA amplification and various dispersion maps, using the average power equations for the Raman pump, signal and noise, (2.43) in order to find the optimal system parameters (the optimal gain split between the lumped and distributed amplifiers and the best amplifier spacing) that allow for the minimisation of the *NPS* under a fixed *OSNR*. The numerical approach ensures that all important effects, including DRS noise and pump depletion, are accounted for.

The focus is set on two basic configurations, depicted in the Figure 2.14 and Figure 2.15. In both cases, a two-step dispersion map with hybrid Raman/EDFA amplification is considered, but the position of the backward Raman pump differs in each configuration. In configuration a), the backward Raman pump is placed immediately after the section of positive dispersion fibre (Fibre 1) and an EDFA, with a typical noise figure of 4.5 dB, is used for post-amplification at the end of the span. In configuration b), both the backward Raman pump and the EDFA are located together at the end of the periodic transmission cell. The combined distributed/lumped gain compensates exactly for the total attenuation due to the transmission through the

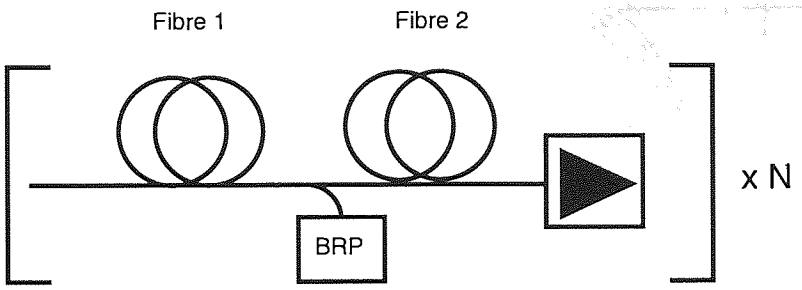

Figure 2.14: Configuration a. Schematic setup.

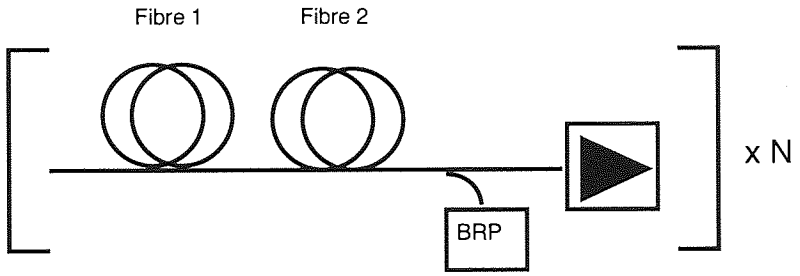

Figure 2.15: Configuration b. Schematic setup.

two fibre sections.

In the presented analysis we actually optimise two parameters, the total span length and the gain split ratio η, defined as the quotient between the on-off gain provided by the distributed Raman amplification and the total gain, both in dB.

We consider WDM transmission at 40 Gb/s with equally spaced channels (the channel spacing is equal to 100 GHz) and symmetrically distributed from the both sides of 1550-nm wavelength. Two different dispersion maps are investigated for configuration a): one based on SMF with DCF, and another one based on SLA with IDF. For configuration b), only the SLA/IDF option is considered. The features of the fibres used are summarised in the Table A.1 of Appendix A. The length of both positive and negative dispersion fibres within the span are considered as variable parameters, but the length of the negative dispersion fibre is automatically adjusted to compensate exactly for the accumulated dispersion of the positive dispersion fibre, at the end of each periodic cell. The total transmission distance is fixed to 900 km of SMF for the first fibre pair, and 900 km of SLA+IDF, for the second one. The number of spans (which is chosen in each case so the number of spans is always an integer) varies with the cell length, in order to keep the total transmission distance.

Figures 2.16 and 2.17 display *NPS* in a contour plot versus the length L of the

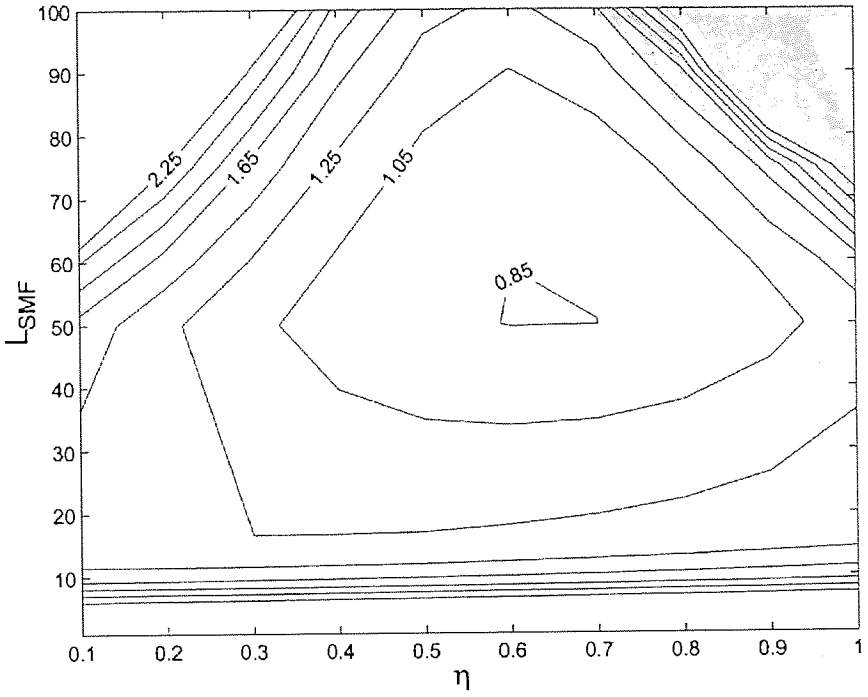

Figure 2.16: Contour plot of *NPS* versus η and the total span length for $OSNR = 22$ dB after 900 km through SMF/DCF (Configuration a).

span and the gain ratio η, for a fixed output *OSNR* of 22 dB in configuration a), for both fibre pairs. We can observe that there is a clear optimal length for the amplification span (for which the NPS is minimal), which is about 50 km (of SMF) for the SMF/DCF case, and about 90 km (60 km of SLA) for the SLA/IDF scheme. This optimal cell length can be understood as the one that allows us to find the best balance between the short span and long span regimes, both suffering enlarged nonlinear effects. In the short span regime, in which the signal is transmitted in quasi-lossless conditions, the system performance become degraded by high nonlinearities accumulated from even relatively low input powers injected into the spans (because of the quasi-flatness of the power span profile). In the long span regime the long distance between amplifiers helps reducing NPS, but leads to an increase of ASE noise, inducing in turn a rise of the span input signal power to keep output OSNR constant, and a nonlinearity exacerbation.

It can also be derived from Figures 2.16 and 2.17 that the optimal η varies slightly with the span length (when longer than 20-30 km for the two basic maps considered here), becoming a little bit lower for long amplification spans. This phenomenon

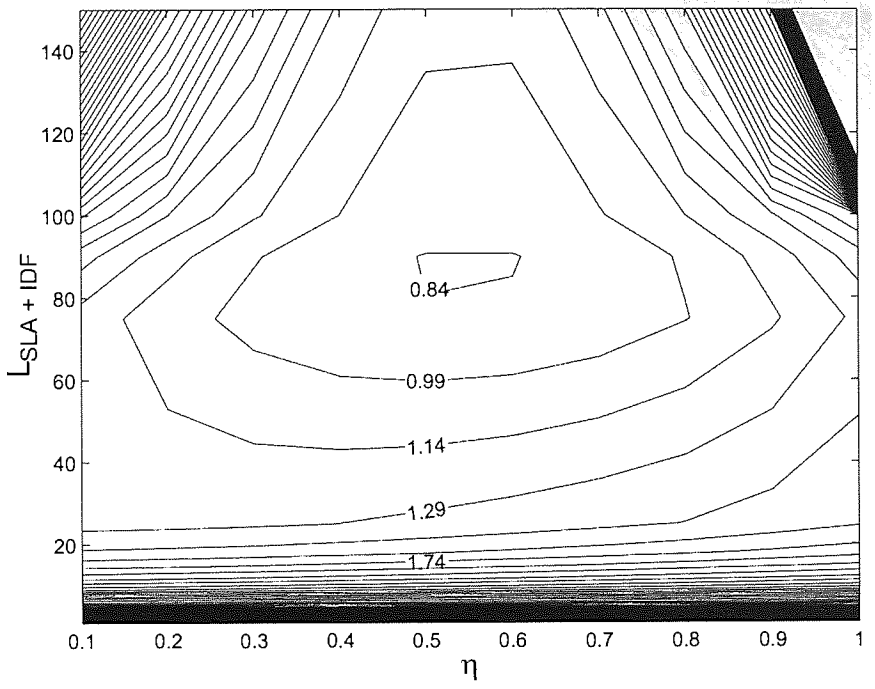

Figure 2.17: Contour plot of *NPS* versus η and the total span length for $OSNR = 22$ dB after 900 km through SLA/IDF. (Configuration a).

can be explained by the growth of the Raman pump power and gain, and with it, of the contribution of DRS noise (due to a worse distribution of the gain within the span) when the span length increases. In order to recover the best possible performance, then, a reduction of the Raman gain and an increase on the contribution of the lumped amplifier is required. For span lengths shorter than 20-30 km, there is no clear optimal η for the two cases considered here. On the other hand, for the case of 100 km and higher of SMF or SLA+IDF, the determination of the optimal η becomes crucial, as shown on Figures 2.16 and 2.17.

A slightly different behaviour can be observed if the output *OSNR* is increased, as shown on Figure 2.18 for the case of SLA/IDF fibre pair. The higher input signal powers required in this case, together with necessity for higher pump powers in order to obtain the same gain, increase the effect of DRS, so the optimal η in general is lower in this occasion. As seen from Figures 2.17 and 2.18, in our case the optimal η changes from the 0.55 for the 22 dB case to 0.5 for the 30 dB case. The optimal cell length, on the other hand, remains unchanged at about 90 km.

Finally, Figure 2.19 shows the results obtained for configuration b): SLA/IDF

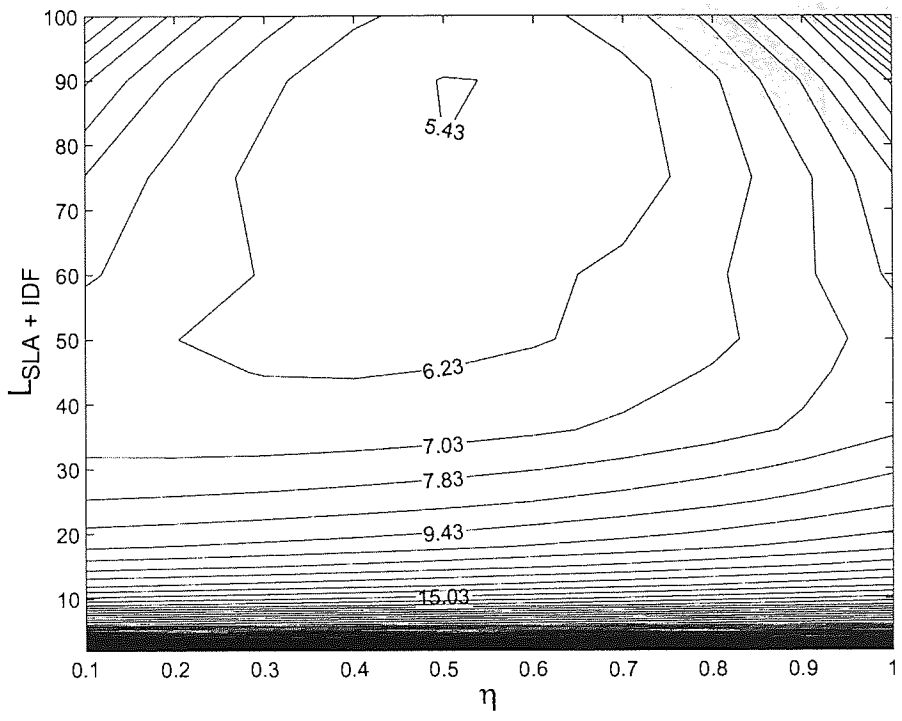

Figure 2.18: Contour plot of *NPS* versus η and the total span length for $OSNR = 30$ dB after 900 km through SLA/IDF. (Configuration a).

dispersion map used with both the discrete amplifier and the Raman pump located at the end of the transmission cell. The change of configuration has a clear effect on the optimal span length, which is reduced to about 50 km of combined SLA+IDF, when compared to the configuration a), for which the optimum was about 90 km. For a low fixed output OSNR, the optimal amplifier configuration corresponds to values of η close to 1 (corresponding to full Raman amplification), but when OSNR or span length are increased, the optimal η is reduced to counteract the effect of DRS noise (the optimal configuration requires then a higher participation from the EDFA to limit its impact). As it happened with configuration a), the increase on the output OSNR to 30 dB has a negligible impact on the optimal span length.

It is interesting to note that for similar span lengths and the same SLA/IDF fibre base, configuration b) suffers from lower nonlinear impairments than configuration a) at equivalent noise levels. It seems, then, that the possibility of using distributed amplification for the whole span (thanks to the position of the Raman pump at the end) while at the same time being able to limit the effect of DRS by increasing the

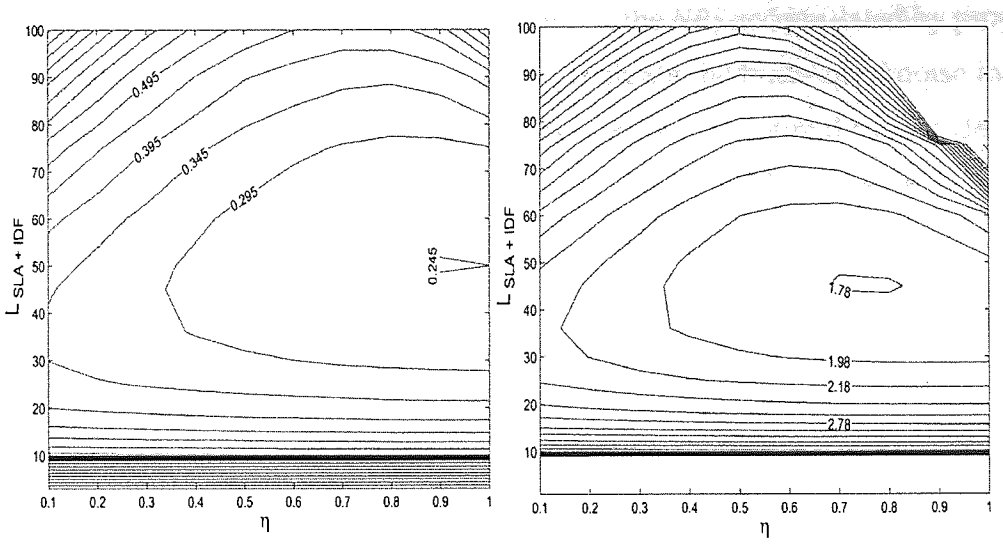

Figure 2.19: *NPS* versus η and the total span length for a fixed *OSNR* of 22 dB (left) and 30 dB (right) after 900 km of the total transmission through SLA/IDF. (Configuration b).

contribution of the lumped amplifier when higher gains are required, gives configuration b) a higher flexibility. This does indeed not have to be the case for other fibre combinations, but the low attenuation and relatively high effective core area of IDF make it possible in this case to pump the negative dispersion fibre directly without too much exacerbation of DRS noise.

In conclusion, in this section we show, using nonlinearity management considerations, that the optimal performance in high bit-rate dispersion-managed fibre systems with hybrid amplification is achieved for a certain amplifier spacing - which is different from the commonly known optimal noise performance corresponding to fully distributed amplification. Moreover, for particular dispersion maps using different fibre pairs we have determined the optimal span length and the Raman/EDFA gain split. The optimisation results are nearly independent on the desired output *OSNR*, hence the optimal span length determined for each system through this method is applicable to a wide range of cases.

2.8 Conclusions

In this chapter we have introduced a novel design optimisation technique based on a balance between the noise and nonlinear impairments. Assuming nonlinearity to

be a detrimental factor, we measure its impact by the *NPS* accumulated by propagating signals. The *OSNR*, moreover, is used to evaluate the built-up of noise induced by optical amplifiers. In our approach we determine the optimal system design by maximising the output *OSNR* under a constraint of fixed *NPS* (or vice versa minimising the *NPS* while keeping the *OSNR* fixed).

In section 2.2 we provide the analytical expressions for the *OSNR* and *NPS* obtained under the assumptions of undepleted pump and neglecting the effect of DRS. Although in specific cases of optical transmission systems with low DRS these expressions demonstrate a very high accuracy, in general design optimisation require numerical approaching. As such, the overview of methods that can be deployed in numerical optimisation is presented in section 2.3.

In section 2.4 we illustrated the suggested technique by optimising the design of a three-step dispersion map with distributed backward Raman amplification. In particular, we examined the optimal location of the dispersion compensating module within the periodic section of an SMF/DCF line. The found configurations provide simultaneous reduction of nonlinear and noise impairments. For the particular transmission distance considered (1000 km of SMF) such optimal split of SMF is in the range of (10-25%SMF)+DCF+(90%-75%SMF). This results show an excellent agreement with the ones found by solving the nonlinear Schrödinger equation.

In section 2.5 we accomplished design optimisation for an optical transmission link with bidirectional Raman amplification. This optimisation was carried out using the analytical solution obtained under an assumption of undepleted pumps and without inclusion of DRS, and by means a full numerical approach accounting for all important effects. Both procedures lead to the same final solution in the considered example. In particular, we found that in considered case the 50% gain split between the forward and backward propagating pumps and 70%SMF+DCF+30%SMF dispersion map present the optimum performance.

In section 2.6 the optimisation technique was applied to evaluation of optimal parameters in optical transmission with hybrid Raman/EDFA amplification. The optimal gain split between amplifiers that maximises OSNR under a fixed NPS for any given input signal power is determined in the first examined configuration with

fixed dispersion map. Subsequently, we optimised the gain split and optimal location of DCF in the second considered configuration.

Finally, in section 2.7 we demonstrated the existence of a non-trivial optimal amplifier spacing, matching modern requirements of cheap system design, for 40 Gb/s WDM dispersion-managed transmission systems using hybrid Raman/EDFA amplification scheme. Using the general approach of section 2.1, based on the concepts of noise and nonlinearity management, we have shown the existence of this optimal amplifier spacing in the particular case of 40 Gb/s WDM transmission systems, considering various dispersion maps (using different fibres arrangements) and hybrid Raman/EDFA amplification schemes. The optimisation results are nearly independent of the desired output OSNR, hence the optimal span length determined for each system through this method is applicable to a wide range of cases.

Chapter 3

Statistical analysis of amplification noise

3.1 Introduction

Due to high requirements imposed on quality in modern optical signal transmission it often becomes impractical to measure bit error rates (BER) directly. Otherwise, the problem of computing the BERs can be addressed statistically. More specifically, BER calculations can be performed based on the probability density functions (PDFs) of the received "marks" and "spaces". In the standard Q factor approach Gaussian assumption is made regarding the signal statistics and the BER is calculated from the binary digits' expectation values and variances. However, in transmission systems deploying devices with essentially nonlinear transfer function (e.g. 2R optical regenerator) signal distributions no longer have Gaussian form and this approach can not be relied upon. Therefore, effective theoretical and numerical approaches for estimating the non-gaussian signal statistics are highly desired. To evaluate the actual marks/spaces distributions in [59] it was proposed to consider a discrete set of signal intensity levels and to define transfer probability matrices. This approach is referred to as covariance matrix method. The more accurate, but more time consuming approach to calculation of signal statistics is based on Monte Carlo simulations. To accelerate numerical simulations in modern transmission systems with reasonably low BER some additional techniques have to be implemented. In [60] it was proposed to extrapolate the tails of the signal distributions, while the tops were found using conventional Monte Carlo approach. Alternatively, the ad-

vanced multicanonical Monte Carlo (MMC) technique [61–63] can be effectively applied to computing of the far tails of the probability density functions (PDFs).

3.2 Multicanonical Monte Carlo

In this subsection a short description to the MMC approach is given. In particular, we demonstrate how the method can be applied to evaluating a PDF of a control quantity $V(\mathbf{x})$, where $\mathbf{x}$ represents a random vector sampled from a multidimensional state space Γ with the distribution $\rho(\mathbf{x})$.

First, we partition the sampling space Γ into M subspaces Γ_k where $1 \leq k \leq M$, such that

$$\Gamma_k = \{\mathbf{x} \in \Gamma \,|\, (k-1)\Delta V \leq V(\mathbf{x}) \leq k\Delta V\} \tag{3.1}$$

Put simply, Γ_k represent sets of samples $\mathbf{x}$ such that $V(\mathbf{x})$ falls in the k-th bin H_k of the histogram H, a set defined as $\{V \,|\, (k-1)\Delta V \leq V(\mathbf{x}) \leq k\Delta V\}$. Then, the probability P_k of a random realization $\mathbf{x}$ to be sampled from a subspace Γ_k becomes

$$P_k = \int_{\Gamma_k} \rho(\mathbf{x})\, d\mathbf{x} = \int_{\Gamma} \chi_k(\mathbf{x})\, \rho(\mathbf{x})\, d\mathbf{x}, \tag{3.2}$$

where $\chi_k(\mathbf{x})$ is defined as

$$\chi_k(\mathbf{x}) = \begin{cases} 1, & \mathbf{x} \in \Gamma_k \\ 0, & \textit{otherwise}. \end{cases}$$

Using the conventional Monte Carlo simulations, this probability can be approximated as

$$P_k \approx \frac{1}{N} \sum_{i=1}^{N} \chi_k(\mathbf{x}^i), \tag{3.3}$$

where $\mathbf{x}^i$ are N realizations of the random variable $\mathbf{x}$ sampled according to the probability density $\rho(\mathbf{x})$. A sufficient improvement to estimate (3.3) become possible through deployment of a biased PDF $\rho^*(\mathbf{x})$ for the vector $\mathbf{x}$. Indeed, by a proper selection of the distribution $\rho^*(\mathbf{x})$ it is possible to reduce the variance of P_k in (3.3). This principle is realized in a variety of importance sampling methods and, in particular, in MMC.

Expression (3.2) can be formally rewritten as

$$P_k = \int_\Gamma \chi_k(\mathbf{x}) \frac{\rho(\mathbf{x})}{\rho^*(\mathbf{x})} \rho^*(\mathbf{x})\, d\mathbf{x}. \tag{3.4}$$

Applying the conventional Monte Carlo to this expression, it is possible to obtain the following approximation

$$P_k \approx \frac{1}{N} \sum_{i=1}^{N} \chi_k(\hat{\mathbf{x}}^i) \frac{\rho(\hat{\mathbf{x}}^i)}{\rho^*(\hat{\mathbf{x}}^i)}, \tag{3.5}$$

where $\hat{\mathbf{x}}^i$ are sampled from a biased distribution $\rho^*(\mathbf{x})$. Zero variance of estimate (3.5) is attained for the optimal biased PDF

$$\rho_{opt}(\mathbf{x}) = \chi_k(\mathbf{x}) \frac{\rho(\mathbf{x})}{P_k}. \tag{3.6}$$

However, according to expression (3.6), the optimal PDF is dependent on the unknown probabilities P_k. The MMC approach takes over this issue by implementing an iterative procedure over the biased PDF $\rho(\mathbf{x})$, so that with growth in a number of iterations it converges to $\rho_{opt}(\mathbf{x})$. Based on expression (3.6), we define the PDF $\rho^{*,j}(\mathbf{x})$ for the j-th iteration as

$$\rho^{*,j}(\mathbf{x}) = \frac{\rho(\mathbf{x})}{c^j P_k^j}, \ \mathbf{x} \in \Gamma_k \tag{3.7}$$

where P_k^j represent the approximate probabilities P_k found at the previous iteration and c^j is a normalisation constant, ensuring that

$$\int_\Gamma \rho^{*,j}(\mathbf{x})\, dx = 1. \tag{3.8}$$

Moreover, it is customary to use $\rho(\mathbf{x})$, as an initial guess for the $\rho^*(\mathbf{x})$, hence, setting $P_1^1 = \cdots = P_M^1 = \frac{1}{M}$. In fact, the choice of the initial sampling PDF does not substantially affect the performance of the MMC and other options can be equally efficient in terms of convergence [62]. After each iteration the P_k^j undergo updating using the information provided by the latest and the previous histograms. The distribution bias, moreover, becomes selected in such a manner that the number of occurrences of rare events in sampling experiments is artificially increased, compared to the unbiased distribution. Eventually, the algorithm approaches a state when the expected number of entries to each bin of the histogram H becomes equal

to $\sum_{i=1}^{N} \chi_k(\mathbf{x}_i) = N/M$. Substituting this value in (3.7) and (3.5) yields $c^j \to M$ and $P_k^j \to P_k$. The recursive relations for updating P_k^j were suggested in [61]:

$$\begin{aligned} P_{k+1}^{j+1} &= \frac{P_k^{j+1} P_{k+1}^j}{P_k^j} \left(\frac{\hat{H}_{k+1}^j}{\hat{H}_k^j} \right)^{\hat{g}_k^j}, \\ \hat{g}_k^j &= \frac{g_k^j}{\sum_{l=1}^{j} g_k^l}, \\ g_k^l &= \frac{\hat{H}_k^l \hat{H}_{k+1}^l}{\hat{H}_k^l + \hat{H}_{k+1}^l}, \end{aligned} \tag{3.9}$$

where in addition we define $\hat{g}_k^j = 0$ if $g_k^j = 0$ and $g_k^l = 0$ if $\hat{H}_k^l + \hat{H}_{k+1}^l = 0$. Moreover, before applying these relations to recalculating the probabilities P_k^{j+1} we set P_1^{j+1} to an arbitrary positive number. The exact value of the number is not important since afterwards we renormalise the approximate probabilities P_k^{j+1} so that

$$\sum_{k=1}^{M} P_k^{j+1} = 1. \tag{3.10}$$

In each iteration we accomplish sampling from the distribution $\rho^{*,j}(\mathbf{x})$ using the Metropolis algorithm [64]. This approach relies on the concept of Markov chains. More specifically, in numerical simulations we produce a random walk of samples $\hat{\mathbf{x}}^i$. Each transition goes from $\hat{\mathbf{x}}^i = \mathbf{x}_a \in \Gamma_k$ to $\mathbf{x}_b = \mathbf{x}_a + \varepsilon^j \Delta\mathbf{x}$ where ε^j is a random step, that does not favour any direction in Γ. With the probability π_{ab} the transition becomes accepted and $\hat{\mathbf{x}}^{i+1} = \mathbf{x}_b$,

In problems related to optics communications the state Γ represents a set of all possible noise realizations at all amplifiers and all frequencies. The $\rho(\mathbf{x})$, therefore, is the product of gaussian PDFs of all noise components, which are assumed to be identical independent Gaussian random variables:

$$\rho(\mathbf{x}) = \prod_{l=1}^{d} \rho_l(x_l), \tag{3.11}$$

where d is the dimension of Γ and $\rho_l(x_l)$ are one dimensional Gaussian distributions. Similarly to the approach of [62], in our simulations we choose to consider the perturbation of each noise component $x_{a,l}$ of $\mathbf{x}_a$ separately, accepting or rejecting it with the probability π_{ab}^l, defined as

$$\pi_{ab}^l = \min\left(\frac{\rho_l(x_{b,l})}{\rho_l(x_{a,l})}, 1 \right). \tag{3.12}$$

For each noise component we select a perturbation step ε_l^j from the symmetric uniform distribution defined on the interval $[-\alpha, \alpha]$. The step size α in each iteration was adjusted so that the acceptance ratio was close to a number set a-priory, with the typical value of 0.5. Following the algorithm, we obtain a trial set $\mathbf{x}_b$ in which only some of the components are different from their previous values in $\mathbf{x}_a$. Subsequently we calculate $V(\mathbf{x}_b)$ and determine which bin k_b in the histogram H the sample $\mathbf{x}_b$ goes to, we finally accept this step with the probability

$$\min\left(P_{k_a}^j / P_{k_b}^j, 1\right). \tag{3.13}$$

The compound transition probability, therefore, reads

$$\pi_{ab} = \left\{\prod_{l=1}^{d} \min\left(\frac{\rho_l(\hat{\mathbf{x}}_{b,l})}{\rho_l(\hat{\mathbf{x}}_{a,l})}, 1\right)\right\} \min\left(P_{k_a}^j / P_{k_b}^j, 1\right). \tag{3.14}$$

All noise realisations accepted in iteration j, subsequently, become recorded in a histogram H^j, containing information about the number of occurrences of $\mathbf{x}$ in Γ_k:

$$H_k^j = \sum_{i=1}^{N} \chi_k(\mathbf{x}_i). \tag{3.15}$$

At the end of each iteration, i.e. after N distinct steps in random walk, the probabilities P_k^j become updated with the aid of expressions (3.9). We consider the method to have converged, when the difference between PDFs from the last two iterations becomes hardly visible on a log scale.

In order to implement this approach we developed a comprehensive C++ software. The general structure of our code and the principal relations between the main objects are described in Appendix B. Prior to each iteration, we apply the relaxation method discussed in section 2.3 to adjust the step size α.

3.3 Analysis of soliton statistics

The accurate calculation of BER remains one of the most important and challenging theoretical problems in optical fibre communications. Until recently, the consideration of statistical properties in optical systems, typically, was limited to the assumption of Gaussian statistics. This often can be justified for the central part of

the distribution function, but not for the tails of the PDF. However, since the tails are responsible for the probability of very rare events, they can be important, for instance, in the situations when an error occurs due to the arrival of a carrier pulse (corresponding to elementary "one") outside the detection window (timing jitter). Such rare events described by the tails of the probability distribution, can be of importance for modern fibre links operating at very low bit-error-rates. Optical soliton models, even those with limited direct applications in complex modern optical links, play an important role in a careful mathematical analysis of many significant characteristics of fibre-optic systems. A variety of powerful mathematical methods can be applied for the analysis of the carrier pulse properties in a soliton transmission line. Finding the statistics of an optical soliton in the presence of optical amplifier noise is a classical problem both for a fibre communication and the nonlinear science. Please note that in soliton-based signal transmission the nonlinearity plays a positive role, thus invalidating the use of the analysis of Chapter 2.

One of the major limitations imposed on the propagation distance in long-haul optical fiber transmission lines is the ASE noise which introduces jitter into the soliton transmission system and thus deteriorates the quality of the transmission. In their pioneering work Gordon and Haus [11] were first to study the timing jitter in the soliton transmission and derived a celebrated result that the timing fluctuations along the transmission line grow as a cube of propagation distance. However the vast majority of the results have been obtained assuming (sometimes implicitly) that the underlying statistics of soliton parameters is Gaussian. The first results on the non-Gaussian soliton statistics have only appeared recently. In paper [65] the above statistics were studied by means of functional integration technique. This method allowed to obtain a series of asymptotics for the tails of probability density functions (PDF) which turned out to be essentially non-Gaussian. Moreover, a considerable progress was made recently with a Fokker-Planck equation approach. In [66] there was derived a Fokker-Planck equation, which contains exact and complete knowledge of the evolution of the soliton statistics, and solving this equation analytically or numerically provides one with a complete or marginal PDF for soliton parameters. In this section we apply the MMC simulation technique to modelling

the Fokker-Planck equation and show numerically computed marginal PDFs for the amplitude, phase, frequency and timing jitter in soliton pulses.

The perturbed nonlinear Schrödinger equation in soliton units has the following form [67]:

$$\frac{\partial q}{\partial z} = \frac{i}{2}\frac{\partial^2 q}{\partial \tau^2} + i|q|^2 q + n(\tau, z), \tag{3.16}$$

where q is an envelope of the electric field, τ and z represent the time and propagation distance respectively and n is the added white Gaussian noise term, modelling ASE with the following statistics

$$< n(\tau, z) > = < n(\tau, z) n(\tau', z') >= 0, \tag{3.17}$$

$$< n(\tau, z) n^*(\tau', z') > = D\delta(z - z')\delta(\tau - \tau'). \tag{3.18}$$

Using the standard single soliton anzatz:

$$q_0(\tau, z) = A(z)\mathrm{sech}\{A(z)[\tau - T(z)]\}\exp[-i\Omega(z)\tau + i\phi(z)] \tag{3.19}$$

and adiabatic soliton perturbation theory [67] for small noise intensities D one can come up with the Fokker-Planck equation [66] for the joint distribution function $P(A, \phi, \Omega, T|z)$

$$\begin{aligned}\frac{\partial P}{\partial z} = & -\frac{1}{2}(A^2 - \Omega^2)\frac{\partial P}{\partial \phi} + \Omega\frac{\partial P}{\partial T} + D\left\{\frac{1}{6}AT^2 + \frac{1}{12A}\left(2 + \frac{\pi^2}{6}\right)\right\}\frac{\partial^2 P}{\partial \phi^2} + \\ & \frac{D}{3}AT\frac{\partial^2 P}{\partial \phi \partial \Omega} + \frac{D}{2}A\frac{\partial^2 P}{\partial A^2} + \frac{D}{6}A\frac{\partial^2 P}{\partial \Omega^2} + \frac{D\pi^2}{24A^3}\frac{\partial^2 P}{\partial T^2}.\end{aligned} \tag{3.20}$$

The initial condition for (3.20) can be set as

$$P(A, \phi, \Omega, T|0) = \delta(A - A_0)\delta(\phi)\delta(\Omega)\delta(T). \tag{3.21}$$

The Stratonovich approach was used to derive equation (3.20).

Although in the limit of small distance z the Gaussian shape can be obtained from (3.20) for the heads of the marginal distribution functions, the tails of the PDFs are non-gaussian even for arbitrary small propagation distances [66]. For example, the amplitude jitters $P(A)$ demonstrate the exponential asymptotic in the tails, as shown in [66]. The PDF for the amplitude jitter, derived by solving the Fokker-Planck equation in (3.20), yields the expression [66]:

$$P(A|z') = \frac{1}{z'}\left(\frac{A}{A_0}\right)^{1/2} \exp\left[-\frac{A+A_0}{z'}\right] I_1\left(\frac{2\sqrt{AA_0}}{z'}\right), \tag{3.22}$$

where I_1 is the modified Bessel function, $z' = (D/2)z$ and $\alpha_k = k/\sqrt{3}$.

To support this theoretical analysis and to gain more insight into the stochastic properties of soliton parameters we conducted numerical Monte Carlo simulations. As such, we approach the Fokker-Planck equation (3.20) by numerical integration of an equivalent Langevin equation system

$$\frac{\partial Q_i}{\partial z} = g_i(\mathbf{Q}, z) + \sum_{j=1}^{N} h_{ij}(\mathbf{Q}, z)\Gamma_j \tag{3.23}$$

where g_i and h_{ij} can be derived from the further introduced drift and diffusion coefficients of the Fokker-Planck equation (3.20). One way to calculate this parameters is presented in [68]. In the canonical form equation (3.20) reads

$$\frac{\partial P}{\partial z} = -\frac{\partial}{\partial Q_i}\left[D_i^{(1)}(Q)P\right] + \frac{\partial^2}{\partial Q_i \partial Q_j}\left[D_{ij}^{(2)}(Q)P\right] \tag{3.24}$$

where $D_i^{(1)}$ are the elements of the drift vector

$$D^{(1)} = \begin{bmatrix} \langle n \rangle \\ 0 \\ 0.5\left(A^2 - \Omega^2\right) \\ -\Omega \end{bmatrix} \tag{3.25}$$

and $D_{ij}^{(2)}$ are the components of the diffusion matrix

$$D^{(2)} = \begin{bmatrix} \frac{\langle n \rangle A}{2} & 0 & 0 & 0 \\ 0 & \frac{\langle n \rangle A}{6} & \frac{\langle n \rangle AT}{6} & 0 \\ 0 & \frac{\langle n \rangle AT}{6} & \langle n \rangle\left(\frac{AT^2}{6} + \frac{2+\pi^2/6}{12A}\right) & 0 \\ 0 & 0 & 0 & \frac{\langle n \rangle \pi^2}{24A^3} \end{bmatrix} \tag{3.26}$$

The terms Γ_j in equations (3.23) denote the gaussian random variables with the following correlation properties

$$\langle \Gamma_i(z) \rangle = 0, \tag{3.27}$$

$$\langle \Gamma_i(z)\Gamma_j(z') \rangle = 2\delta_{ij}\delta(z - z'). \tag{3.28}$$

and $\mathbf{Q} = [A, \Omega, \phi, T]$ is the unknown vector function.

Using the Stratonovich rule for integration, the solution to Langevin equation system (3.23) can be estimated using the following numerical scheme [68]

$$Q_{i,n+1} = Q_{i,n} + D_i^{(1)}(\mathbf{Q_n}, z_n)\,\Delta z + d_{i,j}(\mathbf{Q_n}, z_n)\sqrt{\Delta z} w_{jn}, \tag{3.29}$$

where $Q_{i,n}$ represents the approximate solution at distance $z_n = n\Delta z$, Δz is the step size, $D_i^{(1)}$ is the drift vector given by relation (3.25), $d_{i,j}$ denotes the square root of the diffusion matrix (3.26) and w_{jn} in analogy with Γ is a Gaussian random variable with the following stohastic properties

$$\langle w_{in} \rangle = 0, \tag{3.30}$$

$$\langle w_{in} w_{jk} \rangle = 2\delta_{ij}\delta_{nk}. \tag{3.31}$$

We calculated marginal PDFs of soliton parameters using the MMC approach outlined in section 3.2. The favourable combination of relative simplicity of implementation, high accuracy and high efficiency of MMC suggests a particular attractiveness to this method. Moreover, by construction the MMC is less time-consuming than conventional Monte Carlo methods in determining distributions tails. In the considered example the sample state Γ was composed by values of the random variable w. In every Monte Carlo step we applied numerical scheme (3.29) to evaluate $\mathbf{Q}$ at a given distance. To keep the approach simple at a time we used only one soliton parameter as a control quantity for the MMC iterations and, therefore, used a one dimensional histogram, composed by 100 bins. We used 20,000 samples in the first MMC iteration and increased this number by 15% in each following iteration. The step size in Metropolis random walk was adjusted to fit the acceptance ratio of 0.5. The simulation convergence required up to 10 MMC iterations.

In simulations we consider a cascade of SMF fibre spans. The length of each span in this example was set to 100 km. The parameters of SMF are summarised in Appendix A. The losses acquired by signals during propagation in one span are fully compensated by EDFAs with the noise figure of 4.5 dB, set at the end of each amplification period. In such SMF-based links with periodic lumped amplification we launch a 20 ps conventional soliton pulse centred at a wavelength of 1550 nm.

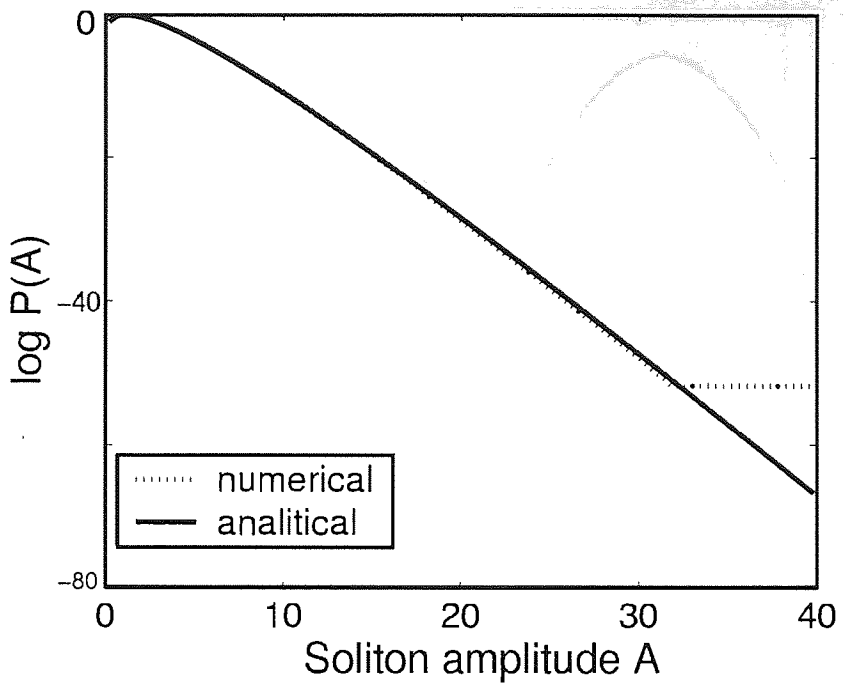

Figure 3.1: Soliton amplitude statistics.

Figure 3.1 shows a comparison between the PDF for the soliton amplitude estimated through numerical simulations and analytically derived distribution function (3.22), plotted after 100,000 km. An excellent agreement between the curves seen on the figure validates the theory of [66] in application to a typical examplanary long-haul optical transmission line. Moreover, a high accuracy in estimate of the amplitude distribution tails seen for the orders of up to -50 suggests the MMC technique a strong candidate to approach the task of calculating the distributions of the remaining soliton parameters, for which there is no a general close-form analytical expression and which then require numerical approaching. In a full agreement with [66] the PDF structure of the soliton amplitude is clearly non-gaussian at such a large propagation distance. The figure, moreover, clearly shows exponential tails of the amplitude PDF, as predicted in [66].

Figure 3.2 shows the marginal distribution functions for amplitude, frequency, phase and timing in a soliton pulse propagated over 55 km. In agreement with the theoretical study of [69], the figure shows that the shape of the timing jitter PDF is Gaussian. Since the propagation distance is small, the tops of the soliton amplitude,

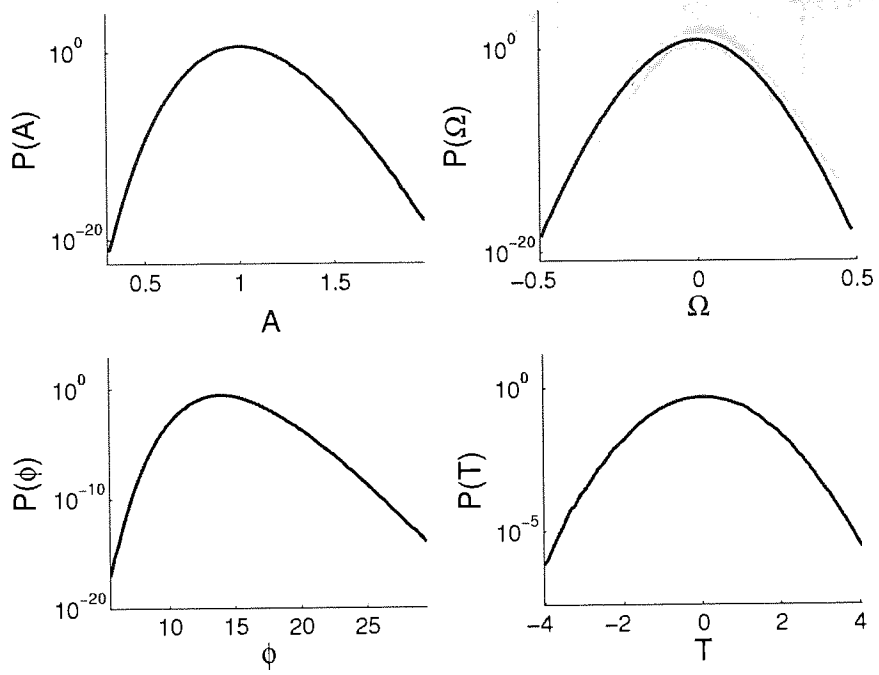

Figure 3.2: Distribution functions of soliton parameters after 55 km.

phase and frequency distributions accurately fit gaussian approximation. Therefore, the gaussian assumption can be used for computing the integral characteristics of these distributions, like, for example, variances. The tails, however, of the amplitude and phase distribution functions are shown to be essentially non-gaussian even at such a short propagation distance. These observations fully agree with the analysis of [66]. In general, this effect may become crucial for accurately evaluating of the probability of erroneous bit detection, since it is the PDFs tails that determine the BER. A very general way to fulfil this task is to approach the problem numerically, by subsequent numerical integration of the PDFs of Figure 3.2. The numerical investigation is particularly important for evaluating the effects of the phase and timing jitter, which dominate other jitters in propagating optical solitons [67], since there is no a comprehensive theory to describe these effects.

As the propagation distance increases, the non-Gaussian nature of the PDFs for the soliton parameters becomes more exposed. Figure 3.3 shows the marginal PDFs for the soliton parameters for a propagation distance of 185 km. As seen from the figure, the timing jitter statistics are in agreement with paper [69], which claims

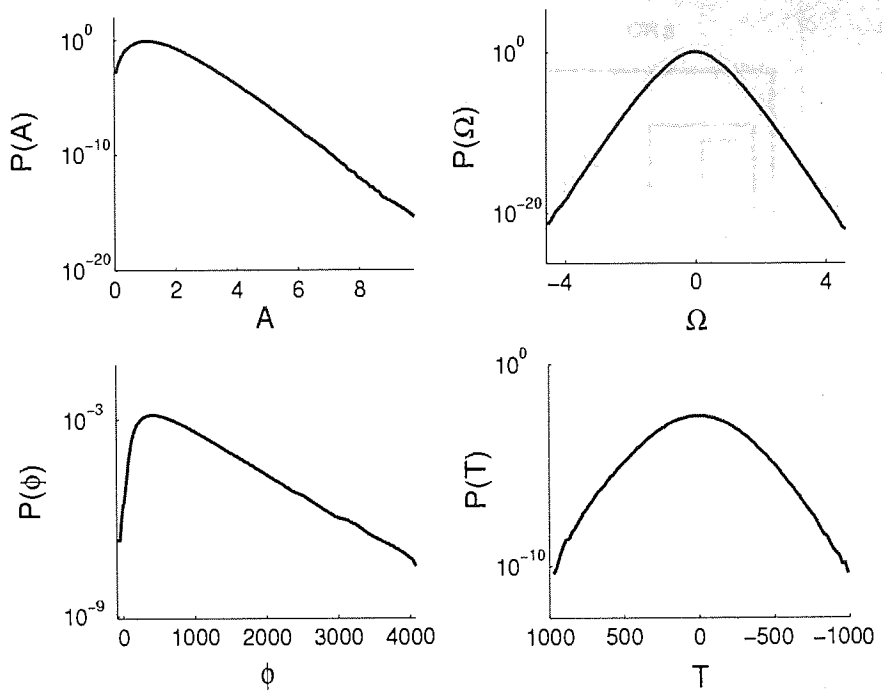

Figure 3.3: Distribution functions of soliton parameters after 185 km.

gaussian statistics for the timing jitter at arbitrary long propagation distance. The nonsymmetry seen in soliton phase statistics is attributed to Gordon-Mollenauer effect [70]. The exponential assimptotic behaviour of the amplitude and phase distribution tales, also seen in Figure 3.2, becomes more evident in this figure. Moreover, even shape of distribution tops for such larger distance is clearly non-gaussian. Therefore, in general, one should use the analytical result of [66] for the amplitude and frequency distributions, while the reliable estimates for the statistics of soliton phase and timing jitters (the most important effects) can be obtained through numerical simulations.

In this subsection we suggested to use the powerful MMC method to calculations of distributions of the phase and timing jitter, which can not be found by means of existing analytical methods. In a typical example of SMF-based transmission link we accurately computed the marginal PDFs for the soliton parameters. Subsequently these results can be applied to evaluation the error probability in such systems. The results of our numerical modelling demonstrate a complete agreement with the conclusions drawn from pre-existing analytical studies.

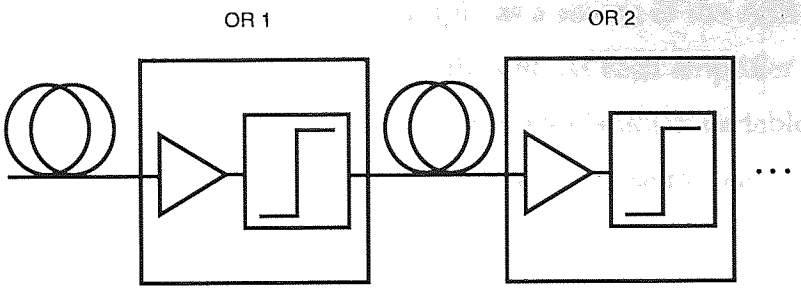

Figure 3.4: Schematic representation of a transmission link with optical regeneration.

3.4 Statistics and BER in transmission systems with optical regeneration

In-line optical regeneration is a powerful tool to enlarge transmission distances by suppressing the accumulation of ASE noise and by reducing signal distortions (see e.g. [29, 59, 71]). Reamplification and reshaping of carrier pulses in 2R optical regenerators (ORs) typically is realized by applying a step-like nonlinear amplitude transfer function. The OR imposes a power threshold on the input pulse and redistributes noise in such a way that signals with powers below the threshold are nearly suppressed, while pulses with powers above the threshold get their amplitude adjusted, thus, the output signal has nearly constant power. Due to inherent nonlinearity of regeneration, signals passing through ORs are subject to reshaping and transformation of their statistical properties. Therefore, the assumption of Gaussian signal statistics does not apply to such systems, invalidating the standard Q-factor approach and making evaluation of the BER a very non-trivial task. In general it is, however, possible to address this problem by using the MMC method, presented in section 3.2. This method increases the number of events in tail regions by biasing them. In this section we apply MMC to compute marks/spaces PDFs and evaluate the BER penalty due to deviations of the decision level from an optimal one in transmission systems with in-line optical regeneration.

We consider a cascade of fibre spans and 2R optical regenerators, as schematically shown on Figure 3.4. The OR is composed of a linear amplifier and a nonlinear gate that is responsible for the suppression of noise and signal reshaping. Here we assume that an amplifier precisely compensates for the losses in the preceding fibre

sections, and, therefore, can be modelled simply as a source of the ASE noise accumulated in the several fibre spans preceding the OR. At each amplifier we append the complex noise to the signal field, where x and y are Gaussian variables with zero mean and variance derived to give an optical signal to noise ratio after one amplifier of 22.2 dB. The nonlinear optical gate is approximated here via the tanh transfer function introduced in [59]:

$$f(x) = \tanh(\gamma x). \tag{3.32}$$

The shape of the transfer function changes with the nonlinearity parameter γ from a step function at $\gamma = 0$ to a linear function at $\gamma = 1$. For completeness, we also consider two simple one-parametric piece-wise linear approximations that are commonly used to model the OR transfer function (see Figure 3.5):

$$f_A(x) = \begin{cases} \gamma_A x, & x < 0.5 \\ \gamma_A (x-1), & \text{otherwise} \end{cases} \tag{3.33}$$

$$f_B(x) = \begin{cases} 0, & x < 0.5 \\ 0.5 + (x-0.5)/\gamma_B, & 1-\gamma_B < 2x < 1+\gamma_B \\ 1, & \text{otherwise} \end{cases} \tag{3.34}$$

The slope parameters γ_A and γ_B determine the tangent of the slope at $x = 0$ for the approximation A and a cotangent of the slope at $x = 0.5$ for the approximation B, respectively. Similarly to the parameter γ, they set the degree of nonlinearity in optical regenerators.

Figure 3.6 represents an example of the evolution of the PDF of "marks" and "spaces" propagating through the line with nonlinear ORs. The nontrivial tails of calculated PDFs come as a result of the nonlinear noise redistribution in ORs. Recall that, the probability of an error (or BER) is determined by the total area under the tails of marks' and spaces' PDFs, limited by the decision level. With the evolution of the tails shape, the value of the BER increases with the number of spans. Furthermore, it is seen that the slope of the marks' PDF at the optimal decision level (crossing point) is reducing with growth in the number of spans, making them almost constant. Consequently, if the decision is made at a level right shifted from the optimal one, the calculated BER, almost entirely determined by PDFs of marks in this case, is very close to the optimal value. This suggests the improvement in tolerance with

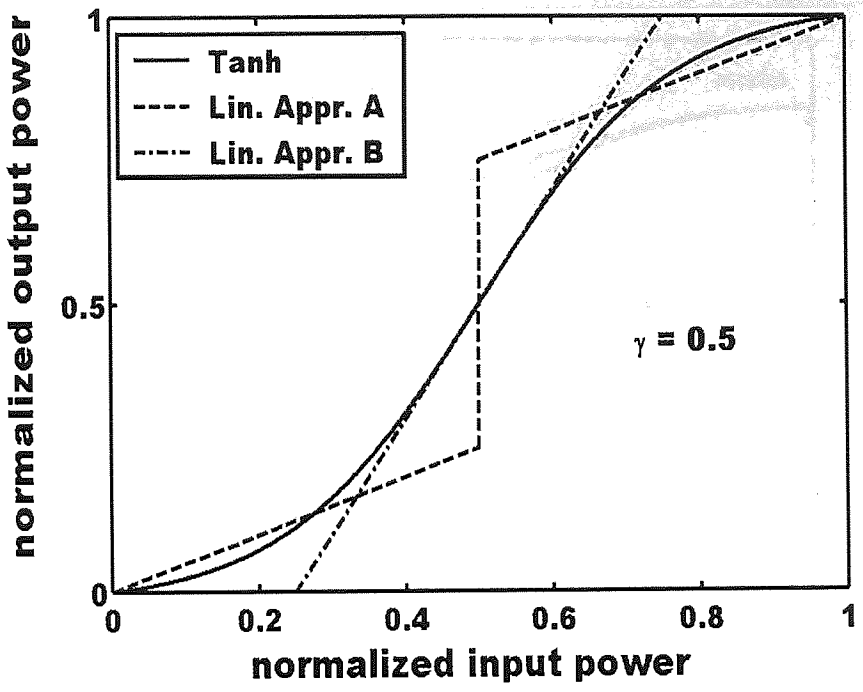

Figure 3.5: Tanh-shaped transfer function and its linear approximations A and B shown for $\gamma = 0.5$.

the number of OR spans. Figure 3.7 compares PDFs measured for linear approximations and tangent hyperbolic transfer function after 5 spans for $\gamma = \gamma_A = \gamma_B = 0.5$. Although, the observed small difference in the BERs between linear approximations and tanh transfer function can be suppressed by optimisation of the parameters γ_A and γ_B, the difference in shapes of the PDFs will produce the discrepancy in tolerance to the decision level. The figure shows that the approximation A demonstrates strong disagreement with the nonlinear transfer function, in particular, around 0.4. The deep observed here can be attributed to essentially nonlinear behaviour of the approximation A in the vicinity of the decision level (see Figure 3.5). The approximation B, on the other hand, yields much better agreement with tangent hyperbolic transfer function, which underlines the importance of accurate approximation around threshold, where the BER is estimated. Now we compare the performance of the two linear approximations of the nonlinear transfer function in terms of BER. Figure 3.8 shows the evolution of the BER versus the number of OR spans for different values of the nonlinear parameter γ. Also, there are shown for comparison results for the linear approximations with (non-optimal) $\gamma_A = 0.5$ and $\gamma_B = 0.5$. It is

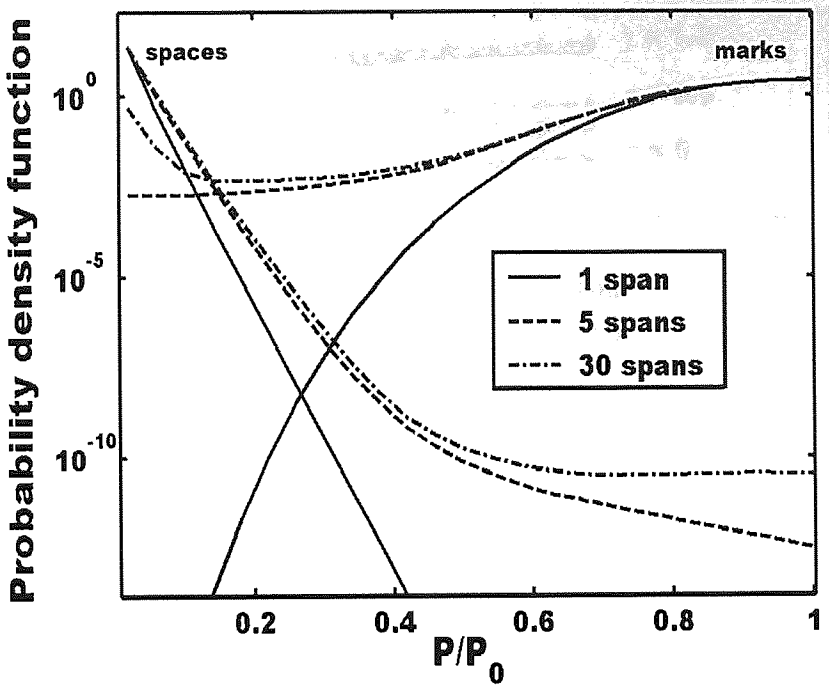

Figure 3.6: PDFs of marks and spaces after 1, 5 and 30 spans for tanh-shaped transfer function, $\gamma = 0.5$.

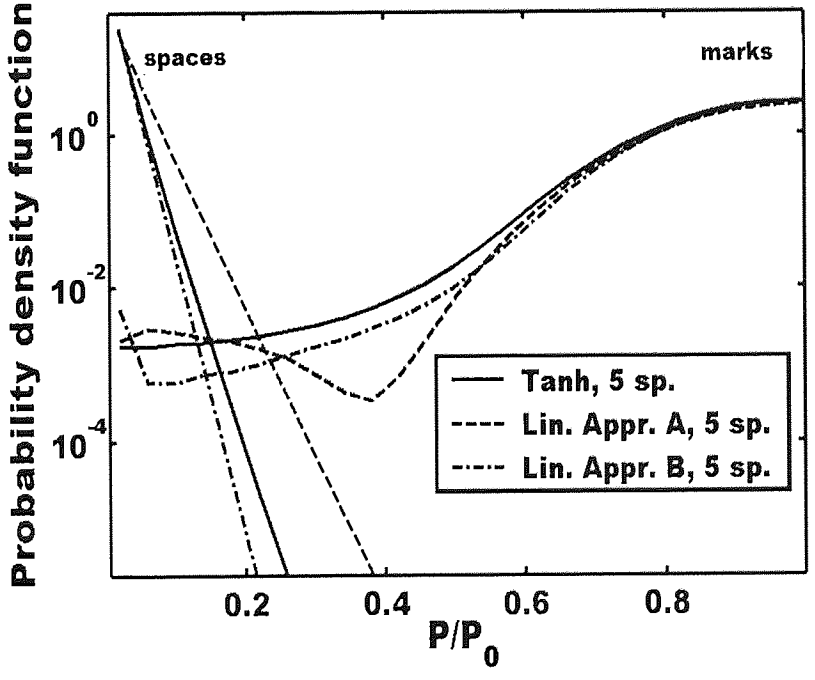

Figure 3.7: Comparison between PDFs of marks and spaces for tanh-shaped transfer function and its linear approximations after 5 spans ($\gamma = \gamma_A = \gamma_B = 0.5$).

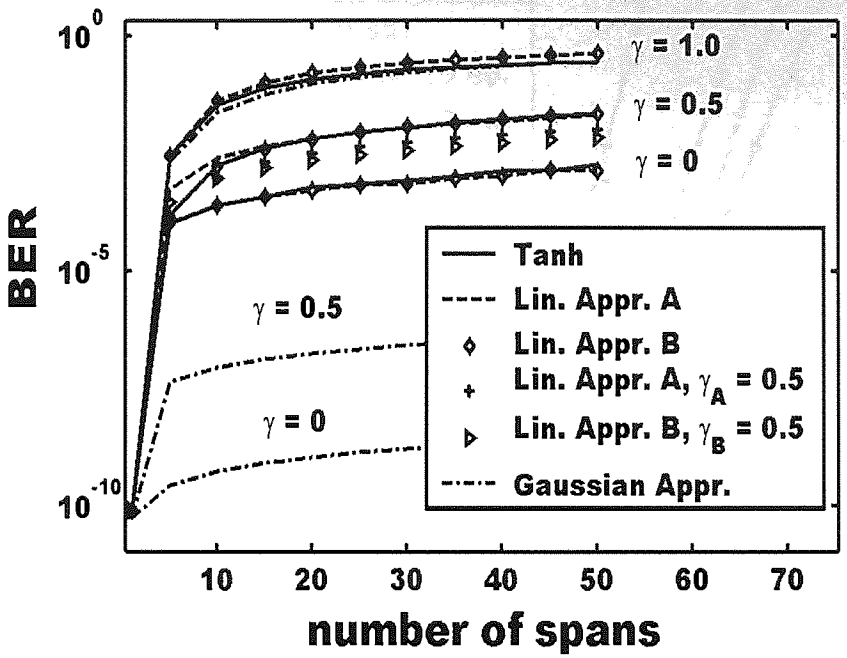

Figure 3.8: BER evolution with increase of number of OR spans.

seen that the intuitively reasonable choice of parameters for the linear transfer functions $\gamma_A = \gamma_B = \gamma$ does not necessarily give the most accurate approximation of the BER, as is seen from the example with $\gamma = 0.5$. For instance, for $\gamma = 0.5$ the optimised parameters of the linear approximations are: $\gamma_A = 0.65$ and $\gamma_B = 0.6$. Recall, that the Gaussian approximations for the signal statistics (shown by dash-dotted curves in Figure 3.8) drastically deviate from the true BER evolution. Non-Gaussian tails of the PDFs for marks/spaces lead to a non-trivial dependence of the BER on the decision level. To investigate the tolerance of the BER with respect to the decision threshold we employed a concept of BER penalty. The BER penalty is defined through a BER for a given decision current normalised to its optimal value (i.e. the BER estimated at the optimal decision threshold). Figure 3.9 presents the BER penalty versus decision level evaluated after ten and fifty spans for $\gamma = 0.5$. Improvement in the tolerance of the BER is observed with an increasing number of OR spans. As already was mentioned, this effect might be attributed to a growing flatness of the distribution function for the "marks". Moreover, a very good agreement is seen between the linear approximation B and the tanh-shaped transfer function. The approximation

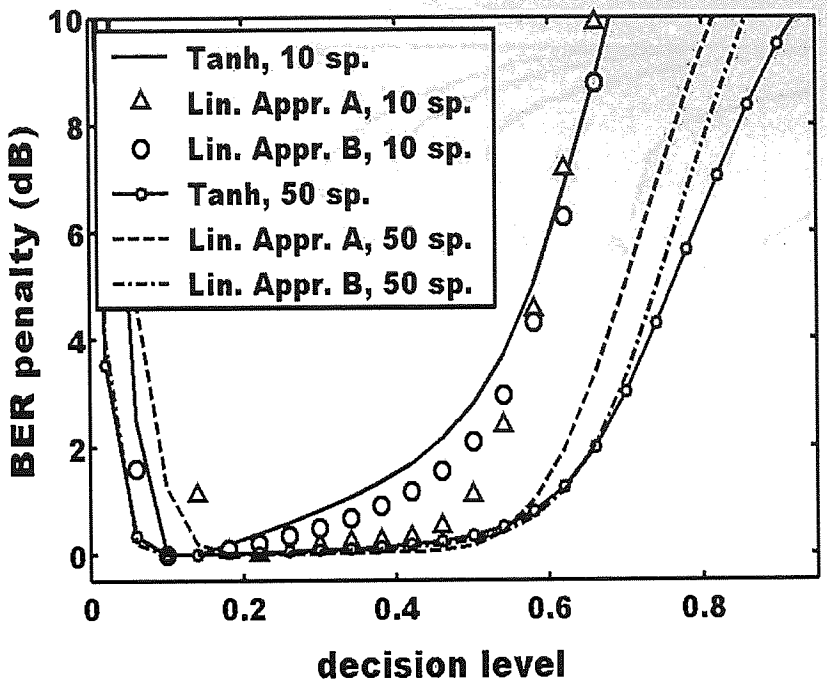

Figure 3.9: BER penalty plotted versus the decision level; here $\gamma = 0.5$.

A deviates from the right values of BER at decision level of 0.5 after 10 spans by 1.7dB, and at decision level of 0.7 after 50 spans by 2 dB. The better accuracy in the case B compared to the approximation A is due to the fact that the approximation B is fitted to the original tangent hyperbolic transfer function in the vicinity of 0.5 - the range of currents that determines the tails of the signal distributions, and consequently, the BER. Figure 3.10 shows a contour plot for the BER penalty after 25 spans plotted as a function of the nonlinear parameter γ and the decision threshold. Rather good tolerance margins of the BER to the decision level can be observed for γ varying in the interval from 0 to 0.7 and the decision level from 0.1 to 0.5. This is an indication that the ORs with strong nonlinear response can tolerate sufficiently larger variations in the decision level.

In conclusion, applying a powerful MMC method in this section we have studied the BER penalty caused by deviations from the optimal decision level in systems employing in-line optical regeneration. We have demonstrated that the analytical linear approximation B making better fit in the central part of the regenerator nonlinear transfer function gives more accurate approximation of the BER and BER

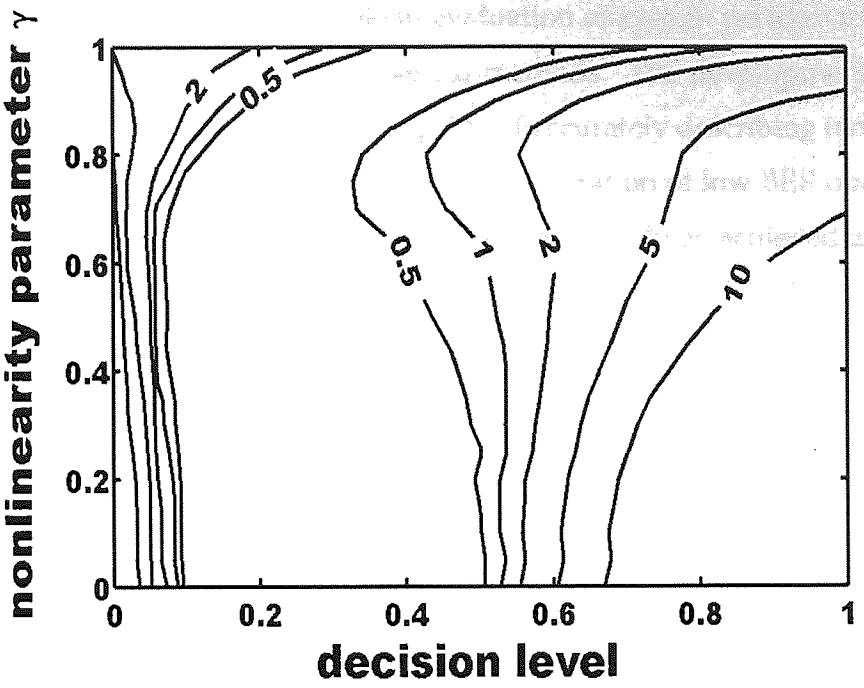

Figure 3.10: BER penalty after 25 OR spans in the plane of nonlinear parameter γ and decision level.

penalty compared to commonly used approximation A.

3.5 BER in optical links using RZ-DPSK modulation format

Differential phase-shift keying (DPSK) transmission systems attract renewed attention in optical communication due to improved receiver sensitivity and longer transmission distances. The principle behind DPSK is encoding information in phase difference between neighbouring pulses, which is chosen to be 0 for marks and π for spaces. Two matched Mach-Zehnder interferometers (MZI) placed at the transmitter and the receiver carry out the modulation and demodulation of signals. Signal amplification, compulsory in long-haul transmission, introduces amplitude, frequency, time and phase fluctuations of the carrier pulse. These perturbations of pulse parameters impair the system performance and enhance the probability of detecting an error at the receiver. Owing to very low BER levels required in modern optical transmission systems, direct measurements of the BER are very time-consuming and

almost impractical. An important role in evaluation of system performance is then played by indirect statistical and numerical methods. The development of novel mathematical and numerical methods capable of accurately describing received signal statistics is crucial for progressing to a new generation of low BER optical communication networks. Recently a significant progress has been achieved in this area (see e.g. [67,72–76]). The ASE noise introduces random amplitude, frequency, time and phase fluctuations of the carrier pulse. Such perturbations of pulse parameters manifest themselves as corresponding jitters that impair the system performance and enhance the probability of detecting an error at the receiver. Note that very different physical effects can often cause similar distortions of the received signal during propagation. Therefore, it is of interest to analyse the statistics of the signal assuming some general form of the most typical distortions.

In this section, we present theoretical and numerical analysis of the statistics of direct detection RZ-DPSK optical signals at the receivers with MZI demodulation. We examine the RZ-DPSK signal statistics in a situation when the carrier pulses at the receiver are deteriorated simultaneously by phase and timing jitters. Note that in many practical situations amplitude and frequency jitters can be neglected since they grow comparatively slower with the propagation distance [67]. In the limit of narrow pulses - when the pulse width is small compared to the time bit slot, we derive a simple close-form analytical expression for the BER. We verify the analytical results by numerical simulations, using the MMC method recognised for its efficiency in calculations of the distributions tails.

3.5.1 Two pulse analysis

In this subsection we consider only two interfering pulses affected by phase and timing jitter. At the receiver the signal is decoded using the MZI with the optical delay identical to the time duration of one bit slot. The DPSK modulated signal enters both arms of the interferometer experiencing the delay in one of the arms. In the two-pulse approximation the signals travelling in the different arms of the

interferometer are given by

$$S_1(t) = S(t-T_1)e^{i\phi_1}, \tag{3.35}$$

$$S_2(t) = S(t-T_2)e^{i(\phi+\phi_2)}, \tag{3.36}$$

where $S(t)$ is a real-valued carrier pulse envelope, ϕ is a phase shift introduced by the modulator (0 if logical one is transmitted, otherwise π), and random variables ϕ_1, ϕ_2 and T_1, T_2 account for the phase and timing jitter of the pulses. Here we neglect the effect of neighbouring bits on the two pulses. In the interferometer the half sum and half difference between pulses S_1 and S_2 are calculated in the constructive and destructive arms. Subsequently, square-law optical detectors detect the interferometer outputs and the differential electric current

$$I(t) = \frac{1}{4}\left(|S_1(t)+S_2(t)|^2 - |S_1(t)-S_2(t)|^2\right) \tag{3.37}$$

is sent to the decision device. By combining (3.35) and (3.36), equation (3.37) becomes

$$I(t) = S(t-T_1)S(t-T_2)\cos(\phi_1-\phi-\phi_2). \tag{3.38}$$

The decision on whether a mark or a space has been received is based on the current averaged over the time bit slot:

$$I = \frac{\kappa}{T_B}\int_{-T_B/2}^{T_B/2} I(t)\,dt. \tag{3.39}$$

By use of (3.38), we obtain

$$I = F(T_1,T_2)\cos(\phi_1-\phi-\phi_2), \tag{3.40}$$

where

$$F(T_1,T_2) = \frac{\kappa}{T_B}\int_{-T_B/2}^{T_B/2} S(t-T_1)S(t-T_2)\,dt. \tag{3.41}$$

In order to calculate the BER we need to analyse the statistical properties of the received signals and this can be done by use of the standard technique of the characteristic function, described in [73]. By definition, the characteristic function for a random variable is given by the Fourier transform of the probability function $f(t)$:

$$\chi(x) = \int_{-\infty}^{\infty} e^{ixt} f(t)\,dt. \tag{3.42}$$

Therefore, the PDF $f(t)$ can be calculated as

$$f(t) = \frac{1}{2\pi}\int_{-\infty}^{\infty} e^{-ixt}\chi(x)\,dx. \tag{3.43}$$

On the other hand, the characteristic function satisfies the relation [77]

$$\chi(x) = \langle e^{ixu}\rangle \tag{3.44}$$

which yields for the current I of marks:

$$\chi(x) = \int_{-\infty}^{\infty} J(x,T_1,T_2)\,f_T(T_1)\,f_T(T_2)\,dT_1 dT_2. \tag{3.45}$$

where

$$J(x,T_1,T_2) = \int_{-\infty}^{\infty} e^{ixF(T_1,T_2)\cos(\phi_1-\phi_2)} f_\phi(\phi_1)\,f_\phi(\phi_2)\,d\phi_1\,d\phi_2 \tag{3.46}$$

and $f_T(x)$ and $f_\phi(x)$ represent the PDFs for the timing and the phase jitter, respectively. Assuming that the phase jitter is gaussian, i.e.

$$f_\phi(x) = \frac{1}{\sqrt{2\pi\sigma_\phi^2}} e^{-\frac{x^2}{2\sigma_\phi^2}}, \tag{3.47}$$

integral J can be converted to

$$J(x,T_1,T_2) = \frac{1}{2\sqrt{\pi\sigma_\phi^2}}\int_{-\infty}^{\infty} \exp\left(ixF(T_1,T_2)\cos\phi - \frac{\phi^2}{4\sigma_\phi^2}\right) d\phi. \tag{3.48}$$

When the phase jitter variance is sufficiently small $\sigma_\phi \ll \pi/\sqrt{2}$, J can be approximated by

$$J(x,T_1,T_2) = \frac{1}{\sqrt{\pi\sigma_\phi^2}}\int_{0}^{\pi} \exp\left(ixF(T_1,T_2)\cos\phi - \frac{\phi^2}{4\sigma_\phi^2}\right) d\phi, \tag{3.49}$$

After making the substitution $z = F(T_1,T_2)\cos(\phi)$, integral (3.49) becomes

$$\begin{aligned} J(x,T_1,T_2) \;=\; & \int_{-\infty}^{\infty} H\left(1-\frac{|z|}{|F(T_1,T_2)|}\right) \frac{e^{ixz}}{F(T_1,T_2)\,\sigma_\phi\sqrt{\pi\left(1-\frac{z^2}{F(T_1,T_2)^2}\right)}} \times \\ & \exp\left(-\frac{\arccos^2\left(\frac{z}{F(T_1,T_2)}\right)}{4\sigma_\phi^2}\right) dz, \end{aligned} \tag{3.50}$$

where H is the Heaviside step function. Using expressions (3.50), (3.45) and (3.43), the sought probability density function for marks reads

$$f_{marks}(t) = \int_{-\infty}^{\infty} \Phi(t,T_1,T_2)\,f_T(T_1)\,f_T(T_2)\,dT_1 dT_2. \tag{3.51}$$

where

$$\Phi(t,T_1,T_2) = \frac{1}{2\pi}\int_{-\infty}^{\infty} H\left(1-\frac{z}{F(T_1,T_2)}\right)\frac{e^{ix(z-t)}}{F(T_1,T_2)\,\sigma_\phi\sqrt{\pi\left(1-\frac{z^2}{F(T_1,T_2)^2}\right)}}\times$$
$$\exp\left(-\frac{\arccos^2\left(\frac{z}{F(T_1,T_2)}\right)}{4\sigma_\phi^2}\right)dz\,dx \tag{3.52}$$

This expression can be rewritten as

$$\Phi(t,T_1,T_2) = \int_{-\infty}^{\infty} H\left(1-\frac{z}{F(T_1,T_2)}\right)\frac{\delta(t-z)}{F(T_1,T_2)\,\sigma_\phi\sqrt{\pi\left(1-\frac{z^2}{F(T_1,T_2)^2}\right)}}\times$$
$$\exp\left(-\frac{\arccos^2\left(\frac{z}{F(T_1,T_2)}\right)}{4\sigma_\phi^2}\right)dz, \tag{3.53}$$

where $\delta(x)$ is the delta function, and subsequently integrated to give

$$\Phi(t,T_1,T_2) = H\left(1-\frac{t}{F(T_1,T_2)}\right)\frac{1}{F(T_1,T_2)\,\sigma_\phi\sqrt{\pi\left(1-\frac{t^2}{F(T_1,T_2)^2}\right)}}\times$$
$$\exp\left(-\frac{\arccos^2\left(\frac{t}{F(T_1,T_2)}\right)}{4\sigma_\phi^2}\right). \tag{3.54}$$

The distribution function in (3.51), hence, is found to be

$$f_{marks}(t) = \int_{-\infty}^{\infty} H\left(1-\frac{|t|}{|F(T_1,T_2)|}\right)\frac{f_T(T_1)\,f_T(T_2)}{F(T_1,T_2)\,\sigma_\phi\sqrt{\pi\left(1-\frac{t^2}{F(T_1,T_2)^2}\right)}}\times$$
$$\exp\left(-\frac{\arccos^2\left(\frac{t}{F(T_1,T_2)}\right)}{4\sigma_\phi^2}\right)dT_1\,dT_2, \tag{3.55}$$

The PDF for spaces can be derived from expression (3.55) by substitution $t \to -t$. Following the symmetry of the problem, the optimal decision threshold is zero and, thus, the BER reads:

$$BER = \int_{-I_0}^{0} f_{marks}(t)\,dt, \tag{3.56}$$

where $I_0 = F(0,0)$ represents the maximum value of the received current I. Indeed, according to (3.41), function $F(T_1,T_2)$, associated with the overlapping area between two shifted pulses, attains its maximum when the pulses are centred in the middle of

the bit slot ($T_1 = T_2 = 0$). Incorporating PDF (3.55) into (3.56) and using the property that $F(T_1, T_2) \leq F(0,0)$, the BER becomes

$$BER = \int_{-\infty}^{\infty} \left\{ \int_{-F(T_1,T_2)}^{0} \frac{1}{F(T_1,T_2)\,\sigma_\phi \sqrt{\pi\left(1 - \frac{t^2}{F(T_1,T_2)^2}\right)}} \times \right.$$
$$\left. \exp\left(- \frac{\arccos^2\left(\frac{t}{F(T_1,T_2)}\right)}{4\sigma_\phi^2} \right) dt \right\} f_T(T_1)\, f_T(T_2)\, dT_1\, dT_2, \qquad (3.57)$$

Via change of the integration variable to $x = \arccos(t/F(T_1,T_2))$ and by integrating timing jitters T_1 and T_2 we obtain the final answer for the BER:

$$BER_{phase} = \int_{\infty}^{-\pi/2} \frac{1}{\sigma_\phi \sqrt{\pi}} \exp\left(- \frac{x^2}{4\sigma_\phi^2} \right) dx = \operatorname{erfc}\left(\frac{\pi}{4\sigma_\phi} \right). \qquad (3.58)$$

According to relation (3.58), the BER represents the probability of detecting the phase shift between two pulses outside the interval $[-\pi/2, \pi/2]$. Seemingly surprising the fact that the probability of an error found by examining two consecutive pulses has no dependency on the timing jitter yields a simple explanation. Indeed, consider the limit of pulses separated by large distances $|T_1 - T_2| \to \infty$, when the decision quantity I is vanishingly small due to a small overlapping area $F(T_1, T_2)$. As the sign of I can not change and due to the zero decision threshold the signal can not be detected erroneously, the timing jitter does not affect the BER. Figure 3.11 illustrates this effect. The figure shows the numerically estimated PDFs for "marks" and "spaces" plotted as functions of the normalised current I. In our simulations the phase jitter standard deviation σ_ϕ is set to 0.2. Moreover, we model the timing jitter by a gaussian random variable with the deviation σ_T, measured in units of the bit period T_B. Considering conventional soliton pulses, we apply the MMC approach to investigation of the PDF of I in the two pulse model given by (3.39). In our simulations we use 50,000 realizations of random variables in the first MMC iteration and increase this number by 15% in the each following iteration. Within the each iteration we employ Metropolis algorithm to produce a random walk of samples, with the step size adjusted so that the acceptance ratio is around 0.5. In this example the accurate estimation of the signal distributions requires up to 10 iterations. It can be seen in Figure 3.11 that the shapes of the distribution functions tops, associated with

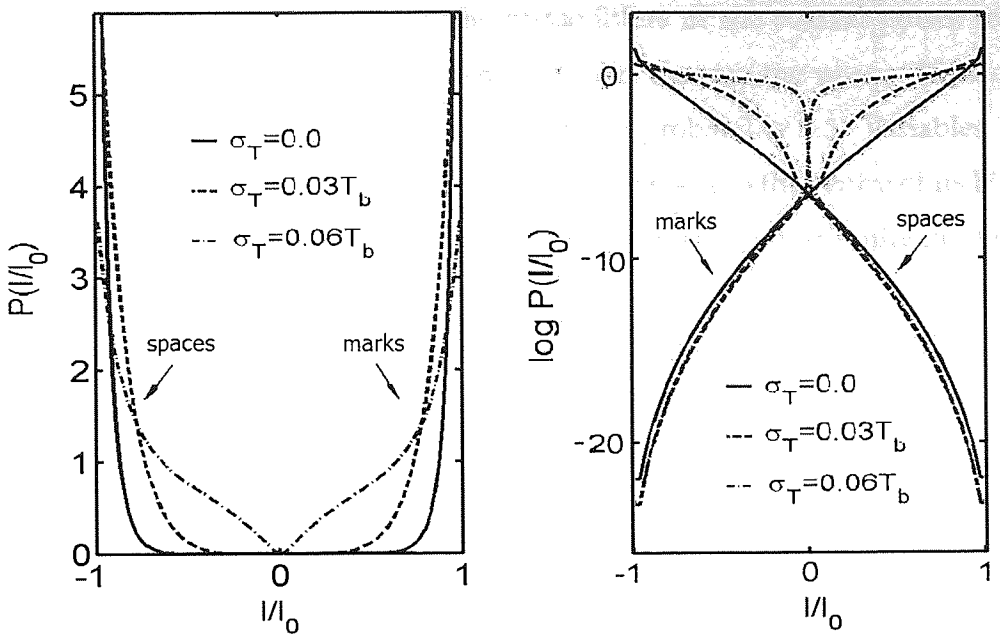

Figure 3.11: PDF of the current for marks and spaces for different values of timing jitter variance and $\sigma_\phi = 0.2$ in linear (left) and logarithmic (right) scales.

the positive I for "marks" and negative I for "spaces", show a strong dependency on the timing jitter. In particular, the probability of detecting the current I around zero increases with increasing σ_T. As previously mentioned, this effect is attributed to a decrease in the overlapping area between the pulses, observed for large separation distances. However, the tails of the "marks" and "spaces" PDFs are shown to nearly coincide for the considered values of the timing jitter variance. This is a clear indication that the BER does not depend on σ_T within the two-pulse approximation. Therefore, the evaluation of the effect of timing jitter on the BER requires a more accurate analysis, which is presented in the following subsection.

3.5.2 Four-pulse analysis

To account for the impact of the timing jitter on the error probability we choose to model the received signal by four successive pulses. In the four-pulse representation the signal in the two arms of the interferometer is given by

$$S_1(t) = S(t - T_0 + T_B) + S(t - T_1) + S(t - T_2 - T_B)e^{i\phi_2} \tag{3.59}$$

$$S_2(t) = S(t - T_{-1} + T_B)e^{i\phi_{-1}} + S(t - T_0) + S(t - T_1 - T_B). \tag{3.60}$$

In relations (3.59) and (3.60) we set the phase jitters of the central pulses to zero $\phi_0 = \phi_1 = 0$, assuming a "mark" transmitted, and assume the phase shifts of the appended pulses ϕ_{-1} and ϕ_2 to be 0 or π with the probability 0.5. Variables T_j for $j = -1, \ldots, 2$ is the timing jitter in the pulse j with respect to the centre of its bit slot. In this subsection we safely neglect the phase jitter, since its contribution to the BER has already been calculated.

Considering the case of narrow pulses, i.e. $T \ll T_B$, we further simplify the analysis by using pulses of the rectangular shape:

$$S(t) = \begin{cases} c & \text{if } |t| < T/2 \\ 0 & \text{otherwise} \end{cases} \tag{3.61}$$

It is intuitively clear, that the highest probability for an erroneous bit detection due to timing jitter to occur is given by a situation when one of the detected pulses is replaced with a neighbouring pulse of the opposite phase. In the square pulse model such a situation is conditioned by the requirement that after the time delay T_B introduced by the MZI the detected pulses overlap. Accounting for the left and right neighbouring pulses the probability of an error reads then

$$P(error) \approx \frac{1}{2}\left(P\left(|T_{-1} - T_b - T_1| < T\right) + P\left(|T_2 + T_b - T_0| < T\right)\right) \tag{3.62}$$

where factor $1/2$ comes from the 50% probability of the neighbouring pulse to have an opposite phase. Considering timing jitters T_j to be independent Gaussian random variables with zero mean and the variance σ_T^2, the BER is then given by

$$BER_{time} = \frac{1}{2}\left(erf\left(\frac{T_B + T}{2\sigma_T}\right) - erf\left(\frac{T_B - T}{2\sigma_T}\right)\right). \tag{3.63}$$

Combining this expression with the previously derived BER for the phase jitter (equation 3.58), we get the total error probability

$$BER = BER_{phase} + BER_{time} = erfc\left(\frac{\pi}{4\sigma_\phi}\right) + \frac{1}{2}\left(erf\left(\frac{T_B + T}{2\sigma_T}\right) - erf\left(\frac{T_B - T}{2\sigma_T}\right)\right). \tag{3.64}$$

To verify the accuracy of the analytical formula we perform direct numerical modelling of RZ-DPSK modulated signals. In particular, we apply the advanced MMC method to the calculation of signal distributions and evaluation of the BER. Without loss of generality, in these simulations we use *sech* shaped pulses with the full-width

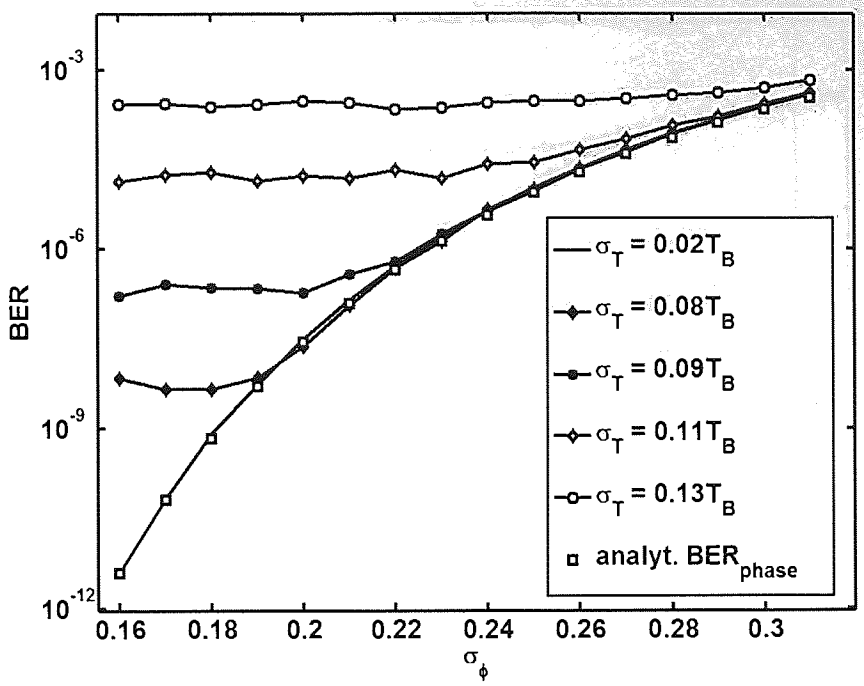

Figure 3.12: The BER as a function of σ_ϕ for different values of σ_T.

at half-maximum of 0.1763 measured in the units of the time bit slot duration. To account for the difference in shape between the soliton and square pulses, in analytical expressions we multiply this value by a factor 2. Indeed, the calculations of probability of the pulse overlap should be rather based on the pulse width at the bottom level than at the half maximum. To attain a higher accuracy in our simulations we use six pulses model.

On Figure 3.12 the BERs are plotted versus the phase standard deviation for different values of σ_T. The analytical solution in (3.58) is also shown for comparison. The figure shows that when the timing jitter is substantially small it is solely the phase jitter that determines the probability of an error. The analytically found BER_{phase} (see equation (3.58)), moreover, shows an excellent agreement with the error probability for such small σ_T. However, as the timing jitter grows, its contribution to the error probability increases, until eventually it overtakes the impact of the phase jitter. In this situation the contribution of the phase jitter becomes negligible, as the independence of the curves of σ_ϕ shows.

Figure 3.13 shows the BER plotted against the timing jitter standard deviation.

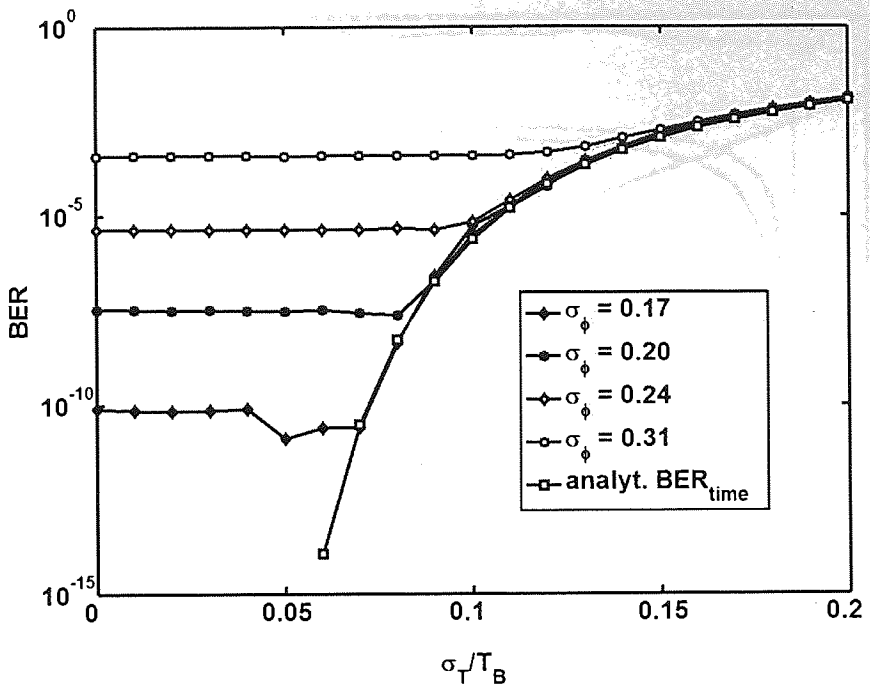

Figure 3.13: The BER plotted with respect to σ_T for several values of σ_ϕ.

In agreement with earlier observations, the figure shows that for relatively small standard deviations of the phase jitter, the effect of the timing jitter becomes determining for the BER. In contrast, when the variance of the phase fluctuations grows sufficiently large, the errors due to the phase jitter prevail so strongly, that the effect of the timing jitter becomes negligible for the BER. Moreover, the very good agreement between the numerically estimated BERs and the BER_{time} solution in (3.63) demonstrates that our approximate approach used to estimate the BER due to timing jitter is sufficiently accurate. In particular, such a good agreement validates the restriction of considering the impact to the error probability only from immediate neighbouring pulses.

The conclusions drawn from Figures 3.12 and 3.13 are more evident from the contour plot of Figure 3.14, where the BER is plotted as a function of the phase and timing jitter standard deviations. It is seen that the analytical solution given by formula (3.64) is in a good agreement with the results of numerical calculations. The figure shows three distinct regions in the plane of parameters σ_T and σ_ϕ. In the first region the BER is determined entirely by phase jitter. This case corresponds

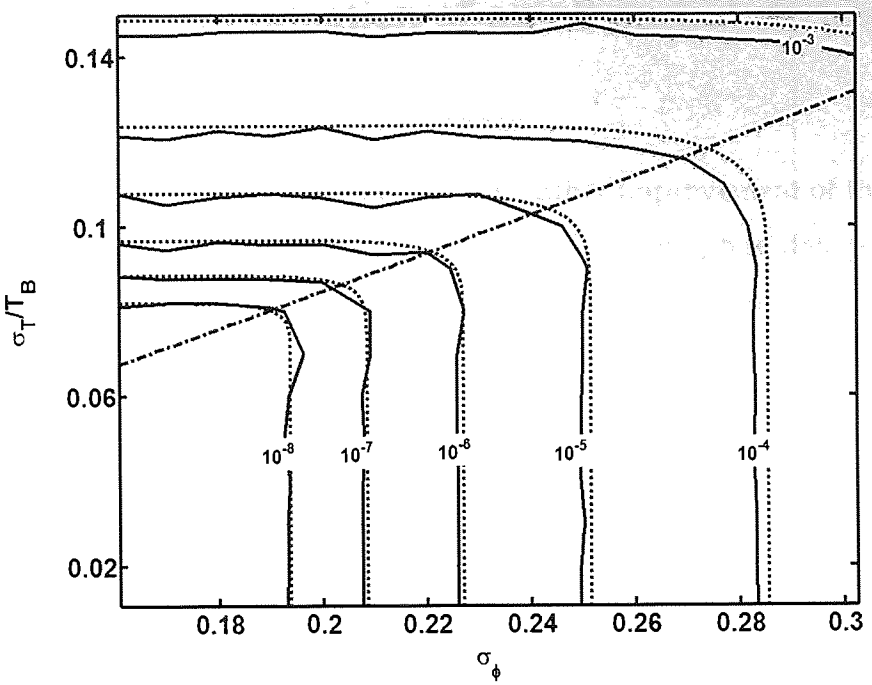

Figure 3.14: Contour plot showing the BER versus σ_ϕ and σ_T. Dotted lines: analytical results; solid lines: numerical results.

to relatively small values of the timing jitter variance, when the probability for a pulse to leave the bit window and overlap with another narrow pulse is negligible compared to the probability for the pulse phase difference to fall outside the interval $[-\pi/2, \pi/2]$. In the second region it is the timing jitter that determines the probability of an error. The dash-dotted line marks the edge between the regions, where the BERs due to the phase and the timing jitter are equal. Around this line there is a small area, where both parameters contribute to the BER.

In summary, we analysed theoretically and numerically the statistical properties of RZ-DPSK optical signals in transmission lines with MZI balanced detection. A close-form analytical expression for the error probability due to the phase and temporal position fluctuations was presented. The theoretical results were fully confirmed by numerical MMC simulations.

3.6 Performance evaluation of an all optical decision element

Signal processing is an attractive technique for further improvement of the performance of fibre transmission systems. The full potential of all-optical data processing is still to be realized in a variety of possible applications. Existing optical regenerative devices operate in accordance with a transfer function, which defines an unambiguous relation between the input and output optical signal intensities. In this section we consider a design based on employing an additional all-optical decision element (ODE) just before the conventional receiver. By this way, a first decision is carried out in the optical domain, improving the quality of the signal to be received. This improves the receiver performance while avoiding the employment of expensive electronic and optoelectronic components to perform signal sampling for data decision after detection. A number of nonlinear ODE schemes have been recently proposed [78–81].

For systems using optical decision elements, the inherent nonlinearity of the employed optical devices causes the received-voltage PDFs of marks and spaces to have an essentially non-Gaussian shape. This invalidates the use of standard estimates of the BER in terms of the well-known Q-factor of the signal, which is based on the Gaussian approximation for the statistics. Therefore, in this section, we apply the MMC simulation technique to compute the performance of an RZ optical receiver enhanced by a nonlinear ODE. As an examplanary system, here we consider the ODE-enhanced receiver proposed in [80] and, by MMC simulations, we demonstrate an observable improvement in the BER compared to the conventional receiver, when the receiver is applied to the 40Gb/s signals.

The structure of the examined ODE-enhanced receiver is shown in Figure 3.15. The receiver is constructed by an optical bandpass filter/demultiplexer, a photodetector with a square-law characteristic, an electrical low-pass filter, and a threshold detector at the decision point. The ODE, placed in front of the receiver, consists of an EDFA, a section of normal dispersion fibre (NDF), and an optical temporal gating device [80]. The principle of the decision function in the optical domain is as follows.

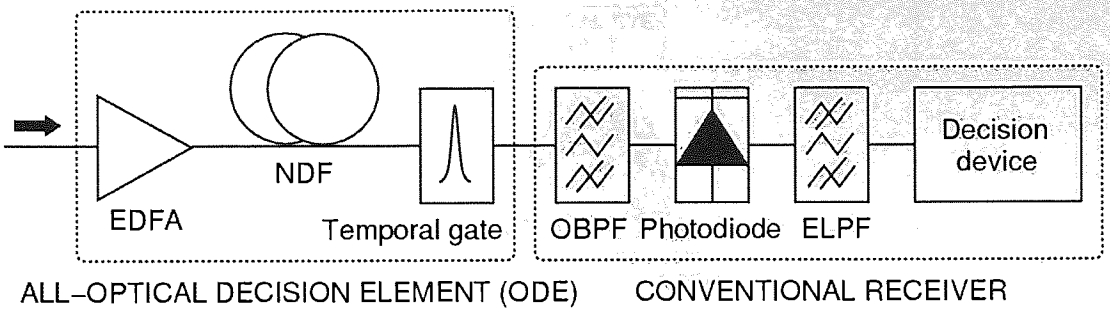

Figure 3.15: Scheme of the RZ optical receiver. (OBPF: optical bandpass filter; ELPF: electrical low-pass filter).

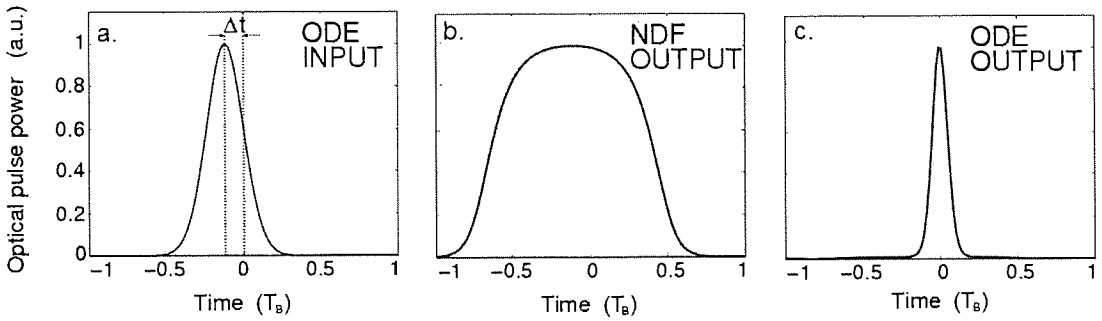

Figure 3.16: Optical signal profile.

An input optical pulse to the ODE (shown in Figure 3.16a) is first amplified by the optical amplifier in order to enhance the effect of nonlinearity in the NDF. During transmission along the NDF, the temporal waveform of the pulse is changed to a rectangular-like profile by the combined action of GVD and Kerr nonlinearity [82]. As a result, the pulse width is broadened and the centre portion of the pulse changes to be flat (see Figure 3.16b). Following the NDF, the pulse enters the temporal gating device. The gate slices the centre portion of the broadened pulse temporal profile, as shown in Figure 3.16c. As a temporal gate one can use, for example, an amplitude modulator with a specially designed nonlinear transfer function [80] given by

$$f(t) = x + (1-x)\cos^{2m}(\pi(t-t_0)/T_B). \tag{3.65}$$

Here, x is the extinction ratio, t_0 is the centre of the modulation, T_B is the bit period, and parameter $m = 1, 2, \ldots$ controls the degree of narrowing and sharpening of the modulation peaks and, thus, the degree of slicing of the pulse temporal profile.

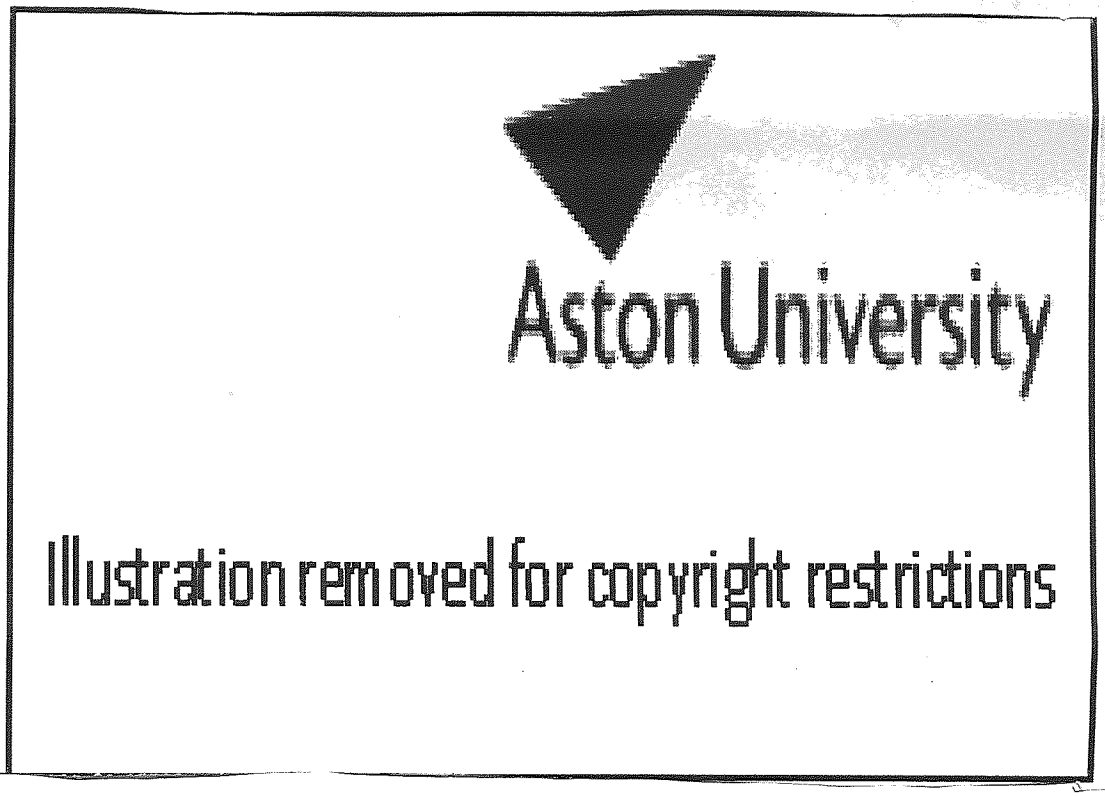

Figure 3.17: Signal eye-diagram in the receiver.

Strongly time-shifted pulses in the optical domain, once they are converted into electrical pulses and arrive at the decision point, might be missed by the threshold detector in a conventional receiver. In contrast to that, the temporal broadening and flattening-induced bit slot recovery in the NDF enables such originally strongly shifted pulses to be recognised as marks in the modified receiver. This is the basic mechanism that is responsible for BER improvement in the ODE-enhanced receiver.

An idea of such an improvement in signal quality achievable in the ODE-modified receiver with respect to the conventional receiver is illustrated by the eye-diagrams [80] in Figure 3.17. An eye diagram provides a visual indication of the power and timing uncertainty associated with the signal at the detector. The eye of the optical input 40 Gb/s RZ signal is closed mainly due to a significant timing jitter of the pulses. When the pulses are detected with the conventional scheme, the pulse width is broadened by the electrical filter, and this yields increase of the eye-opening. The eye-opening detected with the proposed scheme is larger than that in the conventional receiver. This is due to a substantial suppression of the timing jitter, which results from the temporal slicing of the NDF-broadened and flattened pulse wave-

forms by the amplitude modulator.

In this section we propose a quantitative analysis of the performance of the nonlinear ODE-enhanced receiver. Our simulated system is identical to [80]. In particular the NDF has a length of 0.5 km, a dispersion of -20 ps /(nm km), a nonlinear coefficient of 4.28 $(\mathrm{W\,km})^{-1}$, and an attenuation of 0.24 dB/km. The bandwidths of the optical bandpass filter and electrical low-pass filter are set to the respective (optimal) values of 400 GHz and 20 GHz for the conventional receiver, and of 400 GHz and 40 GHz for the ODE-enhanced receiver. The gain of EDFA is 34.2 dB and it has a noise figure of 4.5 dB. The transfer function (3.65) for the amplitude modulator is used with $x = 0.1$ and $m = 12$. In order to account for pulse-to-pulse interaction in our simulations we model the signal to be received by a 8-bit random binary sequence with a bit period of $T_{\mathrm{B}} = 25\,\mathrm{ps}$. The signal pulses are Gaussian-shaped, and have a full-width at half-maximum duration of 7 ps and a peak power of 1.6 mW at the input of the optical decision element. Timing jitter in the signal is modelled by a superposed Gaussian-distributed random shift of the pulse temporal position. The timing jitter standard deviation is 3 ps, unless otherwise specified. When passing the EDFA in the modified receiver, a complex Gaussian random noise is appended to the complex signal field. By applying the MMC method, we calculate the distribution of the voltage of the marks and spaces at the decision point in the receiver. We use 30,000 realizations of random variables in the first MMC iteration, and we increase the number of realizations by 15% in each following iteration. Within each iteration we employ the Metropolis algorithm to produce a random walk of samples, with the step size adjusted so that the acceptance ratio is 0.5. The simulation convergence requires up to 15 MMC iterations in the case that we study here.

Figure 3.18 shows the PDFs of the voltage for the marks and the spaces in the conventional and ODE-enhanced receivers. The voltage is normalised to the statistical average of signal voltages in each of the two receiver types. The BER estimated from the calculated PDFs is 4×10^{-4} for the conventional receiver and 10^{-5} for the ODE-enhanced receiver. This result demonstrates that significant improvement of the BER can be obtained in the modified receiver compared to the conventional scheme, thus validating the qualitative analysis of [80]. We stress the fact that BER improve-

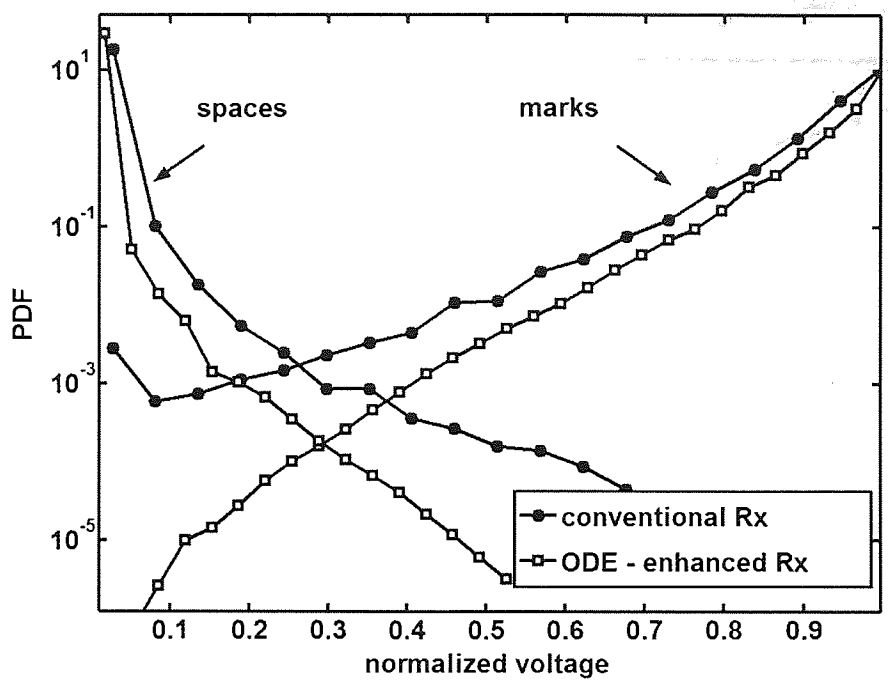

Figure 3.18: PDFs for the voltage of the marks and spaces in the conventional and ODE-enhanced receivers.

ment is achieved here by making decision in the optical domain, which is based effectively on using an additional information about the signals with respect to the conventional receiver. The tolerance of the ODE-enhanced receiver performance to the timing jitter of the input signal is shown in Figure 3.19, where the measured BER is plotted versus the input timing jitter standard deviation. We also calculate the BER as a function of the decision threshold. The results are shown in Figure 3.20 for the conventional and ODE-enhanced receivers. It is seen that the proposed receiver can operate at a lower BER than the conventional device for almost any decision level within the considered range, thus outperforming the conventional receiver. Next, we calculate the BER as a function of the decision threshold. The results are shown in Figure 3.21 for the conventional and ODE-enhanced receivers. The BER penalty is defined here as the ratio of the BER to its optimal value (the BER estimated at the optimal decision threshold). The decision level is normalised to the peak voltage of the signal in each receiver type. It is seen that, while the BER for the proposed receiver remains well below the optimal BER for the conventional receiver within the considered decision level range, the performance of the conventional re-

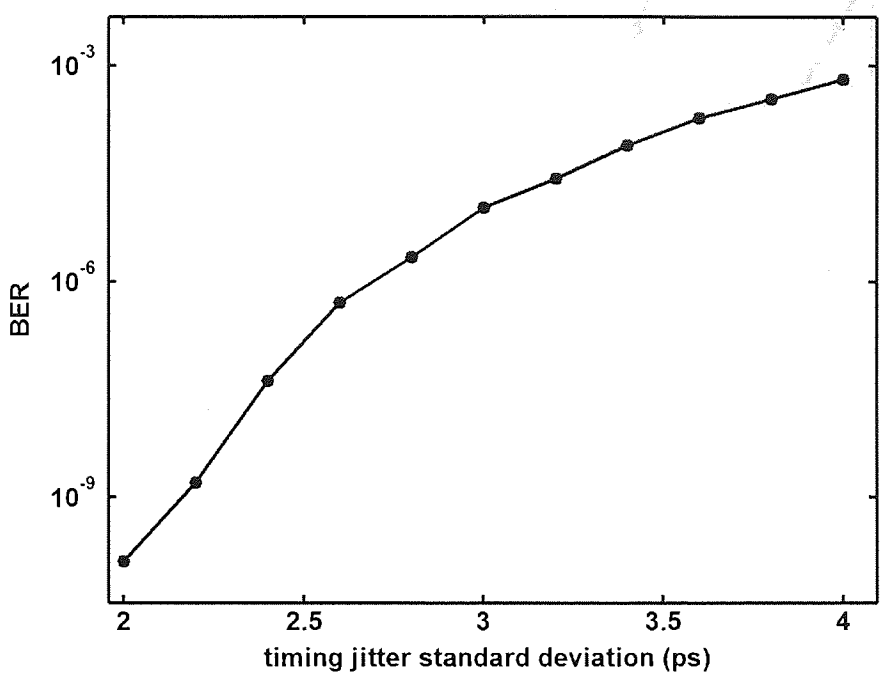

Figure 3.19: BER versus input timing jitter standard deviation for the ODE-enhanced receiver.

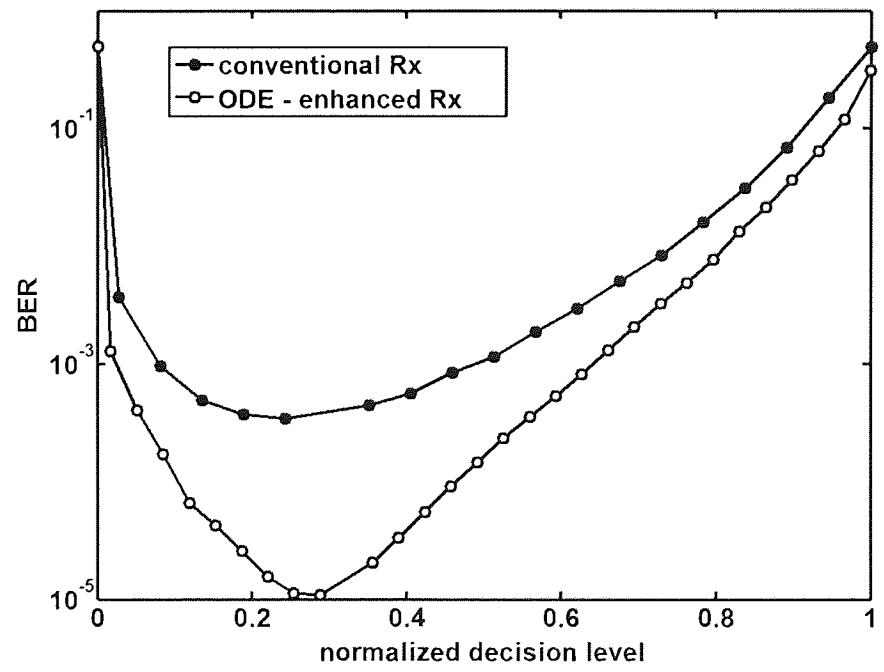

Figure 3.20: BER versus decision threshold for the conventional and ODE-enhanced receivers.

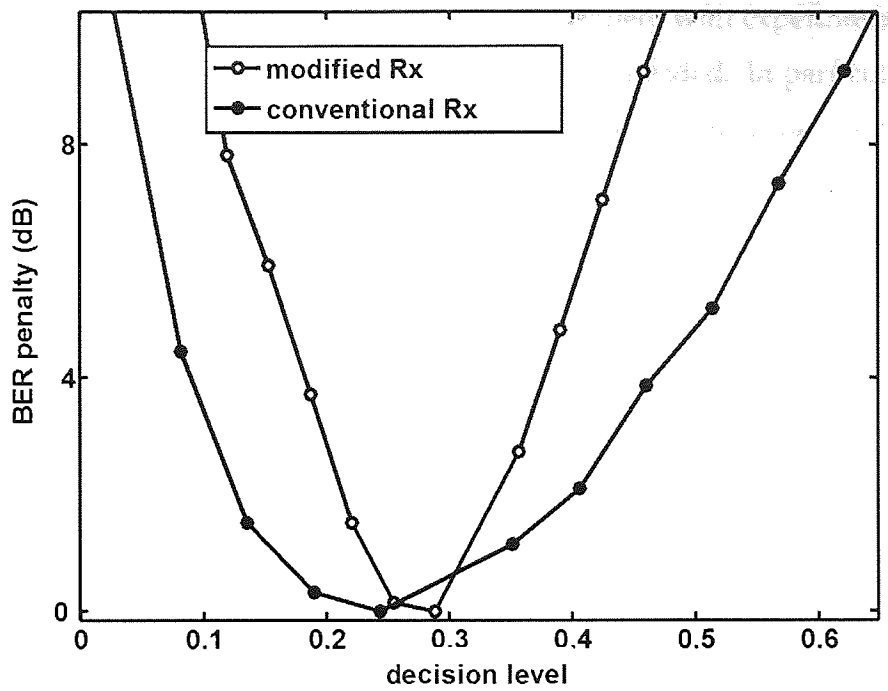

Figure 3.21: BER penalty versus decision threshold for the conventional and ODE-enhanced receivers.

ceiver is more tolerant to the decision threshold. However, we note that, because of the EDFA action, the signal voltage in the ODE-enhanced receiver is three orders larger than that in the conventional receiver and, therefore, the actual performance tolerance to the decision level is much larger for the ODE-enhanced receiver than for the conventional receiver. Of course, one may increase the signal voltage in the conventional receiver by use of a pre-amplifier.

In summary, in this section using the MMC method, we computed the performance of a RZ optical receiver with an additional nonlinear ODE. We exploited an ODE scheme based on an optical temporal gate enhanced by the effect of Kerr nonlinearity in a NDF. We demonstrated more than one order improvement in the BER compared to the conventional receiver, for operation at 40Gb/s data rate.

3.7 Conclusions

The accurate calculation of BER remains the most important and difficult theoretical problem in optical fibre communication. Though the results obtained under the

assumption of Gaussian statistics show a good agreement with experiments, from a theoretical point of view a more rigorous approach is needed. In particular, Gaussian statistics does not hold for large propagation distances, since the optical system under consideration is essentially nonlinear. At the same time, as the desired bit error rates are very low (of the order of 10^{-9} or less), the knowledge of the tails of the PDF is absolutely crucial for the effective estimate of the BER.

In this chapter we approach the statistical issues in optical communication with the aid of an advanced Monte Carlo technique. As such, we have implemented the MMC method, particularly acknowledged for its efficiency in calculating the distribution tails. This method increases the number of events in the tail region of PDF by introducing a sampling bias. The bias is determined iteratively and the algorithm automatically converges to the optimal bias. The general introduction and theoretical aspects to the MMC are, thus, presented in section 3.2.

In section 3.3 we apply the MMC method to evaluating the statistical properties of optical solitons. In particular, MMC suggests a possibility to investigate the PDFs of the phase and timing jitter, which in general can not be treated analytically whereas their effect prevails that one of other jitters. Our results for the amplitude distribution show a complete agreement with the analytical expression derived in [66]. Moreover, numerically estimated PDFs can subsequently be used for evaluating the BER in soliton-based optical transmission systems. The results of our modelling fully confirm previous analytical studies of soliton statistics.

In section 3.4 we examine the performance of optical transmission lines with in-line optical regenerators. A quantitative analysis of the BER penalty due to deviations from the optimal decision level in systems employing optical regeneration is presented. Using extensive MMC modelling we studied accumulation of BER with propagation and compared different linear approximations of the regenerator nonlinear transfer function.

In section 3.5 we investigate optical fibre links deploying RZ-DPSK modulation format. We perform a statistical analysis of RZ-DPSK signals simultaneously affected by timing and phase jitters. Moreover, in such systems we derive analytically a close-form expression for the BER in the limit of narrow pulses considering two

and four-pulse models. The derived analytical expression has a simple physical interpretation. This theoretical results are in excellent agreement with numerical simulations.

Finally, in section 3.6 we studied the performance of an ODE scheme based on an optical temporal gate enhanced by the effect of Kerr nonlinearity in a NDF. A significant improvement in the BER compared to the conventional receiver at the channel rate of 40 Gb/s is demonstrated.

Chapter 4

Conclusions

The major limitations to performance in state-of-art long-haul lightwave communication systems operating at, and in excess of, 40 Gb/s are imposed by the nonlinear impairments and the amplification noise. In this thesis, therefore, we focus on examining the possibilities of suppressing or minimising these negative effects.

In Chapter 2 we introduce a simple technique, designed to optimise the transmission performance in optical links with pure Raman and hybrid Raman-EDFA amplification. The optimal configurations were found from a balance condition between the effects of nonlinearity and ASE noise.

To facilitate the theoretical optimisation, i.e. using the method of Lagrange multipliers, we have proposed a general analytical model applicable to arbitrary DM transmission links with Raman amplification. However, the theoretical analysis did not account for small contributions of the pump depletion and DRS noise, so we have also carried out full numerical modelling which was based on power evolution equations.

With the aid of this optimisation method we have determined the optimal location of the dispersion compensating module within a three-step dispersion map with distributed backward amplification. For the particular SMF/DCF configuration considered with the transmission distance 1000 km of SMF, such an optimal split was found to be in the range of (10-25%SMF)+DCF+(90%-75%SMF).

Subsequently, we applied the proposed optimisation approach to design optimisation of an optical transmission line with bidirectional Raman amplification. More

specifically, we have examined a transmission link with a three-step dispersion map, composed by two sections of transport fibre SLA and one (intermediate) section of dispersion compensating IDF. We have shown that in the case that we consider, the numerical and analytical approaches lead to the same final solution. The optimal gain split between the forward and backward propagating pump powers was found to be 50%, and 70%SMF+DCF+30%SMF dispersion map present the optimum performance.

Similar optimisation analysis have also been conducted for transmission links with hybrid Raman/EDFA amplification scheme. As such, we examined cascaded spans, with each span composed by a section of SMF, followed by a section of DCF. The backward Raman pump source was inserted in the line at the end of the SMF section. The EDFA was set following the DCF. We determined the optimal dependence between the gain split and the launch signal power. Subsequently, we considered a configuration where the Raman pump source was allocated immediately prior to EDFA. In such a configuration we found the optimal share between the Raman and EDFA gains and the optimal location of the dispersion compensating fibre within the amplification period.

Moreover, we applied the suggested optimisation technique to calculate the optimal span length in systems with Raman amplification. We have demonstrated the existence of a non-trivial optimal amplifier spacing, matching modern requirements of cost efficient system design, for 40 Gb/s WDM dispersion-managed transmission systems with hybrid Raman/EDFA amplification scheme.

In Chapter 3 we address the statistical properties of optical signals. By taking an advantage of the Multicanonical Monte Carlo (MMC) simulation technique. In order to increase the number of events from the tail of the PDF being computed, the MMC technique samples noise from a biased PDF and updates the bias automatically by using an iterative procedure. The method was comprehensively implemented in C++.

We estimated the statistics of optical soliton parameters in the presence of ASE noise. By solving numerically the Langevin equation system, derived from the Fokker-Planck equation for the joint probability function of soliton parameters, we

estimated the distributions of soliton amplitude, phase, frequency and timing jitter. The results demonstrated complete agreement with the pre-existing analytical studies.

We accomplished the numerical study of statistical properties and the BER in transmission lines with 2R optical regenerators. We presented a quantitative analysis of the BER penalty due to deviations from the optimal decision level in systems employing optical regeneration. We studied accumulation of BER with propagation and compared different linear approximations of the regenerator nonlinear transfer function.

We model the return to zero differential phase shift keying optical signal statistics at a direct detection receiver with Mach-Zehnder interferometer demodulation. We applied numerical and theoretical analysis to the investigation of the statistical properties and the BER of RZ-DPSK signals, deteriorated by phase and timing jitters. By means of two- and four-pulse analysis, we found an analytical expression that can be used to evaluate the BER in such systems. A high accuracy of this estimate was demonstrated by comparison with the result of direct numerical simulations.

We numerically studied the performance of an ODE scheme based on an optical temporal gate enhanced by the effect of Kerr nonlinearity in a normal dispersion fibre. We have shown a significant improvement in the BER compared to the conventional receiver at the channel bit rate of $40\,\mathrm{Gb/s}$.

Appendix A

Parameters of optical fibres

fibre	dispersion $(ps/nm/km)$	α_s (dB/km)	α_p (dB/km)	A_{eff} (μm^2)	g_R/A_{eff} $(W^{-1}km^{-1})$	n_2 $(10^{-20}$ $m^2W^{-1})$	ε $(10^{-4}$ $km^{-1})$
SMF	17	0.2	0.257	80	0.39	2.7	0.641
DCF	100	0.65	1.2	19	1.75	2.7	6.06
SLA	20	0.188	0.234	106	0.29	2.35	0.4
IDF	-42.3	0.233	0.304	30	1.2	2.7	1.6

Table A.1: Specification of optical fibres used in simulations.

Appendix B

Computer implementation of the MMC algorithm

In the framework of the present research we developed a comprehensive Object-Oriented softwear for the advanced MMC simulation technique. With the aid of this code we investigated a range of statistical problems, with the examples shown in Chapter 3. This Appendix focuses on the issues of the conceptual modelling and the program design of implementing this advanced Monte Carlo method. The principle structure of the generated code is shown on a Unified Modelling Language (UML) 2 class diagram in Figure B.1. The schematic represents the classes, their interrelationships, and the operations and attributes of the classes. In the figure classes are depicted as boxes with three sections, the top one indicates the name of the class, the middle one lists the attributes of the class, and the third one lists the methods. The arrows linking the boxes, moreover, show the association links between classes. Please note that the diagram is shown for demonstration purpose and does not include all details.

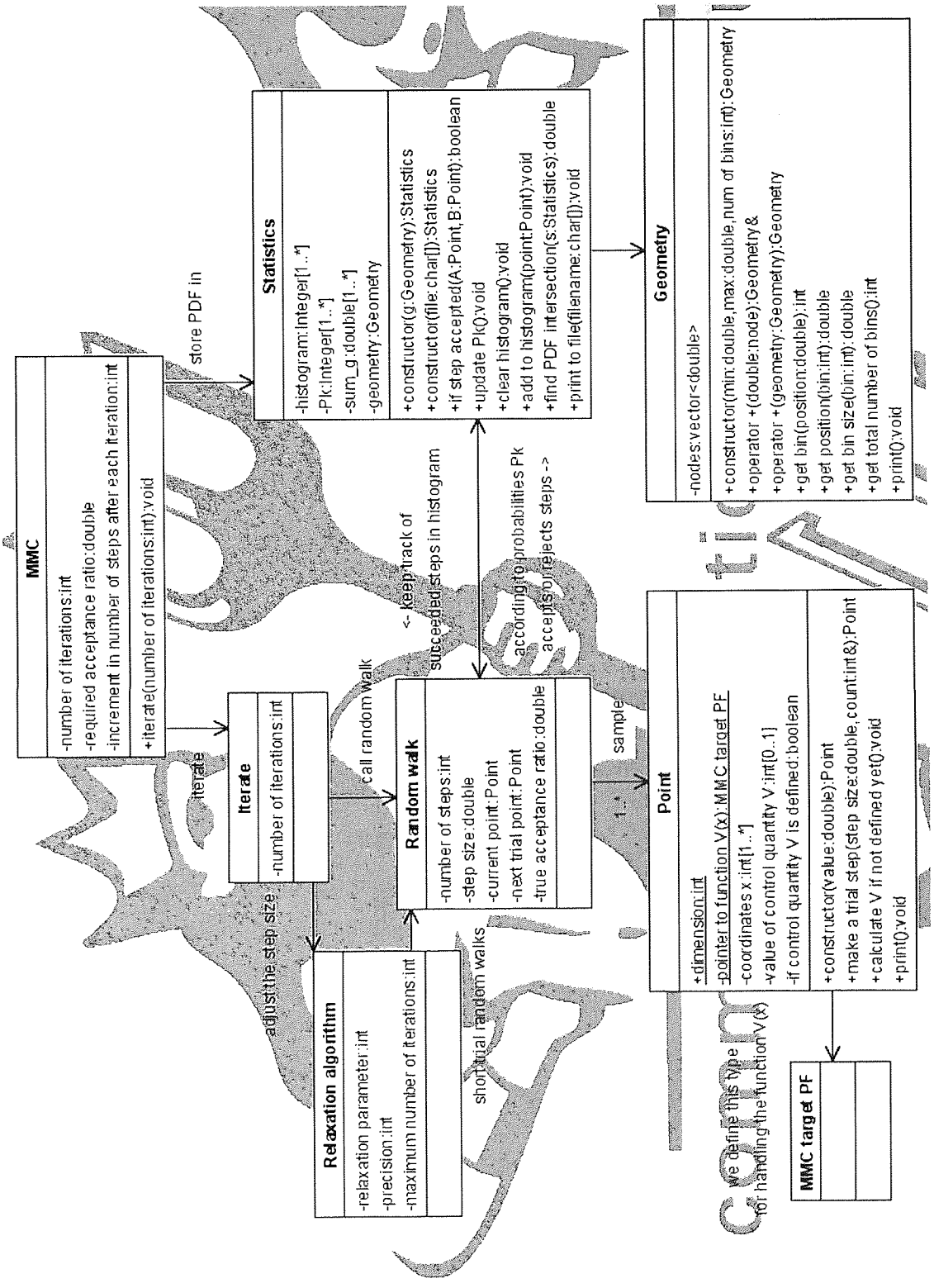

Figure B.1: UML 2 class diagram for our computer implementation of the MMC technique.

Appendix C

Acronyms

ASE	amplified spontaneous emission
AWGN	added white gaussian noise
BER	bit-error rate
BVP	boundary value problem
DC	dispersion compensation
DCF	dispersion-compensating fibre
DM	dispersion management
DPSK	differential phase shift keying
DRA	distributed Raman amplification
DRS	double Rayleigh scattering
EDFA	erbium-doped fibre amplifier
FEC	forward error correction
FWM	four-wave mixing
GVD	group velocity dispersion
IDF	inverse dispersion fibre
IFWM	intrachannel four-wave mixing
IXPM	intrachannel cross phase modulation
MMC	multicanonical Monte Carlo
MZI	Mach-Zehnder interferometer
NDF	normal dispersion fibre
NPS	nonlinear phase shift

ODE	optical decision element
OR	optical regenerator
OSNR	optical signal-to-noise ratio
PMD	polarisation mode dispersion
PDF	probability density function
RZ	return-to-zero
SLA	super-large effective area
SMF	standard monomode fibre
SNR	signal-to-noise ratio
SPM	self phase modulation
UML	Unified Modelling Language
WDM	wavelength-division multiplexing
XPM	cross phase modulation

Appendix D

Publications

1. I. Nasieva, A. Kaliazin and S. K. Turitsyn, "Multicanonical Monte Carlo modelling of BER penalty in transmission systems with optical regeneration", *Optics Communications*, vol. 262, no. 2, page 246, 2006

2. I. Nasieva, S. Boscolo and S. K. Turitsyn, "Bit error rate improvement by nonlinear optical decision element", *Optics Letters*, vol. 31, no. 9, page 1205, 2006

3. J. D. Ania-Castanon, I. Nasieva, S. K. Turitsyn, N. Brochier and E. Pincemin, "Optimal span length in high-speed transmission systems with hybrid Raman-erbium-doped fiber amplification", *Optics letters*, vol. 30, no. 1, page 23, 2005

4. I. Nasieva, J. D. Ania-Castanon, S. K. Turitsyn, N. Brochier, E. Pincemin and M. P. Fedoruk , "Span design for reduced noise and nonlinear impairments in a dispersion-managed Raman amplified system", *Optical and quantum electronics*, vol. 36, no. 8, page 725, 2004

5. J. D. Ania-Castanon, I. Nasieva, N. Kurukitkoson, S. K. Turitsyn, N. Brochier and E. Pincemin, " Nonlinearity management in fiber transmission systems with hybrid amplification", *Optics Communications*, vol. 233, no. 4-6, page 353, 2004

6. I. Nasieva, S. A. Derevyanko and S. K. Turitsyn, "Statistics of RZ-DPSK optical signal at direct detection receiver with Mach-Zehnder interferometer demod-

ulation", Abstract in the half day meeting organised by the ITEC group of the IOP, London, 30-th of June, 2004

7. I. Nasieva, S. A. Derevyanko and S. K. Turitsyn, "Non-Gaussian statistics of optical solitons", Abstract in the summer School "New concepts in photonics and optical communications", Dijon, France, June 21-25, 2004

8. J. D. Ania-Castanon, I. Nasieva, S. K. Turitsyn, N. Brochier and E. Pincemin, "Span length optimization in a hybrid amplification system", In the conference Nonlinear Guided Waves and Their Applications 2004, paper MC4, 2004

9. J. D. Ania-Castanon, I. Nasieva, N. Kurukitkoson, S. K. Turitsyn, N. Brochier and E. Pincemin, "Nonlinearity management in hybrid transmission systems", In the conference Nonlinear Guided Waves and Their Applications 2004, paper MC21, 2004

10. J. D. Ania-Castanon, I. Nasieva, S. K. Turitsyn, N. Brochier and E. Pincemin, "Optimal span length in high-speed transmission systems with hybrid Raman/EDFA amplification", Optical Networks and Technologies, International Federation for Information Processing — Springer, 164, Pisa, page 307, 2004

11. I. Nasieva, J. D. Ania-Castanon and S. K. Turitsyn, "Nonlinearity management in fibre links with distributed amplification", *Electronics Letters*, vol. 39, no. 11, page 856, 2003

12. I. Nasieva and M. P. Fedoruk, "Fibreoptic communication lines with distributed Raman amplification: Numerical simulation", *Quantum Electronics*, vol. 33, no. 10, page 908, 2003

Bibliography

[1] G. P. Agrawal. *Fiber-optic Communication Systems*. Wiley-Interscience, 2002.

[2] T. H. Maiman. Stimulated optical radiation in ruby. *Nature*, 187:493, 1960.

[3] K. C. Kao and G. A. Hockham. Dielectric-fibre surface waveguides for optical frequencies. *IEE Proceedings J (Optoelectronics)*, 133(3):191, 1986.

[4] A. Werts. Propagation de la lumiére cohérente dans les fibres optiques. *L'Onde Electrique*, 46:967, 1966.

[5] F. P. Kapron, D. B. Keck, and R. D. Mourer. Radiation losses in glass optical waveguides. *Applied Physics Letters*, 17(10):423, 1970.

[6] R. J. Sanferrare. Terrestrial Lightwave Systems. *AT & T Technical Journal*, 66(1):95.

[7] J. I. Yamada, S. Machida, and T. Kimura. 2 Gbit/s optical transmission experiments at 1.3 μm with 44 km single mode fibre. *Electronics Letters*, 17(13):479, 1981.

[8] A. H. Gnauck, B. L. Kasper, R. A. Linke, R. W. Dawson, T. L. Koch, T. J. Bridges, E. G. Burkhardt, , R. T. Yen, D. P. Wilt, J. C. Campbell, K. C. Nelson, and L. G. Cohen. 4-Gbit/s transmission over 103 km of optical fibre using novel electronic miltiplexer/demultiplexer. *Journal of Lightwave Technologies*, 3:1032.

[9] N. S. Bergano and H. Kidorf. Global undersea cable networks. *Optics & Photonics News*, 12(3):32.

[10] G. A. Thomas, B. I. Shralman, P. F. Glodis, and M. J. Stephan. Towards the clarity limit in optical fibre. *Nature*, 404:262.

[11] J. P. Gordon and H. A. Haus. Random walk of coherently amplified solitons in optical fiber transmission. *Optics Letters*, 11(10):665, 1986.

[12] F. Forghieri, P. R. Prucnal, R. W. Tkach, and A. R. Chraplyvy. RZ versus NRZ in nonlinear WDM systems. *IEEE Photonics Technology Letters*, 9(7):1035.

[13] C. Lin, H. Kogelnik, and L. G. Kohen. Optical pulse equalization and low dispersion transmission in single-mode fibers in the 1.3-1.7 μm spectral region. *Optics Letters*, 5(11):476, 1980.

[14] A. H. Gnauck, C. R. Giles, L. J. Jr. Cimini, J. Stone, L. W. Stulz, S. K. Korotky, and J. J. Veselka. 8-gb/s-130 km transmission experiment using er-doped fiber preamplifier and optical dispersion equalization. *IEEE Photonics Technology Letters*, 3(12):1147, 1991.

[15] K. Takiguchi, K. Okamoto, and K. Moriwaki. Dispersion compensation using a planar lightwave circuit optical equalizer. *IEEE Photonics Technology Letters*, 6(4):561, 1994.

[16] D. K. W. Lam, B. K. Garside, and K. O. Hill. Dispersion cancellation using optical-fiber filters. *Optics Letters*, 7(6):291, 1982.

[17] F. Ouellette. All-fiber filter for efficient dispersion compensation. *Optics Letters*, 16(5):303, 1991.

[18] B. Bakhshi, M. F. Arend, M. Vaa, E. A. Golovchenko, D. Duff, H. Li, S. Jiang, W. W. Patterson, R. L. Maybach, and D. Kovsh. 1 Tbit/s (101$\times$10 Gbit/s) transmission over transpacific distance using 28 nm C-band EDFAs. *Conference on Optical Fiber Communication. Technical Digest Postconference Edition. Postdeadline Papers*, 4:21, 2001.

[19] A. Hasegawa and F. Tappert. Transmission of stationary nonlinear optical pulses in dispersive dielectric fibers. i. anomalous dispersion. *Applied Physics Letters*, 23(3):142.

[20] L. F. Mollenauer, R. H. Stolen, and J. P. Gordon. Experimental observation of picosecond pulse narrowing and solitons in optical fibers. *Physical Review Letters*, 45(13):1095.

[21] L. F. Mollenauer, P. V. Mamyshev, and M. J. Neubelt. Demonstration of soliton WDM transmission at up to 8×10 Gbit/s, error-free over transoceanic distances. *Conference on Optical Fiber Communication. Technical Digest Series. Post-conference Edition*, 2:415, 1996.

[22] N. J. Smith, N. J. Doran, W. Forysiak, and F. M. Knox. Soliton transmission using periodic dispersion compensation. *Journal of Lightwave Technology*, 15(10):1808, 1997.

[23] W. Forysiak, K. J. Blow, and N. J. Doran. Reduction of Gordon-Haus jitter by post-transmission dispersion compensation. *Electronics Letters*, 29(13):1225, 1993.

[24] M. Nakazawa, K. Suzuki, H. Kubota, and E. Yamada. 60 Gbit/s WDM (20 Gbit/s×3 unequally spaced channels) soliton transmission over 10000 km using in-line synchronous modulation and optical filtering. *Electronics Letters*, 32(18):1686, 1996.

[25] A. Sahara, T. Inui, T. Komukai, H. Kubota, and M. Nakazawa. 40-Gb/s RZ transmission over transoceanic distance in a dispersion managed standard fiber using a new inline synchronous modulation method. *IEEE Photonics Technology Letters*, 12(6):720, 2000.

[26] L. F. Mollenauer, J. P. Gordon, and S. G. Evangelides. The sliding-frequency guiding filter: an improved form of soliton jitter control. *Optics Letters*, 17(22):1575, 1992.

[27] D. Wolfson, P. B. Hansen, A. Kioch, and K. E. Stubkjaer. All-optical 2R regeneration based on interferometric structure incorporating semiconductor optical amplifiers. *Electronics Letters*, 35(1):59, 1999.

[28] S. Boscolo, S. K. Turitsyn, and K. J. Blow. Study of the operating regime for all-optical passive 2R regeneration of dispersion-managed RZ data at 40 Gb/s using in-line NOLMs. *IEEE Photonics Technology Letters*, 14(1):30, 2002.

[29] A. Hirano, H. Tsuda, H. Kobayashi, R. Takahashi, M. Asobe, K. Sato, and K. Hagimoto. All-optical discrimination based on nonlinear transmittance of MQW semiconductor optical gates. *Journal of Lightwave Technology*, 17(5):873, 1999.

[30] P. S. Cho, P. Sinha, D. Mahgerefteh, and G. M. Carter. All-optical 2R-regeneration of 10 Gbit/s RZ data transmitted over 30,000 km in a dispersion-managed system using an electroabsorption modulator. *Conference on Optical Fiber Communication. Technical Digest Series*, 2:275, 2000.

[31] G. Raybon, Yikai Su, B. Mikkelsen, and R.-J. Essiambre. Ultra-high speed optical signal transmission: single channel 40 Gbit/s, 80 Gbit/s and 160 Gbit/s. *Proceeding of the International Conference on Telecommunications*, 1:1390, 2002.

[32] A. H. Gnauck and P. J. Winzer. Optical phase-shift-keyed transmission. *Journal of Lightwave Technology*, 23(1):115, 2005.

[33] R.-J. Essiambre, B. Mikkelsen, and G. Raybon. Intra-channel cross-phase modulation and four-wave mixing in high-speed TDM systems. *Electronics Letters*, 35(18):1576, 1999.

[34] P. V. Mamyshev and N. A. Mamysheva. Pulse-overlapped dispersion-managed data transmission and intrachannel four-wave mixing. *Optics Letters*, 24(21):1454, 1999.

[35] M. J. Ablowitz and T. Hirooka. Resonant intrachannel pulse interactions in dispersion-managed transmission systems. *IEEE Journal on Selected Topics in Quantum Electronics*, 8(3):603, 2002.

[36] A. V. Kanaev, G. G. Luther, V. Kovanis, S. R. Bickham, and J. Conradi. Ghost-pulse generation suppression in phase-modulated 40-Gb/s RZ transmission. *Journal of Lightwave Technology*, 21(6):1486, 2003.

[37] P. Johannisson, D. Anderson, M. Marklund, A. Berntson, M. Forzati, and J. Martensson. Suppression of nonlinear effects by phase alternation in strongly dispersion-managed optical transmission. *Optics Letters*, 27(12):1073, 2002.

[38] L. Xiang, C. Xu, and W. Xing. Nonlinear phase noise in pulse-overlapped transmission based on return-to-zero differential-phase-shift-keying. *28th European Conference on Optical Communication*, 4:2, 2002.

[39] X. Wei and X. Liu. Analysis of intrachannel four-wave mixing in differential phase-shift keying transmission with large dispersion. *Optics Letters*, 28(23):2300, 2003.

[40] G. Charlet, E. Corbel, J. Lazaro, A. Klekamp, R. Dischler, P. Tran, W. Idler, H. Mardoyan, A. Konczykowska, F. Jorge, and S. Bigo. WDM transmission at 6-Tbits/s capacity over transatlantic distance, using 42.7-Gb/s differential phase-shift keying without pulse carver. *Journal of Lightwave Technology*, 23(1):104, 2005.

[41] B. Zhu, L. E. Nelson, S. Stulz, A. H. Gnauck, C. Doerr, J. Leuthold, L. Gruner-Nielsen, M. O. Pedersen, J. Kim, R. Jr. Lingle, Y. Emori, Y. Ohki, N. Tsukiji, A. Oguri, and S. Namiki. 6.4-Tb/s (160×42.7 Gb/s) transmission with 0.8 bit/s/Hz spectral efficiency over 32×100 km of fiber using CSRZ-DPSK format. *Conference on Optical Fiber Communication. Trends in Optics and Photonics Series. Postdeadline Papers*, 3:19, 2003.

[42] A. H. Gnauck, G. Raybon, S. Chandrasekhar, J. Leuthold, C. Doerr, L. Stulz, A. Agarwal, S. Banerjee, D. Grosz, S. Hunsche, A. Kung, A. Marhelyuk, D. Maywar, M. Movassaghi, X. Liu, C. Xu, X. Wei, and D. M. Gill. 2.5 Tb/s (64×42.7 Gb/s) transmission over 40×100 km NZDSF using RZ-DPSK format and all-Raman-amplified spans. *Conference on Optical Fiber Communication. Postconference Technical Digest. Postdeadline Papers*, 2:2, 2002.

[43] M. Daikoku, T. Miyazaki, I. Morita, H. Tanaka, F. Kubota, and M. Suzuki. 8×160-Gb/s WDM field transmission experiment with single-polarization

RZ-DPSK signals and PMD compensator. *IEEE Photonics Technology Letters*, 18(2):391, 2006.

[44] A. Agata, K. Tanaka, and N. Edagawa. Study on the optimum reed-solomon-based FEC codes for 40-Gb/s-based ultralong-distance WDM transmission. *Journal of Lightwave Technology*, 20(12):2189, 2002.

[45] R. H. Morelos-Zaragoza. *The art of error correcting coding*. John Wiley & Sons Ltd, 2002.

[46] C. Berrou and A. Glavieux. Near optimum error correcting coding and decoding: turbo-codes. *IEEE Transactions on Communications*, 44(10):1261, 1996.

[47] C. Berrou, A. Glavieux, and P. Thitimajshima. Near Shannon limit error-correcting coding and decoding: Turbo-codes (1). *IEEE International Conference on Communications, 93*, page 1064, 1993.

[48] J.-C. Antona, S. Bigo, and J.-P. Faure. Nonlinear cumulated phase as a criterion to assess performance of terrestrial wdm systems. *Conference on Optical Fiber Communication. Postconference Technical Digest*, 1:365, 2002.

[49] V. E. Perlin and H. G. Winful. On trade-off between noise and nonlinearity in wdm systems with distributed raman amplification. *Conference on Optical Fiber Communication. Technical Digest Series*, 70:178, 2002.

[50] S. K. Turitsyn, M. P. Fedoruk, V. K. Mezentsev, and E. G. Turitsyna. Theory of optimal power budget in quasi-linear dispersion-managed fibre links. *Electronics Letters*, 39(1):29, 2003.

[51] H. Kidorf, K. Rottwitt, M. Nissov, M. Ma, and E. Rabarijaona. Pump interactions in a 100-nm bandwidth Raman amplifier. *IEEE Photonics Technology Letters*, 11(5):530, 1999.

[52] U. Ascher, J. Christiansen, and R. D. Russell. COLSYS – a collocation code for boundary-value problems. *Codes for Boundary-Value Problems in Ordinary Differential Equations*, page 164, 1979.

[53] U. Ascher, J. Christiansen, and R. D. Russell. A collocation solver for mixed order systems of boundary value problems. *Mathematics of Computation*, 33(146):659, 1979.

[54] W. H. Press, B. P. Flannery, S. A. Teukolsky, and W. T. Vetterling. *Numerical Recipes in C*. Cambridge University Press, 1988.

[55] M. N. Islam. Raman amplifiers for telecommunications. *IEEE Journal of Selected Topics in Quantum Electronics*, 8(3):548, 2002.

[56] S. Namiki and Y. Emori. Ultrabroad-band Raman amplifiers pumped and gain-equalized by wavelength-division-multiplexed high-power laser diodes. *IEEE Journal of Selected Topics in Quantum Electronics*, 7(1):3, 2001.

[57] G. P. Agrawal. *Applications of Nonlinear Fiber Optics*. Academic Press, 2001.

[58] A. Yariv. Signal-to-noise considerations in fiber links with periodic or distributed optical amplification. *Optics Letters*, 15(19):1064, 1990.

[59] E. Desurvire and O. Leclerc. Fundamental bit-error-rate limits of in-line optical regeneration by synchronous intensity modulation: an analytical Gaussian-statistics model. *Optical Fiber Technology: Materials, Devices and Systems*, 6(3):230, 2000.

[60] F. Ohman, S. Bischoff, B. Tromborg, and J. Mork. Noise and regeneration in semiconductor waveguides with saturable gain and absorption. *IEEE Journal of Quantum Electronics*, 40(3):245, 2004.

[61] B. A. Berg. Algorithmic aspects of multicanonical simulations. *Nuclear Physics B, Proceedings Supplements*, 63:982, 1998.

[62] R. Holzlohner, C. B. Menyuk, W. L. Kath, and V. S. Grigoryan. Use of multicanonical monte carlo simulations to obtain accurate bit error rates in optical communications systems. *Optics Letters*, 28(20):1894, 2003.

[63] D. Yevick. Multicanonical Monte-Carlo simulations applied to PMD. *2003 Digest of LEOS Summer Topical Meeting*, page 2, 2003.

[64] N. Metropolis and S. Ulam. The monte carlo method. *Journal of the American Statistical Association*, 44, 1949.

[65] G. E. Falkovich, M. G. Stepanov, and S. K. Turitsyn. Statistics of interacting optical solitons. *Physical Review E. Statistical Physics, Plasmas, Fluids, and Related Interdisciplinary Topics*, 64(6 II):067602 – 1, 2001.

[66] S. A. Derevyanko, S. K. Turitsyn, and D. A. Yakushev. Non-Gaussian statistics of an optical soliton in the presence of amplified spontaneous emission. *Optics Letters*, 28(21):2097, 2003.

[67] E. Iannone, F. Materra, A. Mecozzi, and M. Settembre. *Nonlinear Optical Communication Networks*. John Wiley & Sons, 1998.

[68] H. Risken. *The Fokker-Planck equation*. Springer, 1996.

[69] G. Falkovich, I. Kolokolov, V. Lebedev, V. Mezentsev, and S. Turitsyn. Non-gaussian error probability in optical soliton transmission. *Physica D: Nonlinear Phenomena*, 195(1-2):1, 2004.

[70] K.-P. Ho. Phase statistics of the soliton. *Journal of the Optical Society of America B (Optical Physics)*, 21(2):266, 2004.

[71] O. Leclerc, B. Lavigne, E. Balmefrezol, P. Brindel, L. Pierre, D. Rouvillain, and F. Seguineau. Optical Regeneration at 40 Gb/s and beyond. *Journal of Lightwave Technology*, 21(11):2779, 2003.

[72] M. Hanna, H. Porte, J.-P. Goedgebuer, and W. T. Rhodes. Performance assessment of DPSK soliton transmission system. *Electronics Letters*, 37(10):644, 2001.

[73] D. Marcuse. Derivation of analytical expressions for the bit-error probability in lightwave systems with optical amplifiers. *Journal of Lightwave Technology*, 8(12):1816, 1990.

[74] K.-P. Ho. Performance degradation of phase-modulated systems due to nonlinear phase noise. *IEEE Photonics Technology Letters*, 15(9):1213, 2003.

[75] X. Zhang, G. Zhang, C. Xie, and L. Wang. Noise statistics in optically preamplified differential phase-shift keying receivers with Mach-Zehnder interferometer demodulation. *Optics Letters*, 29(4):337, 2004.

[76] R. Lopez-Valcarce and S. Dasgupta. Second-order statistical properties of nonlinearly distorted phase-shift keyed (PSK) signals. *IEEE Communications Letters*, 7(7):323, 2003.

[77] S. Primak, V. Kontorovich, and V. Lyandres. *Stohastic methods and their applications to communications*. John Wiley & Sons, Ltd, 2004.

[78] M. Suzuki, H. Toda, A. H. Liang, and A. Hasegawa. Improvement of amplitude and phase margins in an RZ optical receiver using Kerr nonlinearity in normal dispersion fiber. *IEEE Photonics Technology Letters*, 13(11):1248, 2001.

[79] P. Ghelfi, M. Scaffardi, M. Secondini, F. Fresi, M. F. Matchouani, A. Bogoni, and L. Poti. Additional all-optical decision element improving the performance of band-limited receivers in RZ systems. *31st European Conference on Optical Communication*, 3:323, 2005.

[80] S. Boscolo, S. K. Turitsyn, and K. J. Blow. Time domain all-optical signal processing at a RZ optical receiver. *Optics Express*, 13(16):6217, 2005.

[81] M. Rochette, J. N. Kutz, J. L. Blows, D. Moss, J. T. Mok, and B. J. Eggleton. Bit-error-ratio improvement with 2R optical regenerators. *IEEE Photonics Technology Letters*, 17(4):908, 2005.

[82] H. Nakatsuka, D. Grischkowsky, and A. C. Balant. III.Nonliner picosecond-pulse propagation through optical fibres with positive group velocity dispersion. *NATO ASI Series, Series B: Physics*, 132:101, 1985.